



**Moderate Resolution Imaging  
Spectroradiometer (MODIS)  
Land Surface Temperature and Emissivity  
Product (MxD21) Algorithm Theoretical  
Basis Document  
Collection 6.1**

*Glynn Hulley, Nabin Malakar, Robert Freepartner*

*Jet Propulsion Laboratory, California Institute of Technology*

**National Aeronautics and  
Space Administration**

**Jet Propulsion Laboratory  
California Institute of Technology  
Pasadena, California**

**December 2016**

---

This research was carried out at the Jet Propulsion Laboratory, California Institute of Technology, under a contract with the National Aeronautics and Space Administration.

Reference herein to any specific commercial product, process, or service by trade name, trademark, manufacturer, or otherwise, does not constitute or imply its endorsement by the United States Government or the Jet Propulsion Laboratory, California Institute of Technology.

© 2016. California Institute of Technology. Government sponsorship acknowledged.

## Change History Log

Revision	Effective Date	Prepared by	Description of Changes
1.1	08/17/2012	Glynn Hulley	Version 1.0 draft by Glynn Hulley
1.2	11/02/12	Glynn Hulley	Section 10: Validation, updated by Glynn Hulley
1.3	11/19/2012	Peter Basch	Edited by Peter Basch, Technical Editor/Writer, Jet Propulsion Laboratory
2.0	03/27/2014	Glynn Hulley	Updated Table 2 to correct an error in the calculation of sky irradiance coefficients. Updated Table 3 and 4 WVS and bmp coefficients which are now valid for view angles up to 65 degrees and for a more diverse set of global atmospheric conditions.
2.2	2/10/15, 4/4/15	Nabin Malakar, Glynn Hulley, Tanvir Islam	Updated the WVS coefficients section to include view angle, PWV, and emissivity dependence. Included info on ASTER GED v3. Radiation-based validation results are updated. Updated the section on the RTTOV. Updated the R-based validation section.
2.3	01/09/2017	Glynn Hulley	Various typos and captions fixed. Updates to validation section.
2.4	05/08/2017	Glynn Hulley	Included NCEP GFS section and discussion and results of near-real time processing.
2.5	03/08/2021	Glynn Hulley	Updated information on how to calculate band model parameters in section 6.1.3
2.6	04/21/2022	Glynn Hulley	Updated broken links

## **Contacts**

Glynn C. Hulley

MS 183-501

Jet Propulsion Laboratory

4800 Oak Grove Dr.

Pasadena, CA 91109

Email: [glynn.hulley@jpl.nasa.gov](mailto:glynn.hulley@jpl.nasa.gov)

Office: (818) 354-2979

## Contents

<b>Contacts .....</b>	<b>2</b>
<b>1 Introduction.....</b>	<b>8</b>
<b>2 MODIS Background.....</b>	<b>10</b>
2.1 Calibration.....	10
2.2 Instrument Characteristics .....	11
2.3 LST&E Standard Products.....	11
<b>3 Earth Science Relevance.....</b>	<b>14</b>
3.1 Use of LST&E in Climate/Ecosystem Models .....	14
3.2 Use of LST&E in Cryospheric Research .....	15
3.3 Use of LST&E in Atmospheric Retrieval Schemes.....	16
<b>4 Thermal Infrared Radiative Transfer .....</b>	<b>17</b>
4.1 Thermal Infrared Radiance .....	17
4.2 Emissivity .....	21
<b>5 Atmospheric Correction.....</b>	<b>21</b>
5.1 Radiative Transfer Model .....	22
5.2 Atmospheric Profiles .....	24
5.2.1 MERRA-2 .....	24
5.2.2 NCEP Global Forecast System (GFS).....	26
5.2.3 Accuracy Assessment: NCEP versus MERRA2 .....	26
5.2.4 Transfer Sensitivity Analysis .....	27
<b>6 Water Vapor Scaling (WVS) Method .....</b>	<b>29</b>
6.1 Scaling Atmospheric Parameters .....	31
6.1.1 Transmittance and Path Radiance .....	31
6.1.2 Downward Sky Irradiance.....	31
6.1.3 Band model parameters .....	32
6.2 EMC/WVD Coefficients Calculation .....	35
6.2.1 Simulations.....	37
6.2.2 ASTER Global Emissivity Dataset (GED) v3 .....	38
<b>7 Temperature and Emissivity Separation Approaches.....</b>	<b>40</b>
7.1 Deterministic Approaches.....	41
7.1.1 SW Algorithms.....	41
7.1.2 Single-Band Inversion.....	42
7.1.3 Non-deterministic Approaches.....	43
7.2 TES Algorithm.....	45
7.2.1 TES Data Inputs .....	46
7.2.2 TES Limitations .....	46
7.2.3 TES Processing Flow .....	48
7.2.4 NEM Module.....	51
7.2.5 Subtracting Downwelling Sky Irradiance .....	51
7.2.6 Refinement of <i>emax</i> .....	52
7.2.7 Ratio Module.....	53

7.2.8	MMD Module.....	53
7.2.9	MMD vs. <i>emin</i> Regression.....	56
7.2.10	Atmospheric Effects.....	58
<b>8</b>	<b>Advantages of TES over SW approaches .....</b>	<b>59</b>
8.1	Land Cover Misclassification .....	60
8.2	Emissivity Error within Cover Type.....	61
8.3	Soil Moisture Effects .....	62
<b>9</b>	<b>Quality Assessment and Diagnostics .....</b>	<b>64</b>
<b>10</b>	<b>Uncertainty Analysis.....</b>	<b>65</b>
10.1	The Temperature and Emissivity Uncertainty Simulator .....	65
10.2	Atmospheric Profiles .....	66
10.3	Radiative Transfer Model .....	66
10.4	Surface End-Member Selection .....	66
10.5	Radiative Transfer Simulations.....	67
10.6	Error Propagation.....	69
10.7	Parameterization of Uncertainties.....	71
<b>11</b>	<b>Validation.....</b>	<b>75</b>
11.1	Water Sites.....	76
11.2	Pseudo-invariant Sand Dune Sites .....	78
11.2.1	Emissivity Validation .....	79
11.2.2	LST Validation .....	82
11.3	Vegetated Sites.....	87
11.4	Validation Summary .....	88
<b>12</b>	<b>References.....</b>	<b>92</b>

## Figures

- Figure 1. Simulated atmospheric transmittance for a US Standard Atmosphere (red) and tropical atmosphere (blue) in the 3–12  $\mu\text{m}$  region. Also shown is the solar irradiance contribution  $\text{W}/\text{m}^2/\mu\text{m}^2$ . 18
- Figure 2. Radiance simulations of the surface-emitted radiance, surface-emitted and reflected radiance, and at-sensor radiance using the MODTRAN 5.2 radiative transfer code, US Standard Atmosphere, quartz emissivity spectrum, surface temperature = 300 K, and viewing angle set to nadir. Vertical bars show placements of the MODIS TIR bands 29 (8.55  $\mu\text{m}$ ), 31 (11  $\mu\text{m}$ ), and 32 (12  $\mu\text{m}$ ). 19
- Figure 3. MODIS spectral response functions for bands 29 (red), 31 (green), and 32 (blue) plotted with a typical transmittance curve for a mid-latitude summer atmosphere. 20
- Figure 4. MODIS MOD07 total column water vapor (left) and WVS factor,  $\gamma$ , (right) computed using Equation (5 and 6) for a MODIS scene cutout on 29 August 2004. 31
- Figure 5. Comparisons between the atmospheric transmittance (top), path radiance ( $\text{W}/\text{m}^2/\mu\text{m}^{-1}$ ) (middle), and computed surface radiance ( $\text{W}/\text{m}^2/\mu\text{m}^{-1}$ ) (bottom), before and after applying the WVS scaling factor  $\gamma$  to a MODIS scene cutout shown in Figure 5. Results are shown for MODIS band 29 (8.55  $\mu\text{m}$ ). 34
- Figure 6. The total precipitable water versus skin temperature in the SeeBor profile used in the simulation for generating view angle and day–night-dependent coefficients. 36
- Figure 7. Global SeeBor radiosonde database showing the distribution of day (red stars) and night (open blue circles) profiles used in the generation of the WVS coefficients. 36
- Figure 8. The RMSE between calculated and modeled surface brightness temperature for MODIS Aqua band 29 are plotted for corresponding view angles considered in the simulation using global radiosonde profile data as discussed in the text. The RMSE is less than 1 K for view angles less than 60°. 38
- Figure 9. Spectrally adjusted ASTER GED emissivity for MODIS band 29 (see text for details). The ASTER GED emissivity (100 m) has been geolocated onto the MODIS swath (1-km) and has been adjusted for vegetation phenology using the MODIS MOD13 NDVI product. 40
- Figure 10. ASTER (left panels) and MODIS (right panels) LST uncertainty distributions plotted versus TCW and simulated LST for all end-member surface types (graybody, soils, sands, and rocks), for the TES algorithm including atmospheric error (TES+atm) and with the WVS method applied (TES+atm+wvs). 48
- Figure 11. Flow diagram showing all steps in the retrieval process in generating the MODIS MOD21 LST&E product starting with TIR at-sensor radiances and progressing through atmospheric correction, cloud detection, and the TES algorithm. 49
- Figure 12. Flow diagram of the TES algorithm in its entirety, including the NEM, RATIO, and MMD modules. Details are included in the text, including information about the refinement of *emax*. 50
- Figure 13. Clockwise from top left: MODIS cutouts of land surface emissivity for band 29 (8.55  $\mu\text{m}$ ); band 31 (11  $\mu\text{m}$ ), band 32 emissivity (12  $\mu\text{m}$ ), and LST output from the TES algorithm over the Imperial Valley, southeastern California on 29 August 2004. 55
- Figure 14. MODIS derived TES and NEM emissivity spectra for three different surface types for the MODIS cutout shown in Figure 11: Algodones Dunes, Salton Sea, and shrublands (mixed soil and vegetation). Details of the TES and NEM outputs from these spectra are shown in Table 7. 55
- Figure 15. MODIS and ASTER calibration curves of minimum emissivity vs. MMD. The lab data (crosses) are computed from 150 spectra consisting of a broad range of terrestrial materials (rocks, sand, soil, water, vegetation, and ice). 57
- Figure 16. Emissivity spectra comparisons on June 15, 2000 over the Salton Sea between ASTER (3-band), ASTER (5-band), and MODTES, using the TES algorithm along with lab spectra of water from the ASTER spectral library. Results from the WVS method and the STD atmospheric correction are also shown. An estimate of the PWV from the MOD07 atmospheric product indicates very high humidity on this day. 59
- Figure 17. Emissivity images (left) and surface temperature images (right) for ASTER (top), MODIS TES (MODTES) (center) and MODIS SW (MOD11\_L2) (bottom) products over the Station Fire burn scar just north of Pasadena, CA. Location of JPL in Pasadena and burn scar area indicated at top right. MODTES and ASTER results match closely; however, the MOD11\_L2 temperatures are underestimated by as much as 12 K, due to an incorrect emissivity classification. 61
- Figure 18. (left) ASTER band 12 (9.1  $\mu\text{m}$ ) emissivity image over Mauna Loa caldera, Hawaii on 5 June 2000, and (right) emissivity spectra from ASTER, MODTES, and MOD11 emissivity classification. While ASTER and

- MODTES agree closely, MOD11 emissivities are too high, resulting in large LST discrepancies between MODTES and MOD1 (12 K) due to misclassification in bands 31 (11  $\mu\text{m}$ ) and 32 (12  $\mu\text{m}$ ). 62
- Figure 19. (top) Emissivity variation for a rainfall event over the Namib desert showing results from MOD11B1 v4 (day/night algorithm), MOD11\_L2 (SW), and MODIS TES (MODTES). (bottom) Corresponding soil moisture variation from AMSRE-E and rainfall estimates from the Tropical Rainfall Measuring Mission (TRMM). It is clear that the physical retrievals, show increases in emissivity due to soil moisture, whereas the SW values are held constant throughout the rainfall period from 15–21 April. From Hulley et al. (2010). 63
- Figure 20. MODIS LST uncertainties using the TES algorithm versus TCW for four viewing Gaussian angles of  $0^\circ$ ,  $26.1^\circ$ ,  $40.3^\circ$ , and  $53.7^\circ$ . The value  $n$  represents the number of data points used for a specific land surface type, in this case bare surfaces (rocks, soils, sands). 71
- Figure 21. MODIS TES retrievals including WVS correction over the southwestern United States on 7 August 2004: (a) (top left) LST, (b) (top right) emissivity for band 29 (8.55  $\mu\text{m}$ ), (c) (bottom left) LST uncertainty, and (d) (bottom right) emissivity uncertainty for band 29 (8.55  $\mu\text{m}$ ). White areas over land indicate areas of cloud that have been masked out using the MOD35 cloud mask product. 74
- Figure 22. Figures showing the Emissivity retrievals for the MODIS Aqua MYD21 products over two water sites using data collected for three years of data for Lake Tahoe (2003-2005) and Salton Sea (2008-2010). Lab data, Lab data convolved with MODIS bands and the MOD11 bands 31 and 32 are also shown for comparison. 77
- Figure 23. An example of the LST validation applied to the MODIS Aqua MYD11 and MYD21 LST products over two water sites using three years of data collected Lake Tahoe (2003-2005) and Salton Sea (2008-2010). While MYD11 performs better than MYD21 at Lake Tahoe (0.5 vs 0.9 K), MYD21 performs better at Salton Sea (1.2 vs 1.5 K). 78
- Figure 24. Laboratory-measured emissivity spectra of sand samples collected at ten pseudo-invariant sand dune sites in the southwestern United States. The sites cover a wide range of emissivities in the TIR region. 80
- Figure 25. Figures showing the Emissivity retrievals for the MODIS Aqua MYD21 products over six pseudo-invariant sand dune sites using data collected for three years of data (2003-2005); Lab data, Lab data convolved with MODIS bands, and the MOD11 bands 31 and 32 emissivity are also shown for comparison. 81
- Figure 26. An example of the R-based validation method applied to the MODIS Aqua MYD11 and MYD21 LST products over six pseudo-invariant sand dune sites using all data during 2003-2005. AIRS profiles and lab-measured emissivities from samples collected at the sites were used for the R-based simulations. 85
- Figure 27. Histogram error plots showing validation of the R-based method applied to the MODIS Aqua MYD11 and MYD21 LST products over six pseudo-invariant sand dune sites using all data during 2003-2005. 86
- Figure 28. MYD21 Emissivity retrievals for band 31 at the two sites show small fluctuations within the error range of 1% from the mean values. The histograms on the margins show a consistently high density of the data around the mean for each of the sites. 87
- Figure 29. R-based validation for MODIS Aqua MYD11 and MYD21 LST products over Redwood and Texas Grassland sites (a, b) using three years of data collected (2003-2005). The bottom panels (c,d) show the histogram of the distribution of the LST error for both products showing comparable performances at the 1 K level in RMSE, although MYD21 is biased warm while MYD11 is biased cold. 88
- Figure 30. Figures showing the validation summary for LST retrievals for the MODIS Aqua MYD21 and MYD11 products over various IGBP sites using data collected for year 2003-2005, except for Salton Sea (2008-2010). 91

## Tables

Table 1: Geophysical data available in the MERRA analysis product. Columns under Mandatory specify if the variables is needed for determining atmospheric correction parameters. Data are output in 6hr analysis for 42 pressure levels at 0.5 degree x 0.625 degree spatial resolution. ....	24
Table 2: Geophysical data available in the NCEP GFS analysis product. Columns under Mandatory specify if the variables is needed for determining atmospheric correction parameters. Data are output in 3hr analysis for 26 pressure levels at 0.5 degree spatial resolution. ....	25
Table 3: MYD21 LST validation using matchups with Lake Tahoe in situ data during 2014 for three NWP models: ECMWF, MERRA2, NCEP GFS. (Bottom figure): Emissivity spectra matchups between VIIRS (VNP21) and lab spectra of sand samples collected at the Little Sahara sand dune validation site in Utah.....	27
Table 4. Percent changes in simulated at-sensor radiances for changes in input geophysical parameters for MODIS bands 29, 31, and 32, with equivalent change in brightness temperature in parentheses. ....	29
Table 5. MODIS-Terra band model parameters in Equation (8). ....	33
Table 6. MODIS-Terra regression coefficients for Equation (12). ....	33
Table 7. Output from various stages of the MODTES algorithm for three surface types: sand dunes, Salton Sea, and shrubland transition zone for a MODIS test scene over the Imperial Valley, southeastern California. ....	53
Table 8. The core set of global validation sites according to IGBP class to be used for validation and calibration of the MODIS MOD21 land surface temperature and emissivity product. ....	76
Table 9. Emissivity comparisons between lab, MYD11, and MYD21 at six sand sites for band 31.....	89
Table 10. R-based LST validation statistics from six pseudo-invariant sand dune sites using all MOD11 and MOD21 LST retrievals during 2005. ....	90

## 1 Introduction

This document outlines the theory and methodology for generating the Moderate Resolution Imaging Spectroradiometer (MODIS) Level-2 daily daytime and nighttime 1-km land surface temperature (LST) and emissivity product using the Temperature Emissivity Separation (TES) algorithm. The MODIS-TES (MXD21\_L2) product, will include the LST and emissivity for three MODIS thermal infrared (TIR) bands 29, 31, and 32, and will be generated for data from the NASA-EOS Terra AM (MOD21) and Aqua PM (MYD21) platforms. This is version 1.0 of the ATBD and the goal is maintaining a ‘living’ version of this document with changes made when necessary. The current standard baseline MODIS LST products (MXD11\*) are derived from the generalized split-window (SW) algorithm (Wan and Dozier 1996), which produces a 1-km LST product and two classification-based emissivities for bands 31 and 32; and a physics-based day/night algorithm (Wan and Li 1997), which produces a 5-km (C4) and 6-km (C5) LST product and emissivity for seven MODIS bands: 20, 22, 23, 29, 31–33.

The land surface temperature and emissivity (LST&E) are derived from the surface radiance that is obtained by atmospherically correcting the at-sensor radiance. LST&E data are used for many Earth surface related studies such as surface energy balance modeling (Zhou et al. 2003b) and land-cover land-use change detection (French et al. 2008), while they are also critical for accurately retrieving important climate variables such as air temperature and relative humidity (Yao et al. 2011). The LST is an important long-term climate indicator, and a key variable for drought monitoring over arid lands (Anderson et al. 2011a; Rhee et al. 2010). The LST is an input to ecological models that determine important variables used for water use management such as evapotranspiration and soil moisture (Anderson et al. 2011b). Multispectral emissivity retrievals are also important for Earth surface studies. For example, emissivity spectral signatures are important for geologic studies and mineral mapping studies (Hook et al. 2005; Vaughan et al. 2005). This is because emissivity features in the TIR region are unique for many different types of materials that make up the Earth’s surface, such as quartz, which is ubiquitous in most of the arid regions of the world. Emissivities are also used for land use and land cover change mapping since vegetation fractions can often be inferred if the background soil is observable (French et al. 2008). Accurate knowledge of the surface emissivity is critical for accurately recovering the LST, especially over land where emissivity variations can be large both spectrally and spatially.

The MODTES algorithm derives its heritage from the ASTER TES algorithm (Gillespie et al. 1998). ASTER is a five-channel multispectral TIR scanner that was launched on NASA's Terra spacecraft in December 1999 with a 90-m spatial resolution and revisit time of 16 days. The MxD21 LST&E products will be produced globally over all land cover types, excluding open oceans for all cloud-free pixels. The Level-2 products will be merged to produce gridded daily, weekly and monthly products, with the monthly product most likely producing global coverage, depending on cloud coverage. The generation of the higher level 3 merged products will be considered a project activity. The MxD21 Level 2 products will be initially inter-compared with the standard MXD11 products to identify regions and conditions for divergence between the products, and validation will be accomplished using a combination of temperature-based (T-based) and radiance-based (R-based) methods over dedicated field sites.

Maximum radiometric emission for the typical range of Earth surface temperatures, excluding fires and volcanoes, is found in two infrared spectral "window" regions: the midwave infrared (3.5–5  $\mu\text{m}$ ) and the thermal infrared (8–13  $\mu\text{m}$ ). The radiation emitted in these windows for a given wavelength is a function of both temperature and emissivity. Determining the separate contribution from each component in a radiometric measurement is an ill-posed problem since there will always be more unknowns— $N$  emissivities and a single temperature—than the number of measurements,  $N$ , available. For MODIS, we will be solving for one temperature and three emissivities (MODIS TIR bands 29, 31, and 32). To solve the ill-posed problem, an additional constraint is needed, independent of the data. There have been numerous theories and approaches over the past two decades to solve for this extra degree of freedom. For example, the ASTER Temperature Emissivity Working Group (TEWG) analyzed ten different algorithms for solving the problem (Gillespie et al. 1999). Most of these relied on a radiative transfer model to correct at-sensor radiance to surface radiance and an emissivity model to separate temperature and emissivity. Other approaches include the SW algorithm, which extends the sea-surface temperature (SST) SW approach to land surfaces, assuming that land emissivities in the window region (10.5–12  $\mu\text{m}$ ) are stable and well known. However, this assumption leads to unreasonably large errors over barren regions where emissivities have large variations both spatially and spectrally. The ASTER TEWG finally decided on a hybrid algorithm, termed the TES algorithm, which capitalizes on the strengths of previous algorithms with additional features (Gillespie et al. 1998).

TES is applied to the land-leaving TIR radiances that are estimated by atmospherically correcting the at-sensor radiance on a pixel-by-pixel basis using a radiative transfer model. TES uses an empirical relationship to predict the minimum emissivity that would be observed from a given spectral contrast, or minimum-maximum difference (MMD) (Kealy and Hook 1993; Matsunaga 1994). The empirical relationship is referred to as the calibration curve and is derived from a subset of spectra in the ASTER spectral library (Baldrige et al. 2009a). A MODIS calibration curve, applicable to MODIS TIR bands 29, 31, and 32 will be computed. Numerical simulations have shown that TES is able to recover temperatures within 1.5 K and emissivities within 0.015 for a wide range of surfaces and is a well-established physical algorithm that produces seamless images with no artificial discontinuities such as might be seen in a land classification type algorithm (Gillespie et al. 1998).

The remainder of the document will discuss the MODIS instrument characteristics, provide a background on TIR remote sensing, give a full description and background on the TES algorithm, provide quality assessment, discuss numerical simulation studies and uncertainty analysis, and, finally, outline a validation plan.

## **2 MODIS Background**

The MODIS sensors on NASA's Terra (AM) and Aqua (PM) platforms are currently the flagship instruments for global studies of Earth's surface, atmosphere, cryosphere, and ocean processes (Justice et al. 1998; Salomonson et al. 1989). In terms of LST&E products, the strength of the MODIS is its ability to retrieve daily data at 1 km for both day- and nighttime observations on a global scale.

### **2.1 Calibration**

There are now multiple satellite sensors that measure the mid- and thermal infrared radiance emitted from the Earth's surface in multiple spectral channels. These sensors include the Advanced Along Track Scanning Radiometer (AATSR), ASTER, Advanced Very High Resolution Radiometer (AVHRR), and MODIS instruments. A satellite calibration interconsistency study is currently underway for evaluating the interconsistency of these sensors at the Lake Tahoe and Salton Sea cal/val sites. This effort has indicated that further work is needed

to consistently inter-calibrate the ATSR series and AVHRR series whereas ASTER and MODIS have a clearly defined calibration and well-understood performance.

In-flight performance of TIR radiance data (3–14  $\mu\text{m}$ ) used in LST&E products is typically determined through comparison with ground validation sites. Well-established automated validation sites at Lake Tahoe, CA/NV, and Salton Sea, CA have been used to validate the TIR data from numerous sensors including ASTER and MODIS (Hook et al. 2007). Results from this work demonstrate that the MODIS (Terra and Aqua) instruments have met their required radiometric calibration accuracy of 0.5–1% in the TIR bands used to retrieve LST&E with differences of  $\pm 0.25\%$  ( $\sim 0.16\text{K}$ ) for the lifetime of the missions. Similar work for ASTER indicates its performance also meets the 1% requirements, provided additional steps are taken to account for drift between calibrations (Tonooka et al. 2005).

## 2.2 Instrument Characteristics

The MODIS instrument acquires data in 36 spectral channels in the visible, near infrared, and infrared wavelengths. Infrared channels 20, 22, 23, 29, 31, and 32 are centered on 3.79, 3.97, 4.06, 8.55, 11.03, and 12.02  $\mu\text{m}$  respectively. Channels 29, 31, and 32 are the focus of the MODTES algorithm. MODIS scans  $\pm 55^\circ$  from nadir and provides daytime and nighttime imaging of any point on the Earth every 1–2 days with a continuous duty cycle. MODIS data are quantized in 12 bits and have a spatial resolution of  $\sim 1$  km at nadir. They are calibrated with a cold space view and full aperture blackbody viewed before and after each Earth view. A more detailed description of the MODIS instrument and its potential application can be found in Salomonson et al. (1989) and Barnes et al. (1998). The MODIS sensor is flown on the Terra and Aqua spacecraft launched in 1999 and 2002, respectively.

## 2.3 LST&E Standard Products

Current standard LST&E products (MOD11 from Terra, and MYD11 from Aqua) are generated by two different algorithms: a generalized split-window (GSW) algorithm (product MOD11\_L2) (Wan and Dozier 1996) that produces LST data at 1-km resolution, and a day/night algorithm (product MOD11B1) (Wan and Li 1997) that produces LST&E data at  $\sim 5$  km (C4) and  $\sim 6$  km (C5) resolution.

The GSW algorithm extends the SST SW approach to land surfaces. In this approach the emissivity of the surface is assumed to be known based on an *a priori* classification of the Earth

surface into a selected number of cover types and a dual or multichannel SW algorithm is used in much the same way as with the oceans. This approach has been adopted by the MODIS and VIIRS emissivity product teams. The MODIS algorithm estimates the emissivity of each pixel by consulting the MODIS land cover product (MOD12Q1) whose values are associated with laboratory-measured emissivity spectra (Snyder et al. 1998). Adjustments are made for TIR BRDF, snow (from MOD10\_L2 product), and green vs. senescent vegetation. The *a priori* approach works well for surfaces whose emissivity can be correctly assigned based on the classification but less well for surfaces whose emissivities differ from the assigned emissivity. Specifically, it is best suited for land-cover types such as dense evergreen canopies, lake surfaces, snow, and most soils, all of which have stable emissivities known to within 0.01. It is significantly less reliable over arid and semi-arid regions.

The day/night approach uses pairs of daytime and nighttime observations in seven MODIS mid-infrared (MIR) and TIR bands (bands 20, 22, 23, 29, and 31–33) to simultaneously retrieve LST&E. This approach was designed to overcome the ill-posed thermal retrieval problem (where there are always more unknowns than independent equations in a given sample) by using two independent samples of the same target separated in time. The resulting system of equations can then be solved, provided several key assumptions are met. These include: a) the difference in surface temperature between the two samples must be large; b) the surface conditions (i.e., the emissivity spectrum) must not change between day and night samples; c) the geolocation of the samples must be highly accurate; and d) emissivity angular anisotropy must not be significant. In summary, it assumes that differences in the spectral radiances between the two samples are caused by surface temperature change and nothing else. In the MODIS implementation, the cloud-free day/night samples must be within 32 days of each other. The day-night approach is more complicated to implement due to data storing; however, it is considered preferable to the *a priori* method in areas where emissivity is difficult to accurately predict—most notably in semi-arid and arid areas. This algorithm is not well suited for polar regions since the signal-to-noise of observations in band 20 of the MIR are unacceptably low. Similarly, this product has limitations over very warm targets (e.g., arid and semi-arid regions) due to saturation of the MIR bands.

Two methods have been used for validating MODIS LST data products; these are a conventional T-based method and an R-based method (Wan and Li 2008). The T-based method requires ground measurements over thermally homogenous sites concurrently with the satellite

overpass, while the R-based method relies on a radiative closure simulation in a clear atmospheric window region to estimate the LST from top of atmosphere (TOA) observed brightness temperatures, assuming the emissivity is known from ground measurements. The MOD11\_L2 LST product has been validated with a combination of T-based and R-based methods over more than 19 types of thermally homogenous surfaces such as lakes (Hook et al. 2007), at dedicated field campaign sites over agricultural fields and forests (Coll et al. 2005), playas and grasslands (Wan et al. 2004; Wan 2008), and for a range of different seasons and years. LST errors are generally within  $\pm 1$  K for all sites under stable atmospheric conditions except semi-arid and arid areas that had errors of up to 5 K (Wan and Li 2008).

At the University of Wisconsin, a monthly MODIS global infrared land surface emissivity database (UWIREMIS) has been developed based on the standard MOD11B1 emissivity product (Seemann et al. 2008) at ten wavelengths (3.6, 4.3, 5.0, 5.8, 7.6, 8.3, 9.3, 10.8, 12.1, and 14.3  $\mu\text{m}$ ) with 5 km spatial resolution. The baseline fit method, based on a conceptual model developed from laboratory measurements of surface emissivity, is applied to fill in the spectral gaps between the six available MODIS/MYD11 bands. The ten wavelengths in the UWIREMIS emissivity database were chosen as hinge points to capture as much of the shape of the higher resolution emissivity spectra as possible, and extended by Borbas et al. (2007) to provide 416 spectral points from 3.6 to 14.3  $\mu\text{m}$ . The algorithm is based on a Principal Component Analyses (PCA) regression using the eigenfunction representation of high spectral resolution laboratory measurements from the ASTER spectral library (Baldrige et al. 2009a).

### **3 Earth Science Relevance**

LST&E are key variables for explaining the biophysical processes that govern the balances of water and energy at the land surface. LST&E data are used in many research areas including ecosystem models, climate models, cryospheric research, and atmospheric retrievals schemes. Our team has been carefully selected to include expertise in these areas. The descriptions below summarize how LST&E data are typically used in these areas.

#### **3.1 Use of LST&E in Climate/Ecosystem Models**

Emissivity is a critical parameter in climate models that determine how much thermal radiation is emitted back to the atmosphere and space and therefore is needed in surface radiation budget calculations, and also to calculate important climate variables such as LST (e.g., Jin and Liang 2006; Zhou et al. 2003b). Current climate models represent the land surface emissivity by either a constant value or very simple parameterizations due to the limited amount of suitable data. Land surface emissivity is prescribed to be unity in the Global Climate Models (GCMs) of the Center for Ocean-Land-Atmosphere Studies (COLA) (Kinter et al. 1988), the Chinese Institute of Atmospheric Physics (IAP) (Zeng et al. 1989), and the US National Meteorological Center (NMC) Medium-Range Forecast (MRF). In the recently developed NCAR Community Land Model (CLM3) and its various earlier versions (Bonan et al. 2002; Oleson et al. 2004), the emissivity is set as 0.97 for snow, lakes, and glaciers, 0.96 for soil and wetlands, and vegetation is assumed to be black body. For a broadband emissivity to correctly reproduce surface energy balance statistics, it needs to be weighted both over the spectral surface blackbody radiation and over the downward spectral sky radiances and used either as a single value or a separate value for each of these terms. This weighting depends on the local surface temperatures and atmospheric composition and temperature. Most simply, as the window region dominates the determination of the appropriate single broadband emissivity, an average of emissivities over the window region may suffice.

Climate models use emissivity to determine the net radiative heating of the canopy and underlying soil and the upward (emitted and reflected) thermal radiation delivered to the atmosphere. The oversimplified representations of emissivity currently used in most models introduce significant errors in the simulations of climate. Unlike what has been included in climate models up to now, satellite observations indicate large spatial and temporal variations in land surface emissivity with surface type, vegetation amount, and soil moisture, especially over deserts

and semi-deserts (Ogawa 2004; Ogawa et al. 2003). This variability of emissivity can be constructed by the appropriate combination of soil and vegetation components.

Sensitivity tests indicate that models can have an error of 5–20  $\text{Wm}^{-2}$  in their surface energy budget for arid and semi-arid regions due to their inadequate treatment of emissivity (Jin and Liang 2006; Zhou et al. 2003b), a much larger term than the surface radiative forcing from greenhouse gases. The provision, through this proposal, of information on emissivity with global spatial sampling will be used for optimal estimation of climate model parameters. A climate model, in principle, constructs emissivity at each model grid square from four pieces of information: a) the emissivity of the underlying soil; b) the emissivity of the surfaces of vegetation (leaves and stems); c) the fraction of the surface that is covered by vegetation; and d) the description of the areas and spatial distribution of the surfaces of vegetation needed to determine what fraction of surface emission will penetrate the canopy. Previously, we have not been able to realistically address these factors because of lack of suitable data. The emissivity datasets developed for this project will be analyzed with optimal estimation theory that uses the spatial and temporal variations of the emissivity data over soil and vegetation to constrain more realistic emissivity schemes for climate models. In doing so, land surface emissivity will be linked to other climate model parameters such as fractional vegetation cover, leaf area index, snow cover, soil moisture, and soil albedo, as explored in Zhou et al. (2003a). The use of more realistic emissivity values will greatly improve climate simulations over sparsely vegetated regions as previously demonstrated by various sensitivity tests (e.g., Jin and Liang 2006; Zhou et al. 2003b). In particular, both daily mean and day-to-night temperature ranges are substantially impacted by the model's treatment of emissivity.

### **3.2 Use of LST&E in Cryospheric Research**

Surface temperature is a sensitive energy-balance parameter that controls melt and energy exchange between the surface and the atmosphere. Surface temperature is also used to monitor melt zones on glaciers and can be related to the glacier facies of (Benson 1996), and thus to glacier or ice sheet mass balance (Hall et al. 2006). Analysis of the surface temperature of the Greenland Ice Sheet and the ice caps on Greenland provides a method to study trends in surface temperature as a surrogate for, and enhancement of, air-temperature records, over a period of decades (Comiso 2006). Maps of LST of the Greenland Ice Sheet have been developed using the MODIS 1-km LST standard product, and trends in mean LST have been measured (Hall et al. 2008). Much attention has been paid recently to the warming of the Arctic in the context of global warming. Comiso

(2006) shows that the Arctic region, as a whole, has been warming at a rate of  $0.72 \pm 0.10^{\circ}\text{C}$  per decade from 1981–2005 inside the Arctic Circle, though the warming pattern is not uniform. Furthermore, various researchers have shown a steady decline in the extent of the Northern Hemisphere sea ice, both the total extent and the extent of the perennial or multiyear ice (Parkinson et al. 1999). Increased melt of the margins of the Greenland Ice Sheet has also been reported (Abdalati and Steffen 2001).

Climate models predict enhanced Arctic warming but they differ in their calculations of the magnitude of that warming. The only way to get a comprehensive measurement of surface-temperature conditions over the Polar Regions is through satellite remote sensing. Yet errors in the most surface temperature algorithms have not been well-established. Limitations include the assumed emissivity, effect of cloud cover, and calibration consistency of the longer-term satellite record.

Comparisons of LST products over snow and ice features reveal LST differences in homogeneous areas of the Greenland Ice Sheet of  $>2^{\circ}\text{C}$  under some circumstances. Because there are many areas that are within a few degrees of  $0^{\circ}\text{C}$ , such as the ice-sheet margin in southern Greenland, it is of critical importance to be able to measure surface temperature from satellites accurately. Ice for which the mean annual temperature is near the freezing point is highly vulnerable to rapid melt.

### **3.3 Use of LST&E in Atmospheric Retrieval Schemes**

The atmospheric constituent retrieval community and numerical weather prediction operational centers are expected to benefit from the development of a unified land surface emissivity product. The retrieval of vertical profiles of air temperature and water vapor mixing ratio in the atmospheric boundary layer over land is sensitive to the assumptions used about the infrared emission and reflection from the surface. Even the retrieval of clouds and aerosols over land using infrared channels is complicated by uncertainties in the spectral dependence of the land surface emission. Moreover, weather models improve their estimates of atmospheric temperature and composition by comparisons between observed and model calculated spectral radiances, using an appropriate data assimilation (1D-Var) framework. The model generates forward calculation of radiances by use of their current best estimate of temperature profiles, atmospheric composition, and surface temperature and emissivity. If good prior estimates of infrared emissivity can be

provided along with their error characterization, what would otherwise be a major source of error and bias in the use of the satellite radiances in data assimilation can be minimized.

## 4 Thermal Infrared Radiative Transfer

### 4.1 Thermal Infrared Radiance

The at-sensor measured radiance in the TIR spectral region (7–14  $\mu\text{m}$ ) is a combination of three primary terms: the Earth-emitted radiance, reflected downwelling sky irradiance, and atmospheric path radiance. The Earth-emitted radiance is a function of temperature and emissivity and gets attenuated by the atmosphere on its path to the satellite. The atmosphere also emits radiation, some of which reaches the sensor directly as “path radiance,” while some gets radiated to the surface (irradiance) and reflected back to the sensor, commonly known as the reflected downwelling sky irradiance. Reflected solar radiation in the TIR region is negligible (Figure 1) and a much smaller component than the surface-emitted radiance. One effect of the sky irradiance is the reduction of the spectral contrast of the emitted radiance, due to Kirchhoff’s law. Assuming the spectral variation in emissivity is small (Lambertian assumption), and using Kirchhoff’s law to express the hemispherical-directional reflectance as directional emissivity ( $\rho_\lambda = 1 - \epsilon_\lambda$ ), the clear-sky at-sensor radiance can be written as three terms: the Earth-emitted radiance described by Planck’s function and reduced by the emissivity factor,  $\epsilon_\lambda$ ; the reflected downwelling irradiance; and the path radiance.

$$L_\lambda(\theta) = [\epsilon_\lambda B_\lambda(T_s) + (1 - \epsilon_\lambda)L_\lambda^\downarrow] \tau_\lambda(\theta) + L_\lambda^\uparrow(\theta) \quad (1)$$

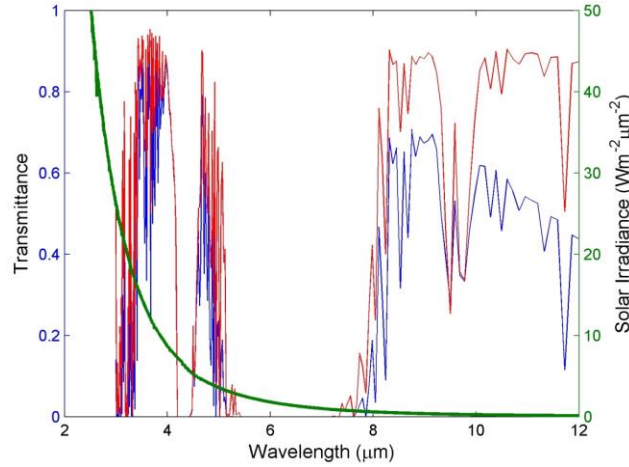


**Figure 1. Simulated atmospheric transmittance for a US Standard Atmosphere (red) and tropical atmosphere (blue) in the 3–12 μm region. Also shown is the solar irradiance contribution  $W/m^2/\mu m^2$ .**

Where:

$L_{\lambda}(\theta)$  = at-sensor radiance;

$\lambda$  = wavelength;

$\theta$  = observation angle;

$\epsilon_{\lambda}$  = surface emissivity;

$T_s$  = surface temperature;

$L_{\lambda}^{\downarrow}$  = downwelling sky irradiance;

$\tau_{\lambda}(\theta)$  = atmospheric transmittance;

$L_{\lambda}^{\uparrow}(\theta)$  = atmospheric path radiance

$B_{\lambda}(T_s)$  = Planck function, described by Planck's law:

$$B_{\lambda} = \frac{c_1}{\pi\lambda^5} \left( \frac{1}{\exp\left(\frac{c_2}{\lambda T}\right) - 1} \right) \quad (2)$$

$c_1 = 2\pi hc^2 = 3.74 \cdot 10^{-16} \text{ W}\cdot\text{m}^2$  (1<sup>st</sup> radiation constant)

$h = 6.63 \cdot 10^{-34} \text{ W}\cdot\text{s}^2$  (Planck's constant)

$c_2 = h \cdot c/k = 1.44 \times 10^4 \text{ }\mu\text{m}\cdot\text{K}$  (2<sup>nd</sup> radiation constant)

$k = 1.38 \times 10^{-23} \text{ W}\cdot\text{s}\cdot\text{K}^{-1}$  (Boltzmann's constant)

$c = 2.99 \cdot 10^8 \text{ m}\cdot\text{s}^{-1}$  (speed of light)

Figure 2 shows the relative contributions from the surface-emission term, surface radiance, and at-sensor radiance for a US Standard Atmosphere, quartz emissivity spectrum, and surface temperature set to 300 K. Vertical bars show the center placement of the three MODIS TIR bands 29 (8.55  $\mu\text{m}$ ), 31 (11  $\mu\text{m}$ ), and 32 (12  $\mu\text{m}$ ). The reflected downwelling term adds a small contribution in the window regions but will become more significant for more humid atmospheres. The at-sensor radiance shows large departures from the surface radiance in regions where atmospheric absorption from gases such as  $\text{CO}_2$ ,  $\text{H}_2\text{O}$ , and  $\text{O}_3$  are high.

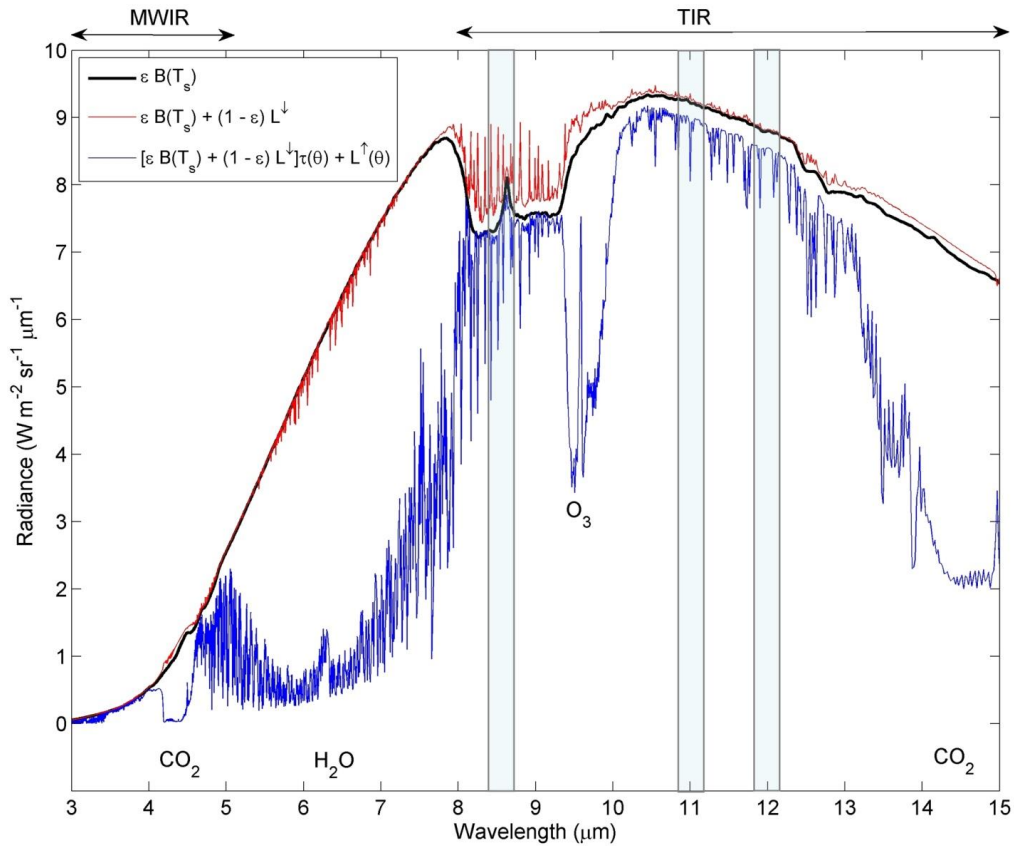


**Figure 2. Radiance simulations of the surface-emitted radiance, surface-emitted and reflected radiance, and at-sensor radiance using the MODTRAN 5.2 radiative transfer code, US Standard Atmosphere, quartz emissivity spectrum, surface temperature = 300 K, and viewing angle set to nadir. Vertical bars show placements of the MODIS TIR bands 29 (8.55  $\mu\text{m}$ ), 31 (11  $\mu\text{m}$ ), and 32 (12  $\mu\text{m}$ ).**

Equation (1) gives the at-sensor radiance for a single wavelength,  $\lambda$ , while the measurement from a sensor is typically measured over a range of wavelengths, or band. The at-sensor radiance for a discrete band,  $i$ , is obtained by weighting and normalizing the at-sensor

spectral radiance calculated by Equation (1) with the sensor's spectral response function for each band,  $Sr_\lambda$ , as follows:

$$L_i(\theta) = \frac{\int Sr_\lambda(i) \cdot L_\lambda(\theta) \cdot d\lambda}{Sr_\lambda(i) \cdot d\lambda} \quad (3)$$

Using Equations (1) and (3), the surface radiance for band  $i$  can be written as a combination of two terms: Earth-emitted radiance, and reflected downward irradiance from the sky and surroundings:

$$L_{S,i} = \epsilon_i B_i(T_s) + (1 - \epsilon_i) L_i^\downarrow = \frac{L_i(\theta) - L_i^\uparrow(\theta)}{\tau_i(\theta)} \quad (4)$$

The atmospheric parameters,  $L_\lambda^\downarrow$ ,  $\tau_\lambda(\theta)$ ,  $L_\lambda^\uparrow(\theta)$ , are estimated with a radiative transfer model such as RTTOV or MODTRAN (Kneizys et al. 1996) discussed in the next section, using input atmospheric fields of air temperature, relative humidity, and geopotential height. Figure 3 shows MODIS spectral response functions for bands 29 (red), 31 (green) and 32 (blue) plotted with a typical transmittance curve for a mid-latitude summer atmosphere.

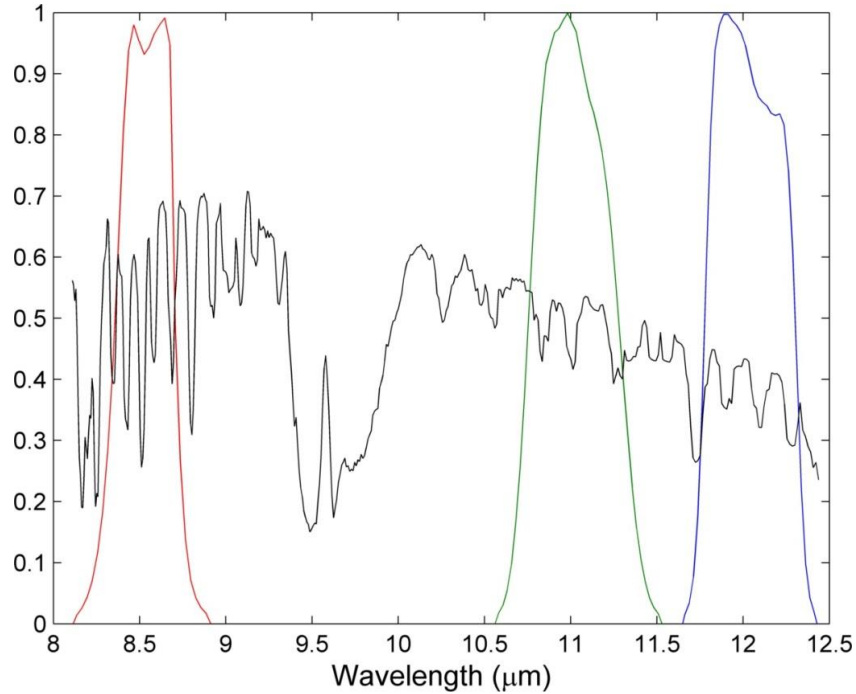


**Figure 3. MODIS spectral response functions for bands 29 (red), 31 (green), and 32 (blue) plotted with a typical transmittance curve for a mid-latitude summer atmosphere.**

## 4.2 Emissivity

The emissivity of an isothermal, homogeneous emitter is defined as the ratio of the actual emitted radiance to the radiance emitted from a black body at the same thermodynamic temperature (Norman and Becker 1995),  $\epsilon_{\lambda} = R_{\lambda}/B_{\lambda}$ . The emissivity is an intrinsic property of the Earth's surface and is an independent measurement of the surface temperature, which varies with irradiance and local atmospheric conditions. The emissivity of most natural Earth surfaces for the TIR wavelength ranges between 8 and 12  $\mu\text{m}$  and, for a sensor with spatial scales  $<100$  m, varies from  $\sim 0.7$  to close to 1.0. Narrowband emissivities less than 0.85 are typical for most desert and semi-arid areas due to the strong quartz absorption feature (reststrahlen band) between the 8- and 9.5- $\mu\text{m}$  range, whereas the emissivity of vegetation, water, and ice cover are generally greater than 0.95 and spectrally flat in the 8–12- $\mu\text{m}$  range.

## 5 Atmospheric Correction

The general methodology for atmospherically correcting the MODIS TIR data will be based largely on the methods that were developed for the ASTER instrument (Palluconi et al. 1999). However, significant improvements will be made by taking advantage of newly developed techniques and more advanced algorithms to improve accuracy. Currently two options for atmospheric profile sources are available: 1) interpolation of data assimilated from Numerical Weather Prediction (NWP) models, and 2) retrieved atmospheric geophysical profiles from remote-sensing data. The NWP models use current weather conditions, observed from various sources (e.g., radiosondes, surface observations, and weather satellites) as input to dynamic mathematical models of the atmosphere to predict the weather. Data are typically output in 6-hour increments, e.g., 00, 06, 12, and 18 UTC. Examples include: the Global Data Assimilation System (GDAS) product provided by the National Centers for Environmental Prediction (NCEP) (Kalnay et al. 1990); the Modern Era Retrospective-analysis for Research and Applications (MERRA) product provided by the Goddard Earth Observing System Data Assimilation System Version 5.2.0 (GEOS-5.2.0) (Bosilovich et al. 2008); and the European Center for Medium-Range Weather Forecasting (ECMWF), which is supported by more than 32 European states. Remote sensing data, on the other hand, are available real-time, typically twice daily and for clear-sky conditions. The principles of inverse theory are used to estimate a geophysical state (e.g., atmospheric temperature)

by measuring the spectral emission and absorption of some known chemical species such as carbon dioxide in the thermal infrared region of the electromagnetic spectrum (i.e., the observation). Examples of current remote-sensing data include the Atmospheric Infrared Sounder (AIRS) (Susskind et al. 2003) and Moderate Resolution Imaging Spectroradiometer (MODIS) (Justice and Townshend 2002), both on NASA's Aqua satellite launched in 2002.

The standard ASTER atmospheric correction technique, which is operated at the Land Processes Distributed Active Archive Center (LP DAAC) at the EROS Center in Sioux Falls, SD, uses input atmospheric profiles from the NCEP GDAS product at 1° spatial resolution and 6-hour intervals. An interpolation scheme in both space and time is required to characterize the atmospheric conditions for an ASTER image on a pixel-by-pixel basis.

## 5.1 Radiative Transfer Model

With the next generation's state-of-the-art, mid- and long-wave infrared (IR) hyperspectral sensors due for launch in the next decade, there has been greater demand for higher resolution and quality radiative transfer modeling. The current choice of radiative transfer model for atmospherically correcting MODIS TIR data is the latest version of the radiative transfer model called RTTOV. It is a very fast radiative transfer model for nadir-viewing passive visible, infrared and microwave satellite radiometers, spectrometers and interferometers (Saunders et al. 1999). RTTOV is written in FORTRAN-90 code, for simulating satellite radiances, designed to be incorporated within users' applications. RTTOV was originally developed at ECMWF in the early 90's for TOVS (Eyre and Woolf 1988). Subsequently, the original code has gone through several developments (Matricardi et al. 2001; Saunders et al. 1999), more recently within the EUMETSAT NWP Satellite Application Facility (SAF), of which RTTOV v11 is the latest version. It is actively developed by ECMWF and UK Met Office. RTTOV has been sufficiently tested and validated and is conveniently fast for full scale retrievals (Matricardi 2009). A number of satellite sensors are supported from various platforms

(e.g. <https://nwp-saf.eumetsat.int/site/software/rttov/documentation/platforms-supported/>). Given an atmospheric profile of temperature, water vapor and optionally other trace gases (for example ozone and carbon dioxide) together with satellite and solar zenith angles and surface temperature, pressure and optionally surface emissivity and reflectance, RTTOV will compute the top of

atmosphere radiances in each of the channels of the sensor being simulated. Users can also specify the selected channels to be simulated.

Mathematically, in vector notation, given a state vector,  $\mathbf{x}$ , which describes the atmospheric/surface state as a profile and surface variables the radiance vector,  $\mathbf{y}$ , for all the channels required to be simulated is given by (Saunders et al. 1999):

$$\mathbf{y} = H(\mathbf{x}) \quad (5)$$

where  $H$  is the radiative transfer model, i.e. RTTOV (also referred to as the observation operator in data assimilation parlance). This is known as the 'direct' or 'forward' model.

An important feature of the RTTOV model is that it not only performs the fast computation of the forward (or direct) clear-sky radiances but also the fast computation of the gradient of the radiances with respect to the state vector variables for the input state vector values. The Jacobian matrix  $\mathbf{H}$  which gives the change in radiance  $\delta\mathbf{y}$  for a change in any element of the state vector  $\delta\mathbf{x}$  assuming a linear relationship about a given atmospheric state  $\mathbf{x}_0$ :

$$\delta\mathbf{y} = \mathbf{H}(\mathbf{x}_0)\delta\mathbf{x} \quad (6)$$

The elements of  $\mathbf{H}$  contain the partial derivatives  $\frac{\partial y_i}{\partial x_j} \left( \frac{dy_i}{dx_j} \right)$  where the subscript  $i$  refers to channel number and  $j$  to position in state vector. The Jacobian gives the top of atmosphere radiance change for each channel from each level in the profile given a unit perturbation at any level of the profile vectors or in any of the surface/cloud parameters. It shows clearly, for a given profile, which levels in the atmosphere are most sensitive to changes in temperature and variable gas concentrations for each channel.

In RTTOV the transmittances of the atmospheric gases are expressed as a function of profile dependent predictors. This parameterization of the transmittances makes the model computationally efficient. The RTTOV fast transmittance scheme uses regression coefficients derived from accurate Line by Line computations to express the optical depths as a linear combination of profile dependent predictors that are functions of temperature, absorber amount, pressure and viewing angle (Matricardi and Saunders, 1999). The regression coefficients are computed using a training set of diverse atmospheric profiles chosen to represent the range of variations in temperature and absorber amount found in the atmosphere (Matricardi and Saunders, 1999; Chevallier ,2000; and Matricardi ,2008, 2009). The selection of the predictors is made according to the coefficients file supplied to the program.

**Table 1: Geophysical data available in the MERRA analysis product. Columns under Mandatory specify if the variables is needed for determining atmospheric correction parameters. Data are output in 6hr analysis for 42 pressure levels at 0.5 degree x 0.625 degree spatial resolution.**

MERRA Analysis Data (inst6_3d_ana_Np)				
Geophysical fields		Required?	Available?	Remarks
time	Time	Yes	Yes	
lat	Latitude	Yes	Yes	
lon	Longitude	Yes	Yes	
nlev	nLevel	Yes	Yes	
p	Pressure	Yes	Yes	
t	Air Temperature	Yes	Yes	
q	Specific Humidity	Yes	Yes	
sp	Surface Pressure	Yes	Yes	
skt	Surface Temperature	Yes	No	T value at the first valid level above surface is used.
t2	Temperature at 2 m	Yes	No	T value at the first valid level above surface is used
q2	Specific Humidity at 2 m	Yes	No	Q value at the first valid level above surface is used
ism	Land Sea Mask	Yes	No	Auxiliary database
el	Elevation	Yes	No	Auxiliary database

## 5.2 Atmospheric Profiles

### 5.2.1 MERRA-2

MERRA-2 is a follow on product to the original MERRA project for the modern satellite era (1979-2015). It has been expanded to use new observations including MODIS, AVHRR, GPS Radio Occultation, OMI, and MLS. The latest enhancement include improved water vapor assimilation resulting in a balance between precipitation and evaporation. Therefore one of the major advancement is that it includes land surface forcing by observed precipitation. The MOD21 algorithm uses the MERRA-2 analysis data for its standard atmospheric correction. MERRA-2 data are output in 6hr analysis for 42 pressure levels at 0.5 degree x 0.625 degree spatial resolution. The MERRA-2 profiles are first interpolated in time to the MODIS observation using the [00 06 12 18Z] analysis observation hours before ingesting into RTTOV. Table 1 shows MERRA-2

**Table 2: Geophysical data available in the NCEP GFS analysis product. Columns under Mandatory specify if the variables is needed for determining atmospheric correction parameters. Data are output in 3hr analysis for 26 pressure levels at 0.5 degree spatial resolution.**

NCEP GSF Data (NCEP-GFS-03HR-ANC)				
Geophysical fields		Required?	Available?	Remarks
time	Time	Yes	Yes	
lat	Latitude	Yes	Yes	
lon	Longitude	Yes	Yes	
nlev	nLevel	Yes	Yes	
p	Pressure	Yes	Yes	
t	Air Temperature	Yes	Yes	
q	Specific Humidity	Yes	Yes	
sp	Surface Pressure	Yes	Yes	
skt	Surface Temperature	Yes	Yes	
t2	Temperature at 2 m	Yes	No	T value at the first valid level above surface is used
q2	Specific Humidity at 2 m	Yes	No	Q value at the first valid level above surface is used
ism	Land Sea Mask	Yes	No	Auxiliary database
el	Elevation	Yes	No	Auxiliary database

geophysical data available in the MERRA-2 analysis product and the variables required for the input data into RTTOV for the atmospheric correction.

The RTTOV output data of transmittance, path radiance, and sky irradiance are then gridded to the MODIS swath at 1-km resolution using a bicubic interpolation approach. It should be noted that the data interpolation could potentially introduce errors, especially in humid regions where atmospheric water vapor can vary on smaller spatial scales than the native resolution of the input MERRA data at 0.5°. The propagation of these atmospheric correction errors would result in band-dependent surface radiance errors in both spectral shape and magnitude, which in turn could result in errors of retrieved Level-2 products such as surface emissivity and temperature. This is one of the main reason that we implement a Water Vapor Scaling (WVS) approach to help mitigate these errors.

### 5.2.2 NCEP Global Forecast System (GFS)

Because MERRA-2 has a data latency of approximately one month, an additional source of atmospheric profiles is necessary to produce MxD21 in near real time (NRT) mode in sync with the other MODIS science products. For this we use NCEP's Global Forecast System (GFS). MxD21 products produced from this data will become available from the NASA LAADS server for the current two months of the mission period and subsequently reprocessed with MERRA-2 data upon availability and distributed to the NASA LDPAAC. This is to ensure consistency in the long-term data record with MERRA-2.

NCEP's GFS is produced by the NCEP global forecast system and provides initial and/or boundary conditions for NCEP's other models for regional, ocean and wave prediction systems for up to 16 days in advance, but with decreased spatial resolution after 10 days. The Global Data Assimilation System (GDAS) uses maximum amounts of satellite and conventional observations from global sources and generates initial conditions for the global forecasts. The global data assimilation and forecasts are made four times daily at 00, 06, 12 and 18 UTC at 0.5 deg spatial resolution. Details of the geophysical variables used are highlighted in Table 2.

### 5.2.3 Accuracy Assessment: NCEP versus MERRA2

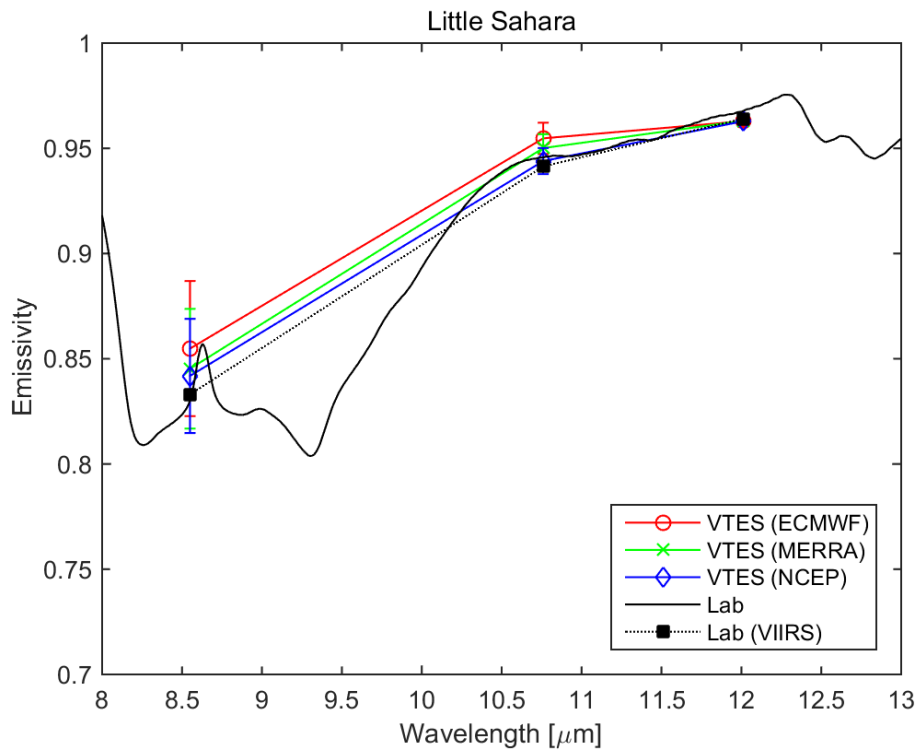
In order to better assess and quantify difference in MxD21 retrieval accuracy between using either NCEP or MERRA2 data for atmospheric correction, we validated the MYD21 LST retrievals with in situ data over Lake Tahoe during 2004, and validated the emissivity retrievals from the VIIRS VNP21 product using lab measured spectra of sand samples collected at the Little Sahara sand dune site in Utah. In addition we included ECMWF profile data as a third reference.

The results in Table 3 for Tahoe indicate a very close agreement in LST accuracy in terms of bias and RMSE between the three modes with RMSE's at the 1 K level and biases at the 1/10 K level. ECMWF had the lowest RMSE (1.06 K) when compared to MERRA2 (1.15 K) and NCEP (1.13), while MERRA-2 had the lowest bias when compared to NCEP/ECMWF. ECMWF data were never considered for use due to the difficulties in obtaining licence agreements. Emissivity matchups at Little Sahara show very close agreement with the lab data for all three NWP models, with NCEP and MERRA2 giving slightly better results than ECMWF, and matching the closest to within <1% emissivity accuracy of each other. Although not a comprehensive intercomparison study, these results nevertheless show reasonable agreement in

LST&E retrieval accuracy when using MERRA2 and NCEP data, and the near-real time product using NCEP GFS should produce very close to the similar accuracy as the standard product from MERRA2.

**Table 3: MYD21 LST validation using matchups with Lake Tahoe in situ data during 2014 for three NWP models: ECMWF, MERRA2, NCEP GFS. (Bottom figure): Emissivity spectra matchups between VIIRS (VNP21) and lab spectra of sand samples collected at the Little Sahara sand dune validation site in Utah.**

Site	NWP Model	Bias (K)	RMSE (K)
Lake Tahoe (2014)	ECMWF	-0.14	1.06
	MERRA2	-0.13	1.15
	NCEP	-0.23	1.13



#### 5.2.4 Transfer Sensitivity Analysis

The accuracy of the proposed atmospheric correction technique relies on the accuracy of the input variables to the model, such as air temperature, relative humidity, and ozone. The

combined uncertainties of these input variables need to be known if an estimate of the radiative transfer accuracy is to be estimated. These errors can be band-dependent, since different channels have different absorbing features and they are also dependent on absolute accuracy of the input profile data at different levels. The final uncertainty introduced is the accuracy of the radiative transfer model itself; however, this is expected to be small.

To perform the analysis, four primary input geophysical parameters were input to MODTRAN 5.2, and each parameter was changed sequentially in order to estimate the corresponding percent change in radiance (Palluconi et al. 1999). These geophysical parameters were air temperature, relative humidity, ozone, and aerosol visibility. Two different atmospheres were chosen, a standard tropical atmosphere and a mid-latitude summer atmosphere. These two simulated atmospheres should capture the realistic errors that we expect to see in humid conditions.

Typical values for current infrared sounder accuracies (e.g., AIRS) of air temperature and relative humidity retrievals in the boundary layer were used for the perturbations: 1) air temperature of 2 K, 2) relative humidity of 20%, 3) ozone was doubled, and 4) aerosol visibility was changed from rural to urban class. Numerical weather models such as NCEP would most likely have larger uncertainties in the 1–2 K range for air temperature and 10–20% for relative humidity (Kalnay et al. 1990).

Table 4 shows the results for three simulated MODIS bands 29, 31, and 32 expressed as percent change in radiance (equivalent brightness temperature change in parentheses) for two standard atmospheric regimes, tropical and mid-latitude summer. The results show that band 29 is in fact most sensitive to perturbations in air temperature, followed by band 31 and 32 for both atmospheric profiles, with the mid-latitude profile having larger changes than tropical. For a 20% change in humidity the reverse is true, band 32 having the largest change of nearly 3 K for a tropical atmosphere, followed by band 31 and 29. This is because band 32 falls closest to strong water lines above 12  $\mu\text{m}$ , as shown in Figure 2. Doubling the ozone results in a much larger sensitivity for band 5, since it is closest to the strong ozone absorption feature centered around the 9.5- $\mu\text{m}$  region as shown in Figure 2. Changing the aerosol visibility from rural to urban had a small effect on each band but was largest for band 5. Generally, the radiance in the thermal infrared region is insensitive to aerosols in the troposphere so, for the most part, a climatology-based estimate of aerosols would be sufficient. However, when stratospheric aerosol amounts increase

substantially due to volcanic eruptions, for example, then aerosol amounts from future NASA remote-sensing missions such as ACE and GEO-CAPE would need to be taken into account.

**Table 4. Percent changes in simulated at-sensor radiances for changes in input geophysical parameters for MODIS bands 29, 31, and 32, with equivalent change in brightness temperature in parentheses.**

Geophysical Parameter	Change in Parameter	% Change in Radiance (Tropical Atmosphere)			% Change in Radiance (Mid-lat Summer Atmosphere)		
		Band 29 (8.5 $\mu\text{m}$ )	Band 31 (11 $\mu\text{m}$ )	Band 32 (12 $\mu\text{m}$ )	Band 29 (8.5 $\mu\text{m}$ )	Band 31 (11 $\mu\text{m}$ )	Band 32 (12 $\mu\text{m}$ )
Air Temperature	+2 K	-2.8 (1.44 K)	-1.97 (1.31 K)	-1.62 (1.15 K)	-3.27 (1.64 K)	-2.50 (1.61 K)	-2.13 (1.49 K)
Relative Humidity	+20%	3.51 (1.76 K)	3.91 (2.54 K)	4.43 (3.09 K)	2.76 (1.35 K)	3.03 (1.93 K)	3.61 (2.48 K)
Ozone	$\times 2$	0.69 (0.35 K)	0.00 (0 K)	0.02 (0.01 K)	0.69 (0.34 K)	0.00 (0 K)	0.02 (0.02 K)
Aerosol	Urban/Rural	0.42 (0.21 K)	0.27 (0.17 K)	0.22 (0.16 K)	0.43 (0.21 K)	0.29 (0.19 K)	0.25 (0.17 K)

It should also be noted, as discussed in Palluconi et al. (1999), that in reality these types of errors may have different signs, change with altitude, and/or have cross-cancellation between the parameters. As a result, it is difficult to quantify the exact error budget for the radiative transfer calculation; however, what we do know is that the challenging cases will involve warm and humid atmospheres where distributions of atmospheric water vapor are the most uncertain.

## 6 Water Vapor Scaling (WVS) Method

The accuracy of the TES algorithm is limited by uncertainties in the atmospheric correction, which result in a larger apparent emissivity contrast. This intrinsic weakness of the TES algorithm has been systemically analyzed by several authors (Coll et al. 2007; Gillespie et al. 1998; Gustafson et al. 2006; Hulley and Hook 2009b; Li et al. 1999), and its effect is greatest over graybody surfaces that have a true spectral contrast that approaches zero. In order to minimize atmospheric correction errors, a Water Vapor Scaling (WVS) method has been introduced to improve the accuracy of the water vapor atmospheric profiles on a band-by-band basis for each observation using an Extended Multi-Channel/Water Vapor Dependent (EMC/WVD) algorithm (Tonooka 2005), which is an extension of the Water Vapor Dependent (WVD) algorithm (Francois and Otle 1996). The EMC/WVD equation models the at-surface brightness temperature, given the at-sensor brightness temperature, along with an estimate of the total water vapor amount:

$$T_{g,i} = \alpha_{i,0} + \sum_{k=1}^n \alpha_{i,k} T_k \quad (7)$$

$$\alpha_{i,k} = p_{i,k} + q_{i,k} W + r_{i,k} W^2,$$

where:

$i$	Band number
$n$	Number of bands
$W$	Estimate of total precipitable water vapor (cm)
$p, q, r$	Regression coefficients for each band
$T_k$	Brightness temperature for band k (K)
$T_{g,i}$	Brightness surface temperature for band, $i$

The coefficients of the EMC/WVD equation are determined using a global-based simulation model with atmospheric data from the NCEP Climate Data Assimilation System (CDAS) reanalysis project (Tonooka 2005).

The scaling factor,  $\gamma$ , used for improving a water profile, is based on the assumption that the transmissivity,  $\tau_i$ , can be express by the Pierluissi double exponential band model formulation. The scaling factor is computed for each gray pixel on a scene using  $T_{g,i}$  computed from Equation (7) and  $\tau_i$  computed using two different  $\gamma$  values that are selected *a priori*:

$$\gamma^i = \frac{\ln \left( \frac{\tau_i(\theta, \gamma_2)^{\gamma_1 \beta_i}}{\tau_i(\theta, \gamma_1)^{\gamma_2 \beta_i}} \cdot \left( \frac{B_i(T_{g,i}) - L_i^\uparrow(\theta, \gamma_1)/(1 - \tau_i(\theta, \gamma_1))}{L_i - L_i^\uparrow(\theta, \gamma_1)/(1 - \tau_i(\theta, \gamma_1))} \right)^{\gamma_1 \beta_i - \gamma_2 \beta_i} \right)}{\ln(\tau_i(\theta, \gamma_2)/\tau_i(\theta, \gamma_1))} \quad (8)$$

where:

$\beta_i$	Band model parameter (Table 5)
$\gamma_1, \gamma_2$	Two appropriately chosen $\gamma$ values
$\tau_i(\theta, \gamma_{1,2})$	Transmittance calculated with water vapor profile scaled by $\gamma$
$L_i^\uparrow(\theta, \gamma_{1,2})$	Path radiance calculated with water vapor profile scaled by $\gamma$

Typical values for  $\gamma$  are  $\gamma_1 = 1$  and  $\gamma_2 = 0.7$ . Tonooka (2005) found that the  $\gamma$  calculated by Equation (8) will not only reduce biases in the water vapor profile, but will also simultaneously reduce errors in the air temperature profiles and/or elevation. An example of the water vapor scaling factor,  $\gamma$ , is shown in Figure 5 for a MODIS observation on 29 August 2004.

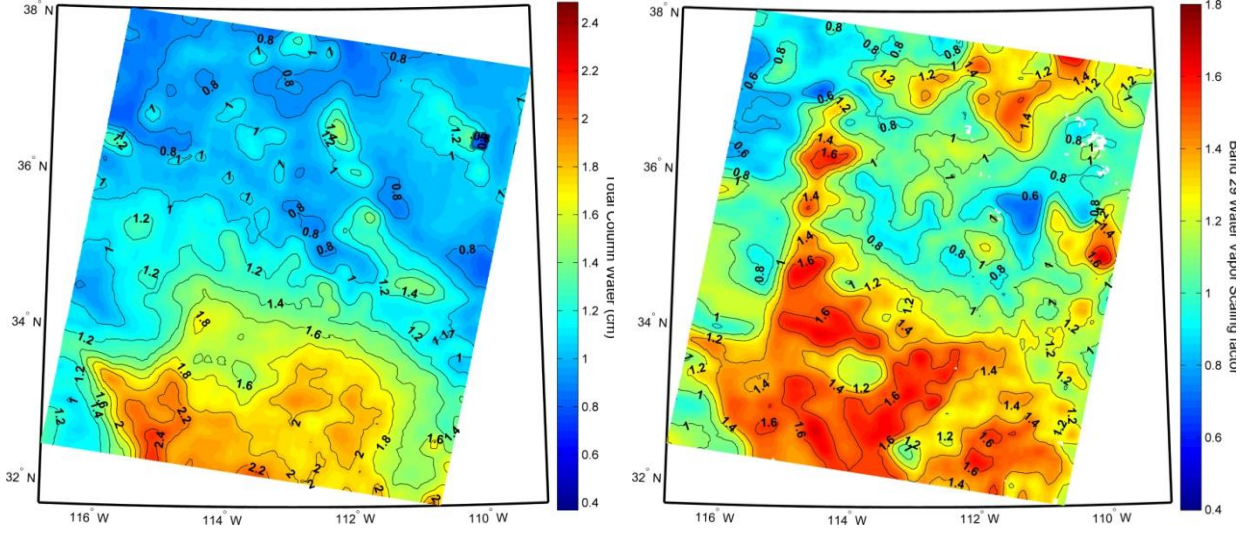


Figure 4. MODIS MOD07 total column water vapor (left) and WVS factor,  $\gamma$ , (right) computed using Equation (5 and 6) for a MODIS scene cutout on 29 August 2004.

## 6.1 Scaling Atmospheric Parameters

### 6.1.1 Transmittance and Path Radiance

Once the MODTRAN run has completed and the  $\gamma$  image has been interpolated and smoothed, the atmospheric parameters transmittance  $\tau_i$  and path radiance  $L_i^\uparrow$  are modified as follows:

$$\tau_i(\theta, \gamma) = \tau_i(\theta, \gamma_1) \frac{\gamma^{\beta_i} - \gamma_2^{\beta_i}}{\gamma_1^{\beta_i} - \gamma_2^{\beta_i}} \cdot \tau_i(\theta, \gamma_2) \frac{\gamma_1^{\beta_i} - \gamma^{\beta_i}}{\gamma_1^{\beta_i} - \gamma_2^{\beta_i}} \quad (9)$$

$$L_i^\uparrow(\theta, \gamma) = L_i^\uparrow(\theta, \gamma_1) \cdot \frac{1 - \tau_i(\theta, \gamma)}{1 - \tau_i(\theta, \gamma_1)} \quad (10)$$

Once the transmittance and path radiance have been adjusted using the scaling factor, the surface radiance can be computed using Equation (4).

### 6.1.2 Downward Sky Irradiance

In the WVS simulation model, the downward sky irradiance can be modeled using the path radiance, transmittance, and view angle as parameters. To simulate the downward sky irradiance in a MODTRAN run, the sensor target is placed a few meters above the surface, with surface emission set to zero and view angle set at prescribed values, e.g., Gaussian angles ( $\theta = 0^\circ, 11.6^\circ, 26.1^\circ, 40.3^\circ, 53.7^\circ, \text{ and } 65^\circ$ ). In this way, the only radiance contribution is from the reflected

downwelling sky irradiance at a given view angle. The total sky irradiance contribution is then calculated by summing up the contribution of all view angles over the entire hemisphere:

$$L_i^\downarrow = \int_0^{2\pi} \int_0^{\pi/2} L_i^\downarrow(\theta) \cdot \sin\theta \cdot \cos\theta \cdot d\theta \cdot d\delta \quad (11)$$

where  $\theta$  is the view angle and  $\delta$  is the azimuth angle. However, to minimize computational time in the MODTRAN runs, the downward sky irradiance can be modeled as a non-linear function of path radiance at nadir view:

$$L_i^\downarrow(\gamma) = a_i + b_i \cdot L_i^\uparrow(0, \gamma) + c_i L_i^\uparrow(0, \gamma)^2 \quad (12)$$

where  $a_i$ ,  $b_i$ , and  $c_i$  are regression coefficients (Table 6), and  $L_i^\uparrow(0, \gamma)$  is computed by:

$$L_i^\uparrow(0, \gamma) = L_i^\uparrow(\theta, \gamma) \cdot \frac{1 - \tau_i(\theta, \gamma)^{\cos\theta}}{1 - \tau_i(\theta, \gamma)} \quad (13)$$

Tonooka (2005) found RMSEs of less than 0.07 W/m<sup>2</sup>/sr/μm for ASTER bands 10–14 when using Equation (13) as opposed to Equation (12). Figure 6 shows an example of comparisons between MODIS band 29 (8.55 μm) atmospheric transmittance (top), path radiance (middle), and computed surface radiance (bottom), before and after applying the WVS scaling factor,  $\gamma$ , for the MODIS cutout shown in Figure 5. A decrease in transmittance and corresponding increase in path radiance values, after scaling over an area in the south of the image, show that the original atmospheric water absorption was underestimated using input MODIS MOD07 atmospheric profiles. The result is an increase in surface radiance over the bare regions of the Mojave Desert in the south of the image due to an increase in reflected downward sky irradiance.

### 6.1.3 Band model parameters

The band model parameter,  $\beta_i$ , in equation 8 is computed using MODTRAN simulations where the total water vapor for each profiles is scaled by three different  $\gamma$  values ( $\gamma_1=0.8$ ,  $\gamma_2=1.0$ ,  $\gamma_3=1.2$ ). For each band, the procedure is as follows:

Given:

$\beta_i$ : band model parameter value for a given band,  $i$ , in Table 5.

$\gamma_1=0.8$ ,  $\gamma_2=1.0$ ,  $\gamma_3=1.2$ , and trnX: transmittance for scaled profile,  $j$ , with  $\gamma_X$

$$p1 = \frac{(\gamma_3^{\beta_i} - \gamma_2^{\beta_i})}{(\gamma_1^{\beta_i} - \gamma_2^{\beta_i})} \quad (14)$$

$$p2 = \frac{(\gamma_1^{\beta_i} - \gamma_3^{\beta_i})}{(\gamma_1^{\beta_i} - \gamma_2^{\beta_i})} \quad (15)$$

Then for each profile,  $j$ ,  $trn3' = trn1^{p1} \times trn2^{p2}$

The optimal value of  $\beta_i$  for all the simulations is then obtained by least squares optimization, i.e.

$$\min_{\beta_i} \sum_j (trn3' - trn3)^2 \quad (16)$$

**Table 5. MODIS-Terra band model parameters in Equation (8).**

Band	Parameter
29	$\beta_1 = 1.4293$
31	$\beta_2 = 1.8203$
32	$\beta_3 = 1.8344$

**Table 6. MODIS-Terra regression coefficients for Equation (12).**

Band	a	b	c
29	-0.0011	1.7807	-0.0333
31	-0.0019	1.7106	-0.0545
32	0.0012	1.7005	-0.0595

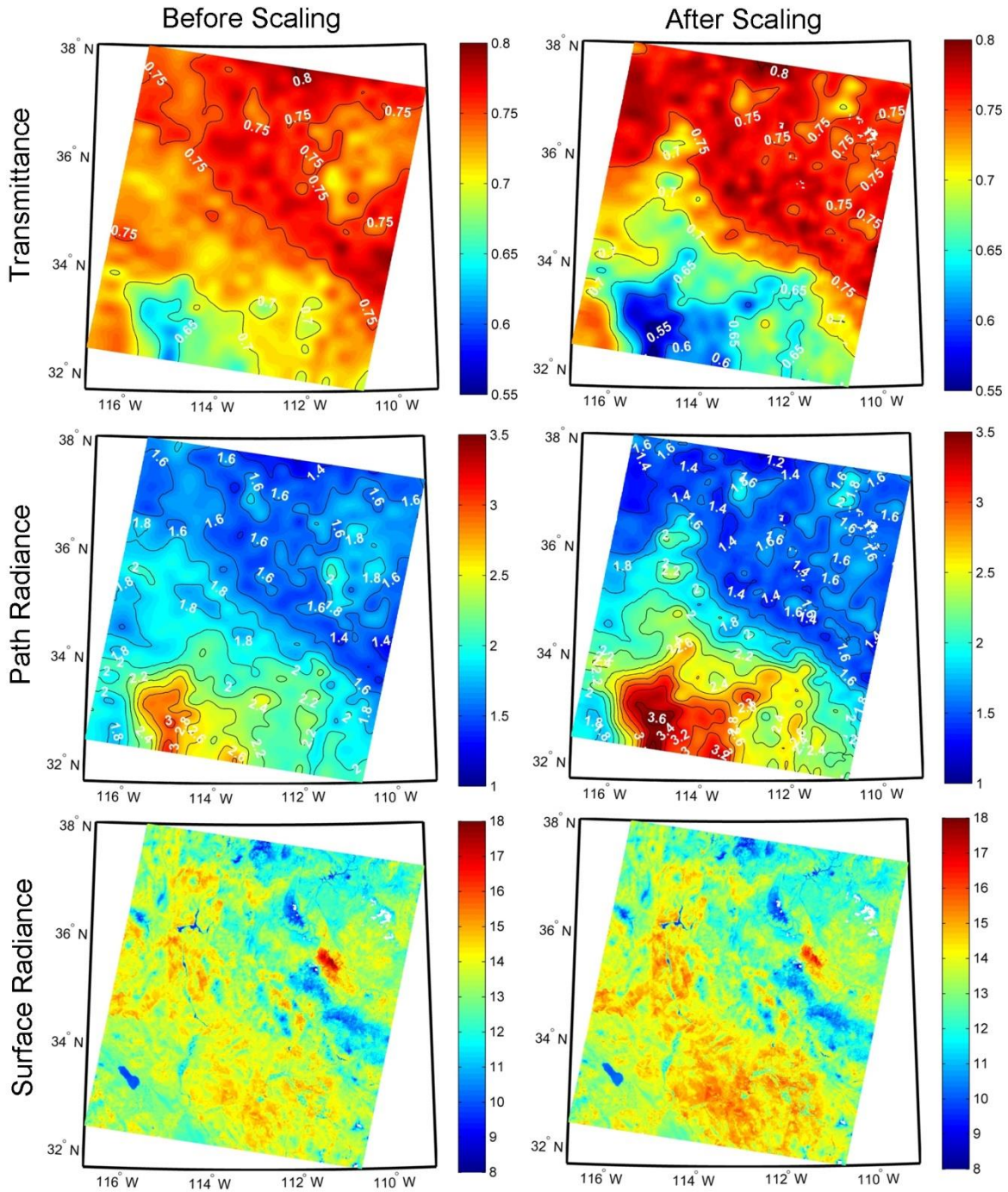


Figure 5. Comparisons between the atmospheric transmittance (top), path radiance ( $W/m^2/\mu m^{-1}$ ) (middle), and computed surface radiance ( $W/m^2/\mu m^{-1}$ ) (bottom), before and after applying the WVS scaling factor  $\gamma$  to a MODIS scene cutout shown in Figure 5. Results are shown for MODIS band 29 ( $8.55 \mu m$ ).

## 6.2 EMC/WVD Coefficients Calculation

The EMC/WVD coefficients ( $p, q, r$ ) in Equation (7) can be determined using a global simulation model with input atmospheric data from either radiosonde or numerical weather model sources. For this study we used the SeeBor V5.0 radiosounding database provided by the University of Wisconsin-Madison (Hook et al. 2013). The SeeBor data consist of 15,704 global profiles of uniformly distributed global atmospheric soundings temperature, moisture, and ozone at 101 pressure levels for clear sky conditions, acquired both day and night in order to capture the full-scale natural atmospheric variability. These profiles are taken from NOAA-88, an ECMWF 60L training set; TIGR-3; ozonesondes from eight NOAA Climate Monitoring and Diagnostics Laboratory (CMDL) sites; and radiosondes from 2004 in the Sahara Desert. The SeeBor data are curated with the following quality criteria: For clear sky conditions, the relative humidity (RH) value of the profiles must be less than 99% at each level below the 250 hPa pressure level. It is also required that the original top of sounding pressure be no greater than 30 hPa for temperature and moisture profiles and 10 hPa for ozone. Additionally, for each profile in the dataset, a physically based characterization of the surface skin temperature and surface emissivity must be assigned. As the radiosondes may drift towards water bodies, we further filtered the data to contain at least 50% of the records over land. This reduced the sample size to 9136 data points. When classified based upon the local sunrise and sunset times, the day and night profiles are nearly equally distributed with counts of 4990 and 4142, respectively. Figure 7 shows the distribution of the surface temperature with the total precipitable water in centimeters for the profiles used in the simulation. In addition to the quadratic nonlinear relationship, the profiles also capture high temperature/low water vapor conditions common to most arid and semi-arid regions. Figure 8 shows the global distribution of the profiles, with markers distinguishing between day/night profiles using sunrise/sunset time at the time of the profile recordings.

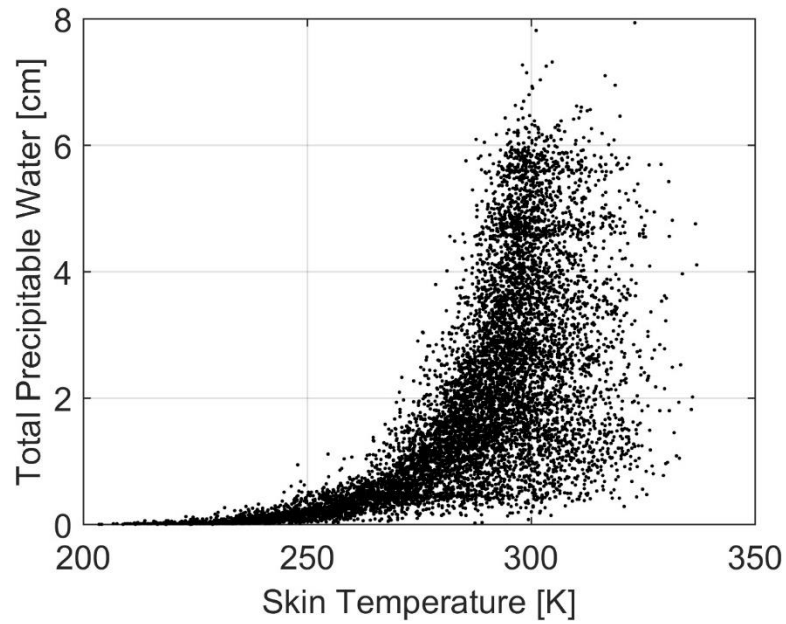


Figure 6. The total precipitable water versus skin temperature in the SeeBor profile used in the simulation for generating view angle and day–night-dependent coefficients.

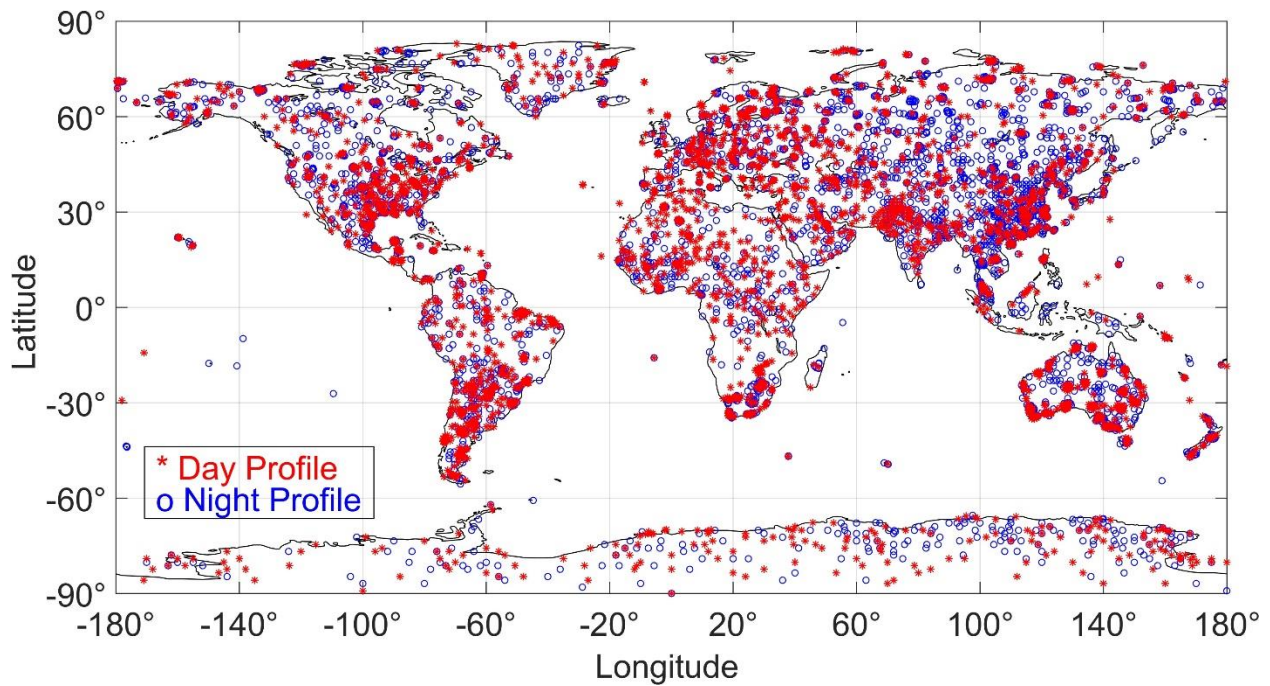


Figure 7. Global SeeBor radiosonde database showing the distribution of day (red stars) and night (open blue circles) profiles used in the generation of the WVS coefficients.

### 6.2.1 Simulations

In order to perform the simulations, we consider the emissivity spectra from the ASTER spectral library consisting of 102 samples that includes a variety of materials such as water, snow/ice, vegetation, rocks, soils, and sands. The emissivity of the samples cover a broad range of emissivities with even distribution ranging from ~0.6 to 1. The selected spectra are convolved to the MODIS spectral response functions for band 29, 31, 32 in order to perform the simulation. A total of 931,872 simulations (9136 profiles x 102 samples) are simulated with the RTTOV radiative transfer model for the set of 11 Gaussian view angles (between 0-70°), and for the three MODIS TIR bands. Using the simulated at-sensor  $T_k$ , and at-surface  $T_g$  calculated brightness temperatures, and an estimate of the total precipitable water vapor, the best fit coefficients in Equation (7) are found by using a linear least squares method, and dependent on four independent variables: day/night case, view angle, minimum band emissivity in intervals of 0.05 from 0.6 - 1, and precipitable water vapor. As shown in Figure 9, the RMSE between calculated and modeled surface brightness temperature for MODIS Aqua band 29 for all view angles is less than 1 K below 60-degree view angle. The exponential increase in RMSE with higher view angle can be attributed to the nonlinear effects of the Planck function due to increase in path length through the atmosphere in comparison to the nadir view. The obtained day and night coefficients are applied based on whether more than two-thirds of the land pixels are illuminated by the sun as determined by the solar zenith angles greater than 85 degrees and vice versa.

Finally, a four-dimensional look-up table (LUT) is produced consisting of the regression coefficients for the three TIR bands and the four independent variables. The EMC/WVD LUT is then used on a pixel-by-pixel basis for calculating the  $T_g$  (and  $\gamma$ ), given estimates of the view angle, emissivity, and PWV. Emissivity information from the ASTER Global Emissivity Database (v3) (Hulley et al. 2015a) are used to compute the minimum band emissivity at each MODIS pixel. This procedure is explained in detail in the following section. Note that the EMC/WVD coefficients are mapped to all MODIS pixels in a granule through bi-cubic interpolation of the coefficients derived from the four factors: day/night case, view angle, minimum band emissivity, and precipitable water vapor. Bi-cubic interpolation assures smooth transitions in the EMC/WVD coefficients across the pixels.

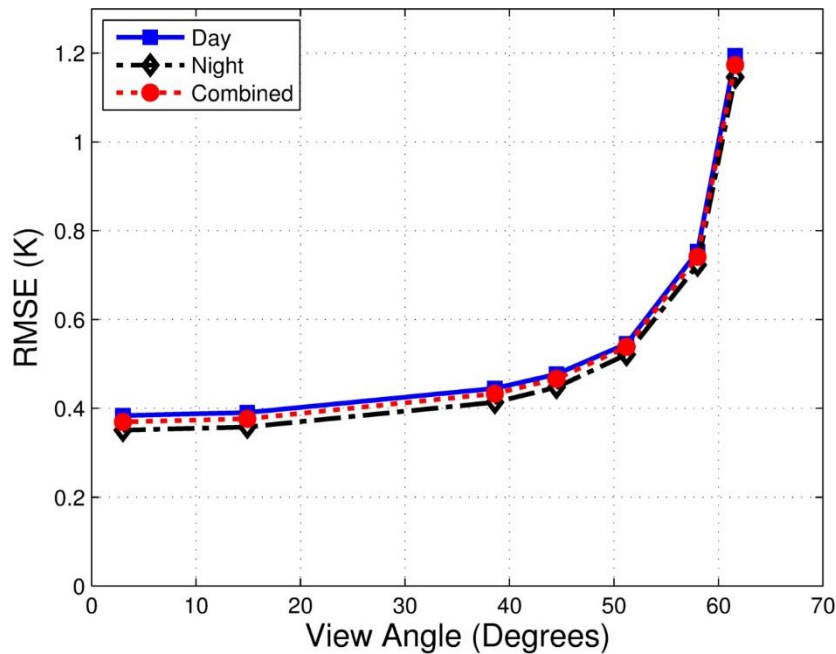


Figure 8. The RMSE between calculated and modeled surface brightness temperature for MODIS Aqua band 29 are plotted for corresponding view angles considered in the simulation using global radiosonde profile data as discussed in the text. The RMSE is less than 1 K for view angles less than 60°.

### 6.2.2 ASTER Global Emissivity Dataset (GED) v3

The ASTER GED v3 is a global emissivity dataset developed using millions of cloud free ASTER retrieved emissivity data over a 9-year period (2000-2008), and aggregated and mosaicked to produce a gridded global map. Recently, version 3 of the dataset has been made available that provides an average surface emissivity at the five ASTER TIR wavelengths (8.3, 8.6, 9.1, 10.6, and 11.3  $\mu\text{m}$ ) and for two different resolutions - 3 arc sec ( $\sim 100$  m) and 30 arc sec ( $\sim 1$  km). ASTER GEDv3 has been extensively validated in the past over mostly arid and semi-arid regions (Hulley and Hook 2009c; Hulley et al. 2015b) with an average absolute band error of  $\sim 1\%$  (Hulley et al. 2015b).

In order to assign the correct WVS coefficients discussed in the previous section, the ASTER GED data have to be first spectrally adjusted to the three MODIS bands 29, 31 and 32. To do this we use a regression approach based on a set of laboratory spectra from the ASTER spectral library,

where the ASTER bands chosen in the regression fall closest to the MODIS spectral response shapes. The spectral adjust functions are described as follows:

$$\epsilon(MODIS)_{29} = 0.9878 \epsilon(ASTER)_{11} \quad (17)$$

$$\epsilon(MODIS)_{31} = 0.4050 \epsilon(ASTER)_{13} + 0.5945 \epsilon(ASTER)_{14} + 0.0013 \quad (18)$$

$$\epsilon(MODIS)_{32} = 0.1175 \epsilon(ASTER)_{13} + 0.3572 \epsilon(ASTER)_{14} + 0.5168 \quad (19)$$

where,  $\epsilon(MODIS)_{29}$ ,  $\epsilon(MODIS)_{31}$ , and  $\epsilon(MODIS)_{32}$  are the spectrally adjusted ASTER GED emissivity for the MODIS TIR bands 29, 31 and 32, and  $\epsilon(ASTER)_{11}$ ,  $\epsilon(ASTER)_{13}$ , and  $\epsilon(ASTER)_{14}$  are the ASTER GED emissivity values for bands 11, 13 and 14, respectively. The regression coefficients are calculated using a wide range of emissivities including rocks, soils, vegetation, water and ice emissivity spectra from several spectral libraries and lab measurements, including the ASTER spectral library (Baldrige et al. 2009b) and emissivity measurements from sand dunes sites (Hulley et al. 2009a).

Because the ASTER GEDv3 is a static product, in addition to spectral adjustment, an emissivity adjustment is required to account for changes in vegetation phenology and seasonal changes in snow cover. This adjustment is done by employing a theoretical relationship between emissivity and normalized difference vegetation index (NDVI), as initially proposed by (Valor and Caselles 1996). The snow cover fraction adjustment is performed based on the same methodology. The specific steps of the adjustment process using MODIS data are detailed in Hulley et al. (2015b). For MODIS, data from the global monthly MODIS snow cover 0.05° product (MOD10CM), and the MODIS monthly gridded NDVI product (MOD13C2) were used to estimate the fractional vegetation and snow cover fractions. These emissivity adjustments are usually relatively small (on order of 0.5%-1%) for seasonal changes, but can be large for high frequency land disturbances (fires, deforestation, tornadoes etc.). Figure 10 shows an example of Spectrally adjusted ASTER GED emissivity for MODIS band 29. The ASTER GED emissivity (at native 100 m) has been geolocated onto the MODIS swath (1-km) and has been adjusted for vegetation phenology using the MODIS MOD13 NDVI product. This emissivity is consequently used to assign the correct WVS coefficient in the computation of surface brightness temperature in Equation (7).

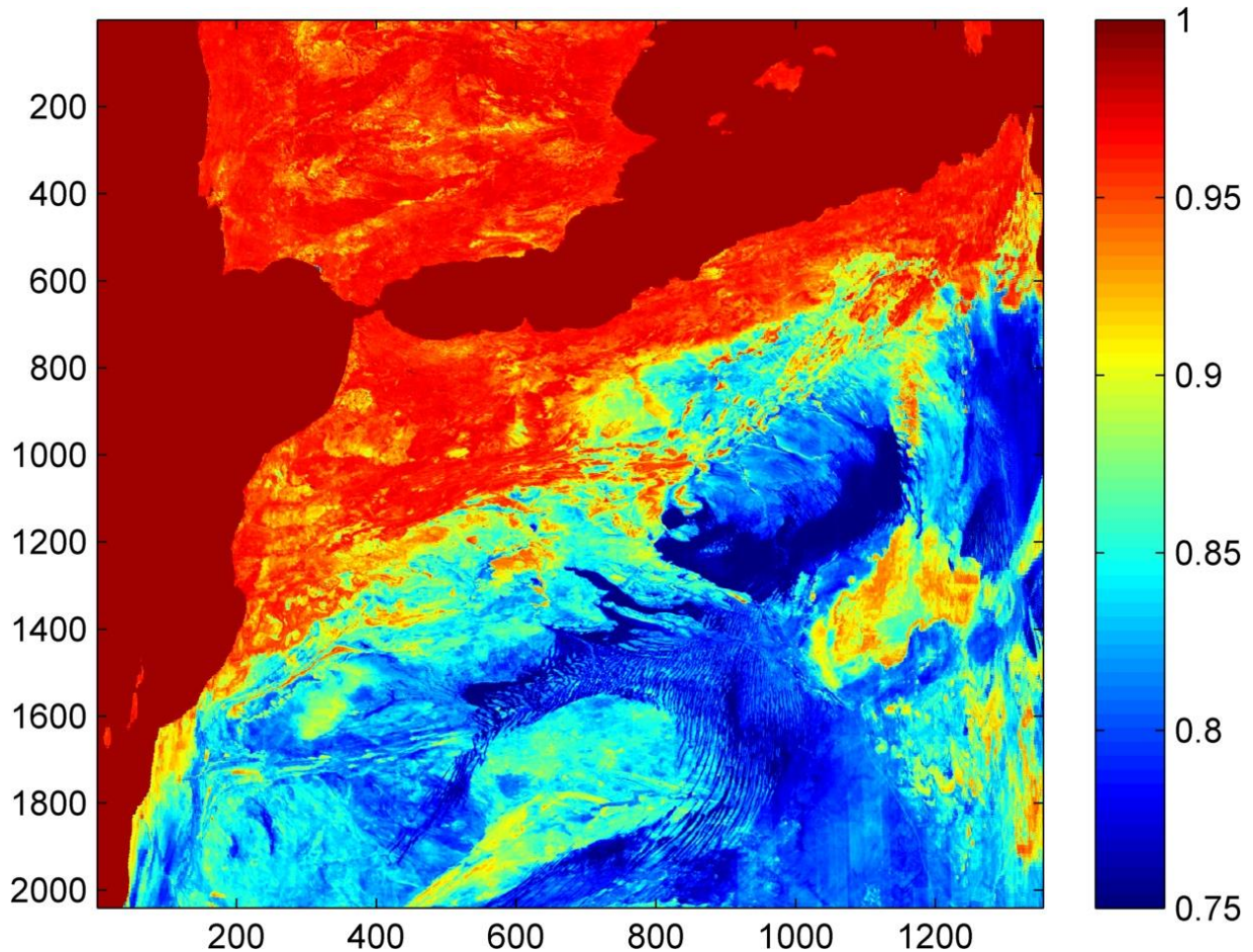


Figure 9. Spectrally adjusted ASTER GED emissivity for MODIS band 29 (see text for details). The ASTER GED emissivity (100 m) has been geolocated onto the MODIS swath (1-km) and has been adjusted for vegetation phenology using the MODIS MOD13 NDVI product.

## 7 Temperature and Emissivity Separation Approaches

The radiance in the TIR atmospheric window (8–13  $\mu\text{m}$ ) is dependent on the temperature and emissivity of the surface being observed according to Planck's law. Even if the atmospheric properties (water vapor and air temperature) are well known and can be removed from Equation (1), the problem of retrieving surface temperature and emissivity from multispectral measurements is still a non-deterministic process. This is because the total number of measurements available ( $N$  bands) is always less than the number of variables to be solved for (emissivity in  $N$  bands and one surface temperature). Therefore, no retrieval will ever do a perfect job of separation, with the consequence that errors in temperature and emissivity may co-vary. If the surface can be

approximated as Lambertian (isotropic) and the emissivity is assigned *a priori* from a land-cover classification, then the problem becomes deterministic with only the surface temperature being the unknown variable. Examples of such cases would be over ocean, ice, or densely vegetated scenes where the emissivity is known *a priori* and spectrally flat in all bands. Another deterministic approach is the single-band inversion approach. If the atmospheric parameters are known in Equation (1), then the temperature can also be solved for using a single band assuming the emissivity is known, usually in the clearest region of the window ( $\sim 11 \mu\text{m}$ ). Deterministic approaches are usually employed with sensors that have one or two bands in the TIR region using an SW approach, while non-deterministic approaches are applied to multispectral sensors with three or more bands in the TIR so that spectral variations in the retrieved emissivity can be related to surface composition and cover, in addition to retrieving the surface temperature. For the MODIS MOD21 product, a non-deterministic approach will be used in order to retrieve spectral emissivity in bands 29, 31, and 32, in addition to the surface temperature.

## **7.1 Deterministic Approaches**

### **7.1.1 SW Algorithms**

The most common deterministic approach can be employed without having to explicitly solve the radiative transfer equation. Two or more bands are employed in the window region (typically  $10.5\text{--}12 \mu\text{m}$ ), and atmospheric effects are compensated for by the differential absorption characteristics from the two bands. This approach is used with much success over oceans to compute the SST (Brown and Minnett 1999), as the emissivity of water is well known (Masuda et al. 1988). Variations of this method over land include the SW approach (Coll and Caselles 1997; Prata 1994; Price 1984; Wan and Dozier 1996; Yu et al. 2008), the multichannel algorithm (Deschamps and Phulpin 1980), and the dual-angle algorithm (Barton et al. 1989). Over land, the assumption is that emissivities in the SW bands being used are stable and well known and can be assigned using a land-cover classification map (Snyder et al. 1998). However, this assumption introduces large errors over barren surfaces where much larger variations in emissivity are found due to the presence of large amounts of exposed rock or soil, often with abundant silicates (Hulley and Hook 2009a). Land cover classification maps typically use Visible Near-Infrared (VNIR) data for assignment of various classes. This method may work for most vegetation types and over water surfaces but, because VNIR reflectances correspond predominately to Fe oxides and  $\text{OH}^-$  and not

to the Si-O bond over barren areas, there is little or no correlation with silicate mineralogy features in thermal infrared data. This is why, in most classification maps, only one bare land class is specified (barren).

The primary LST product for MODIS (MOD11) currently uses a generalized SW approach (Wan and Dozier 1996), where coefficients are stratified according to view angle, total column water (TCW), and surface air temperature. Emissivities are assigned *a priori* based on land cover classification maps. The MOD21 LST&E product will not be based on an SW algorithm as in MOD11, but will use a non-deterministic multi-spectral approach for the following reasons:

1. An SW method based on classification is not able to retrieve spectral emissivities of geologic surfaces for compositional analysis.
2. The emissivity of the land surface is in general heterogeneous and is dependent on many factors including surface soil moisture, vegetation cover changes, and surface compositional changes, which are not characterized by land classification maps.
3. SW algorithms are inherently very sensitive to measurement noise between bands.
4. Classification leads to sharp discontinuities and contours in the data between different class types, while a physical-based multispectral retrieval will produce seamless emissivity images.
5. Temperature inaccuracies are difficult to quantify over geologic surfaces where constant emissivities are assigned.

### 7.1.2 *Single-Band Inversion*

If the atmosphere is known, along with an estimate of the emissivity, then Equation (1) can be inverted to retrieve the surface temperature using one band. Theoretically, any band used should retrieve the same temperature, but uncertainties in the atmospheric correction will result in subtle differences as different bands have stronger atmospheric absorption features than others that may be imperfectly corrected for atmospheric absorption. For example, a band near 8  $\mu\text{m}$  will have larger dependence on water vapor, while the 9–10- $\mu\text{m}$  region will be more susceptible to ozone absorption. Jimenez-Munoz and Sobrino (2010) applied this method to ASTER data by using atmospheric functions (AFs) to account for atmospheric effects. The AFs can be computed by the radiative transfer equation or empirically given the total water vapor content. The clearest ASTER band (13 or 14) was used to retrieve the temperature, with the emissivity determined using an

NDVI fractional vegetation cover approach. A similar procedure has been proposed to retrieve temperatures from the Landsat TIR band 6 on ETM+ and TM sensors (Li et al. 2004). The single-band inversion method has not been proposed for MODIS data for the following reasons:

1. Inability to retrieve spectral emissivity of geologic surfaces for compositional analysis. This will not be possible with the single-band approach, which assigns emissivity based on land cover type and vegetation fraction.
2. Estimating emissivity from an NDVI-derived vegetation cover fraction over arid and semi-arid regions will introduce errors in the LST because NDVI is responsive only to chlorophyll-active vegetation, and does not correlate well with senescent vegetation (e.g., shrublands).
3. Only one-band emissivity is solved for the single-band inversion approach. The MODIS MOD21 product will be based on a multispectral retrieval approach.

### *7.1.3 Non-deterministic Approaches*

In non-deterministic approaches, the temperature and spectral emissivity are solved using an additional constraint or extra degree of freedom that is independent of the data source. These types of solutions are also rarely perfect because the additional constraint will always introduce an additional level of uncertainty; however, they work well over all surfaces (including arid and semi-arid) and can automatically account for land surface changes, such as those due to wildfires or surface soil moisture. First, we introduce two well-known approaches, the day/night and TISI algorithms, followed by an examination of the algorithms and methods that led up to establishment of the TES algorithm, which will be used in the MOD21 LST&E product.

#### *7.1.3.1 Day/Night Algorithm*

The constraint in the day/night algorithm capitalizes on the fact that the emissivity is an intrinsic property of the surface and should not change from day- to nighttime observations. The day/night algorithm is currently used to retrieve temperature/emissivity from MODIS data in the MOD11B1 product (Wan and Li 1997). The method relies on two measurements (day and night), and the theory is as follows: Two observations in  $N$  bands produce  $2N$  observations, with the unknown variables being  $N$ -band emissivities, a day- and nighttime surface temperature, four atmospheric variables (day and night air temperature and water vapor), and an anisotropic factor, giving  $N + 7$  variables. In order to make the problem deterministic, the following conditions must

be met:  $2N \geq N+7$ , or  $N \geq 7$ . For the MODIS algorithm, this can be satisfied by using bands 20, 22, 23, 29, and 31–33. Although this method is theoretically sound, the retrieval is complicated by the fact that two clear, independent observations are needed (preferably close in time) and the pixels from day and night should be perfectly co-registered. Errors may be introduced when the emissivity changes from day to night observation (e.g., due to condensation or dew), and from undetected nighttime cloud. In addition, the method relies on very precise co-registration between the day- and nighttime pixel.

### 7.1.3.2 Temperature Emissivity Separation Approaches

During research activities leading up to the ASTER mission, the ASTER TEWG was established in order to examine the performance of existing non-deterministic algorithms and select one that would be suitable for retrieving the most accurate temperature and/or emissivity over the entire range of terrestrial surfaces. This led to the development of the TES algorithm, which ended up being a hybrid algorithm that capitalized on the strengths of previous algorithms. In Gillespie et al. (1999), ten inversion algorithms were outlined and tested, leading up to development of TES. For all ten algorithms, an independent atmospheric correction was necessary. The ten algorithms were as follows: 1) Alpha-derived emissivity (ADE) method, 2) Classification method, 3) Day-Night measurement, 4) Emissivity bounds method, 5) Graybody emissivity method, 6) Mean Min-Max Difference (MMD) method, 7) Model emissivity method, 8) Normalized emissivity method (NEM), 9) Ratio Algorithm, and 10) SW algorithm.

In this document, we will briefly discuss a few of the algorithms but will not expand upon any of them in great detail. The Day-Night measurement (3), Classification (2), and SW (10) algorithms have already been discussed in section 4.2.1. A detailed description of all ten algorithms is available in Gillespie et al. (1999). The various constraints proposed in these algorithms can: determine spectral shape but not temperature, use multiple observations (day and night), assume a value for emissivity and calculate temperature, assume a spectral shape, or assume a relationship between spectral shape and minimum emissivity.

The NEM removes the downwelling sky irradiance component by assuming an  $\epsilon_{max}$  of 0.99. Temperature is then estimated by inverting the Planck function and a new emissivity found. This process is repeated until successive changes in the estimated surface radiances are small. This method in itself was not found to be suitable for ASTER because temperature inaccuracies tended to be high ( $>3$  K) and the emissivities had incorrect spectral shapes. Other approaches have used

a model to estimate emissivity at one wavelength (Lyon 1965) or required that the emissivity be the same at two wavelengths (Barducci and Pippi 1996). This introduces problems for multispectral data with more than five bands, e.g., ASTER.

The ADE method (Hook et al. 1992; Kealy et al. 1990; Kealy and Hook 1993) is based on the alpha residual method that preserves emissivity spectral shape but not amplitude or temperature. The introduced constraint uses an empirical relationship between spectral contrast and average emissivity to restore the amplitude of the alpha-residual spectrum and to compute temperature. The average emissivity was used in the relationship to minimize band-to-band calibration errors. The TEWG used this key feature of the ADE method in TES, although the minimum emissivity, rather than the average emissivity, was used in the empirical relationship (Matsunaga 1994). The ADE itself was not fully employed for two primary reasons as discussed in Gillespie et al. (1999): 1) ADE uses Wien's approximation,  $\exp(x) - 1 = \exp(x)$ , which introduces a noticeable "tilt" in the residual spectra that gets transferred to the final emissivity spectra; and 2) This issue was easily fixed in the hybrid version of TES.

Lastly, the temperature-independent spectral indices (TISI) approach (Becker and Li 1990) computes relative emissivities from power-scaled brightness temperatures. TISI, however, is band-dependent and only recovers spectral shape; furthermore, the values are non-unique. To retrieve actual emissivities, additional information or assumptions are needed. Other algorithms, which only retrieve spectral shape, are the thermal log and alpha residual approach (Hook et al. 1992) and spectral emissivity ratios (Watson 1992; Watson et al. 1990). Neither of these was considered because they do not recover temperature or actual emissivity values.

## **7.2 TES Algorithm**

The final TES algorithm proposed by the ASTER TEWG combined some core features from previous algorithms and, at the same time, improved on them. TES combines the NEM, the ratio, and the MMD algorithm to retrieve temperature and a full emissivity spectrum. The NEM algorithm is used to estimate temperature and iteratively remove the sky irradiance, from which an emissivity spectrum is calculated, and then ratioed to their mean value in the ratio algorithm. At this point, only the shape of the emissivity spectrum is preserved, but not the amplitude. In order to compute an accurate temperature, the correct amplitude is then found by relating the minimum emissivity to the spectral contrast (MMD). Once the correct emissivities are found, a

final temperature can be calculated with the maximum emissivity value. Additional improvements involve a refinement of  $\epsilon_{max}$  in the NEM module and refining the correction for sky irradiance using the  $\epsilon_{min}$ -MMD final emissivity and temperature values. Finally, a quality assurance (QA) data image is produced that partly depends on outputs from TES such as convergence, final  $\epsilon_{max}$ , atmospheric humidity, and proximity to clouds. More detailed discussion of QA is included later in this document.

Numerical modeling studies performed by the ASTER TEWG showed that TES can recover temperatures to within 1.5 K and emissivities to within 0.015 over most scenes, assuming well-calibrated, accurate radiometric measurements (Gillespie et al. 1998).

### 7.2.1 TES Data Inputs

Inputs to the TES algorithm are the surface radiance,  $L_{s,i}$ , given by Equation (4) (at-sensor radiance corrected for transmittance and path radiance), and downwelling sky irradiance term,  $L_{\lambda}^{\downarrow}$ , which is computed from the atmospheric correction algorithm using a radiative transfer model such as MODTRAN. Both the surface radiance and sky irradiance will be output as a separate product. The surface radiance is primarily used as a diagnostic tool for monitoring changes in Earth's surface composition. Before the surface radiance is estimated using Equation (4), the accuracy of the atmospheric parameters,  $L_{\lambda}^{\downarrow}$ ,  $\tau_{\lambda}(\theta)$ ,  $L_{\lambda}^{\uparrow}(\theta)$ , is improved upon using a WVS method (Tonooka 2005) on a band-by-band basis for each observation using an extended multi-channel/water vapor dependent (EMC/WVD) algorithm.

### 7.2.2 TES Limitations

As with any retrieval algorithm, limitations exist that depend on measurement accuracy, model errors, and incomplete characterization of atmospheric effects. Currently, the largest source of uncertainty for ASTER data is the residual effect of incomplete atmospheric correction. Measurement accuracy and precision contribute to a lesser degree. This problem is compounded for graybodies, which have low spectral contrast and are therefore more prone to errors in "apparent" MMD, which is overestimated due to residual sensor noise and incomplete atmospheric correction. A threshold classifier was introduced by the TEWG to partly solve this problem over graybody surfaces. Instead of using the calibration curve to estimate  $\epsilon_{min}$  from MMD, a value of  $\epsilon_{min} = 0.983$  was automatically assigned when the spectral contrast or MMD in emissivity was

smaller than 0.03 for graybody surfaces (e.g., water, vegetation). However, this caused artificial step discontinuities in emissivity between vegetated and arid areas.

At the request of users, two parameter changes were made to the ASTER TES algorithm on 1 August 2007, first described in Gustafson et al. (2006). Firstly, the threshold classifier was removed as it caused contours and artificial boundaries in the images, which users could not tolerate in their analyses. The consequence of removing the threshold classifier was a smoother appearance for all images but at the cost of TES underestimating the emissivity of graybody scenes, such as water by up to 3% and vegetation by up to 2% (Hulley et al. 2008). The second parameter change removed the iterative correction for reflected downwelling radiation, which also frequently failed due to inaccurate atmospheric corrections (Gustafson et al. 2006). Using only the first iteration resulted in improved spectral shape and performance of TES.

Figure 11 shows the distribution of LST uncertainties for the MODIS and ASTER TES algorithm with respect to TCW and simulated LST for TES+atm (atmospheric uncertainty) and TES+atm+wvs (atmospheric uncertainty with WVS) simulation cases. In general the TES+atm uncertainties increase with TCW and simulated LST for both types of surfaces and range from 4–6 K for TCW values greater than 4 cm and LSTs greater than 300 K. The TES+atm+wvs results show that applying the WVS method reduces the LST uncertainty at higher TCW contents by more than a factor of two, with uncertainties not exceeding 2 K for either type of surface type or sensor.

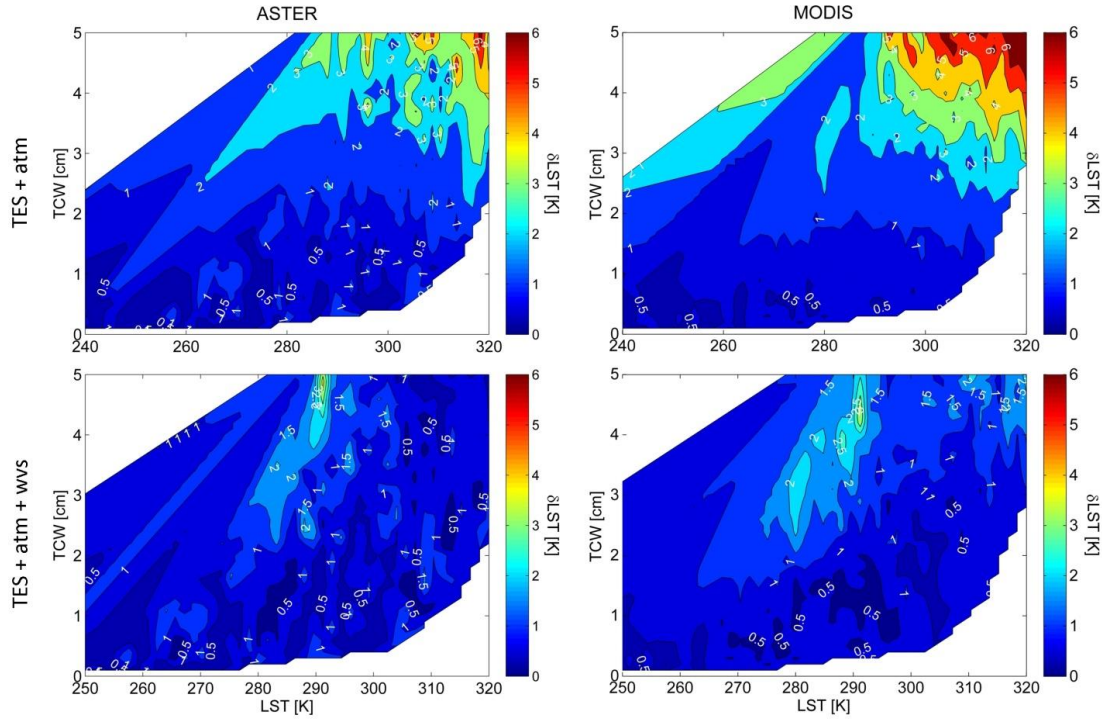


Figure 10. ASTER (left panels) and MODIS (right panels) LST uncertainty distributions plotted versus TCW and simulated LST for all end-member surface types (graybody, soils, sands, and rocks), for the TES algorithm including atmospheric error (TES+atm) and with the WVS method applied (TES+atm+wvs).

### 7.2.3 TES Processing Flow

Figure 12 shows the processing flow diagram for the generation of the cloud masks, land-leaving radiance, VNIR reflectances, and TES temperature and emissivity, while Figure 13 shows a more detailed processing flow of the TES algorithm itself. Each of the steps will be presented in sufficient detail in the following section, allowing users to regenerate the code. TES uses input image data of surface radiance,  $L_{s,i}$ , and sky irradiance,  $L_{\lambda}^{\downarrow}$ , to solve the TIR radiative transfer equation. The output images will consist of three emissivity images ( $\epsilon_i$ ) corresponding to MODIS bands 29, 31, 32, and one surface temperature image (T).

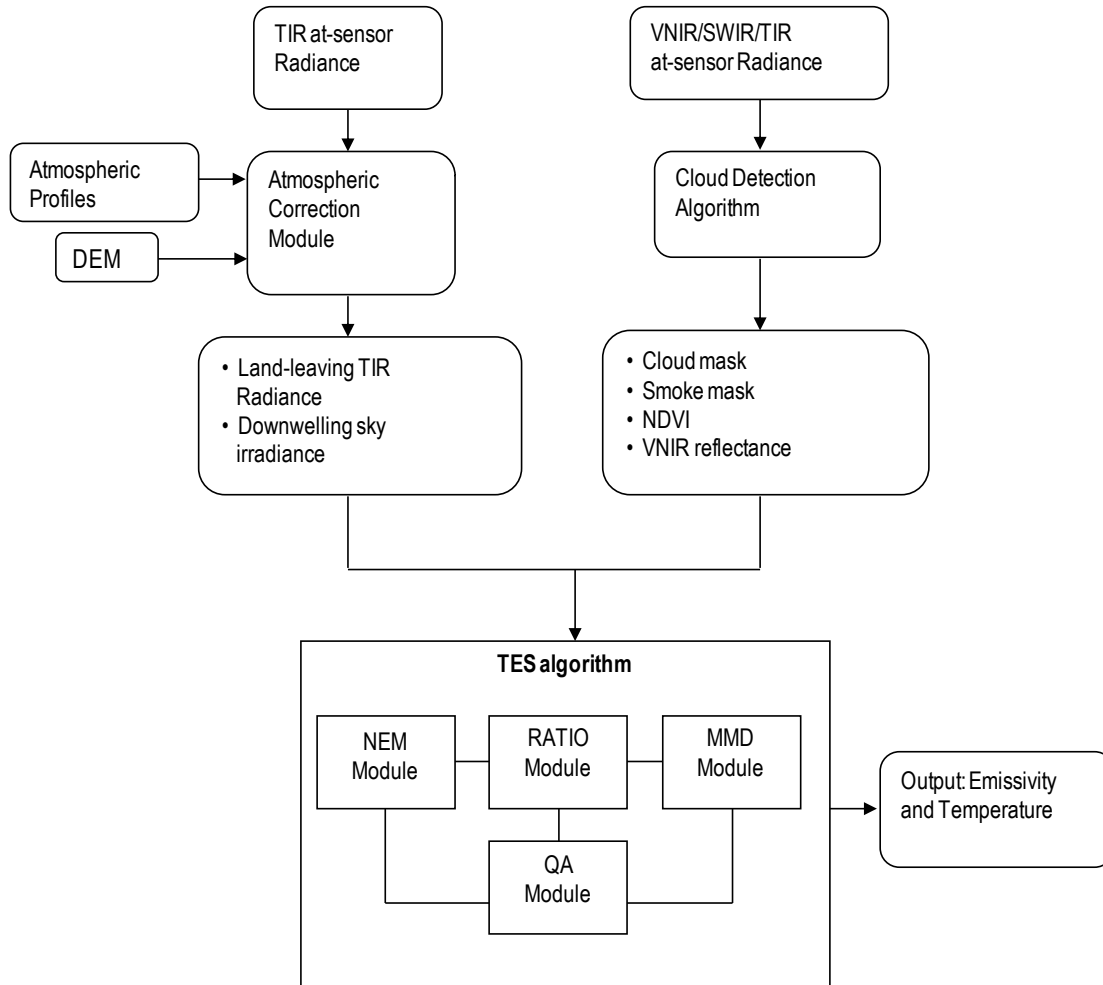


Figure 11. Flow diagram showing all steps in the retrieval process in generating the MODIS MOD21 LST&E product starting with TIR at-sensor radiances and progressing through atmospheric correction, cloud detection, and the TES algorithm.

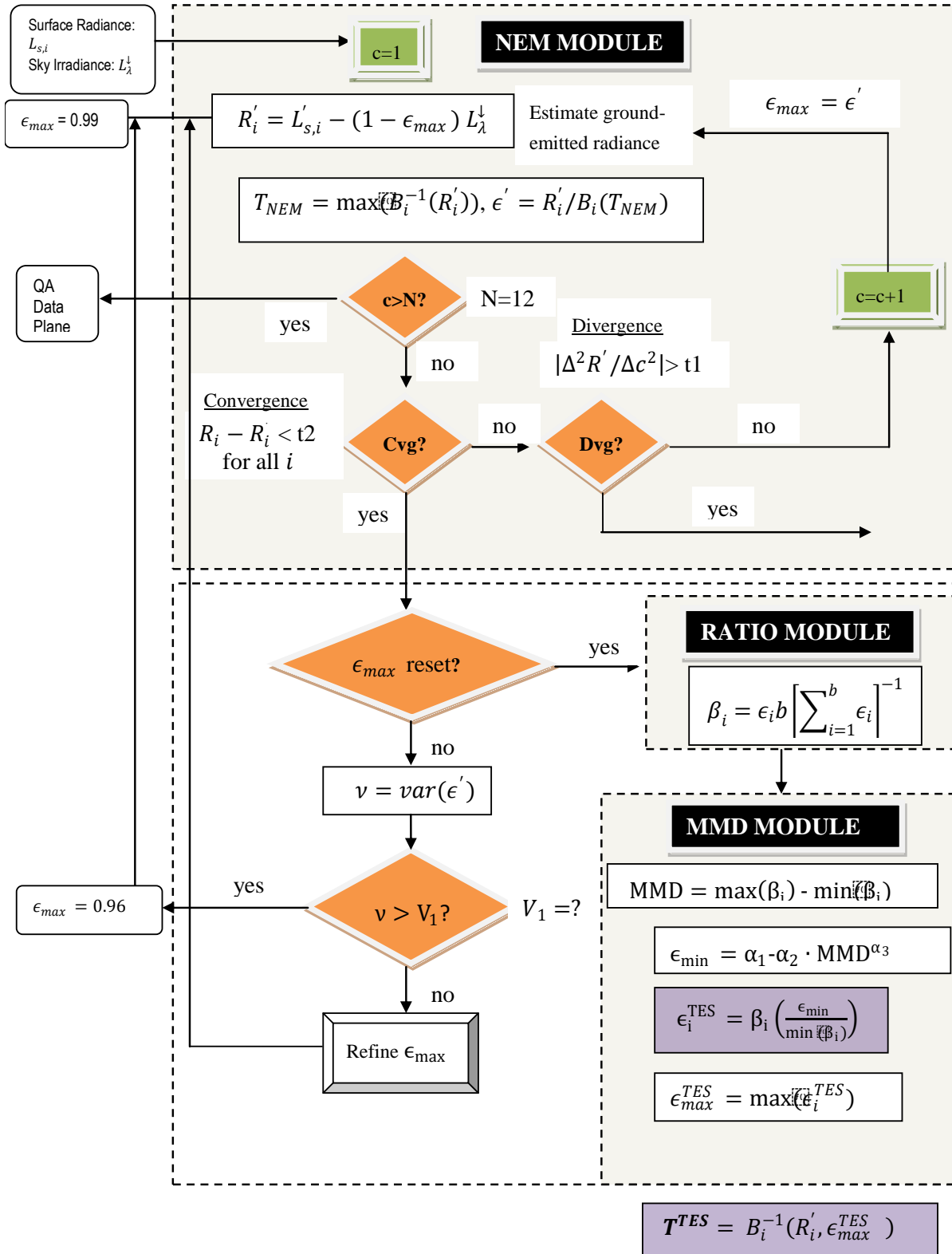


Figure 12. Flow diagram of the TES algorithm in its entirety, including the NEM, RATIO, and MMD modules. Details are included in the text, including information about the refinement of  $\epsilon_{max}$ .

#### 7.2.4 NEM Module

The NEM builds upon the model emissivity algorithm (Lyon 1965) by allowing the initial  $\epsilon_{max}$  value to be consistent for all wavelengths. The role of NEM is to compute the surface kinetic temperature,  $T$ , and a correct shape for the emissivity spectrum. An initial value of 0.99 is set for  $\epsilon_{max}$ , which is typical for most vegetated surfaces, snow, and water. For geologic materials such as rocks and sand,  $\epsilon_{max}$  values are set lower than this, typically 0.96, and this value remains fixed. For all other surface types, a modification to the original NEM allows for optimization of  $\epsilon_{max}$  using an empirically based process. For the majority of materials in the ASTER spectral library, a typical range for  $\epsilon_{max}$  is  $0.94 < \epsilon_{max} < 1.0$ . Therefore, for a material at 300 K, the maximum errors that NEM temperatures should have are  $\sim \pm 1.5$  K, assuming the reflected sky irradiance has been estimated correctly.

#### 7.2.5 Subtracting Downwelling Sky Irradiance

Generally the effects of sky irradiance are small with typical corrections of  $< 1$  K (Gillespie et al. 1998). However, the contribution becomes larger for pixels with low emissivity (high reflectance) or in humid conditions when the sky is warmer than the surface. Over graybody surfaces (water and vegetation), the effects are small because of their low reflectivity in all bands. The first step of the NEM module is to estimate ground-emitted radiance, which is found by subtracting the reflected sky irradiance from the surface radiance term:

$$R_i = L'_{s,i} - (1 - \epsilon_{max}) L_{\lambda}^{\downarrow} \quad (20)$$

The NEM temperature, which we call  $T_{NEM}$ , is then estimated by inverting the Planck function for each band using  $\epsilon_{max}$  and the ground-emitted radiance and then taking the maximum of those temperatures. The maximum temperature will most likely be closest to the actual surface temperature in the presence of uncompensated atmospheric effects.

$$T_i = \frac{c_2}{\lambda_i} \left( \ln \left( \frac{c_1 \epsilon_{max}}{\pi R_i \lambda_i^5} + 1 \right) \right)^{-1} \quad (21)$$

$$T_{NEM} = \max(T_i) \quad (22)$$

The NEM emissivity spectrum is then calculated as the ratio of emitted radiance to that of a blackbody with a temperature estimated by  $T_{NEM}$ :

$$\epsilon'_i = \frac{R_i}{B_i(T_{NEM})} \quad (23)$$

The new emissivity spectrum is then used to re-calculate  $R'_i = L'_{s,i} - (1 - \epsilon'_i) L_{\lambda}^{\downarrow}$ , and the process is repeated until convergence, which is determined if the change in  $R_i$  between steps is less than a set threshold,  $t_2$ , which is set as the radiance equivalent to NE $\Delta$ T of the sensor. The process is stopped if the number of iterations exceeds a limit  $N$ , set to 12. Execution of the NEM module is also aborted if the slope of  $R_i$  versus iteration,  $c$ , increases such that  $|\Delta^2 R' / \Delta c^2| > t_1$ , where  $t_1$  is also set to radiance equivalent of NE $\Delta$ T for the sensor (0.05 K for MODIS). In this case, correction is not possible, TES is aborted, and NEM values of  $\epsilon_i$  and  $T_{NEM}$  are reported in the QA data plane, along with an error flag. TES is also aborted and an error flag recorded if, for any iteration, the values of  $\epsilon_i$  fall out of reasonable limits, set to  $0.5 < \epsilon_i < 1.0$ . See Figure 13 for a detailed description of these steps.

### 7.2.6 Refinement of $\epsilon_{max}$

Most pixels at MODIS resolution (1 km) will contain a mixed cover type consisting of vegetation and soil, rock and water. The effective maximum emissivity for such pixels will therefore vary across the scene and depend on the fractional contribution of each cover type. For these cases, the initial  $\epsilon_{max} = 0.99$  may be set to high and refinement of  $\epsilon_{max}$  is necessary to improve accuracy of  $T_{NEM}$ . The optimal value for  $\epsilon_{max}$  minimizes the variance,  $\nu$ , of the NEM calculated emissivities,  $\epsilon_i$ . The optimization of  $\epsilon_{max}$  is only useful for pixels with low emissivity contrast (near graybody surfaces) and therefore is only executed if the variance for  $\epsilon_{max} = 0.99$  is less than an empirically determined threshold (e.g.,  $V_1 = 1.7 \times 10^{-4}$  for ASTER ) (Gillespie et al. 1998). If the variance is greater than  $V_1$ , then the pixel is assumed to predominately consist of either rock or soil. For this case,  $\epsilon_{max}$  is reset to 0.96, which is a good first guess for most rocks and soils in the ASTER spectral library, which typically fall between the 0.94 and 0.99 range. For MODIS the  $\epsilon_{max}$  values is set to 0.97, a typical value for bare surfaces in the 12  $\mu$ m range. If the first condition is met, and the pixel is a near-graybody, then values for  $\epsilon_{max}$  of 0.92, 0.95, 0.97, and 0.99 are used to compute the variance for each corresponding NEM emissivity spectrum. A plot of variance  $\nu$  versus each  $\epsilon_{max}$  value results in an upward-facing parabola with the optimal  $\epsilon_{max}$  value determined by the minimum of the parabola curve in the range  $0.9 < \epsilon_{max} < 1.0$ . This minimum is set to a new  $\epsilon_{max}$  value, and the NEM module is executed again to compute a new  $T_{NEM}$ . Further tests are used to see if a reliable solution can be found for the refined  $\epsilon_{max}$ . If the parabola is too flat, or too steep, then refinement is aborted and the original  $\epsilon_{max}$  value is used.

The steepness condition is met if the first derivative (slope of  $\nu$  vs.  $\epsilon_{max}$ ) is greater than a set threshold (e.g.,  $V_2 = 1.0 \times 10^{-3}$  for ASTER) and the flatness conditions is met if the second derivative is less than a set threshold (e.g.,  $V_3 = 1.0 \times 10^{-3}$  for ASTER). Finally, if the minimum  $\epsilon_{max}$  corresponds to a very low  $\nu$ , then the spectrum is essentially flat (graybody) and the original  $\epsilon_{max} = 0.99$  is used. This condition is met if  $\nu_{min} < V_4$  (e.g.,  $V_2 = 1.0 \times 10^{-4}$ ). Table 7 shows typical output from various stages of the TES algorithm for pixels representing three different surface types: sand dunes, vegetated cropland, and semi-vegetated cropland for a MODIS scene on 29 August 2004 over the Imperial Valley, southeastern California. Note the different  $\epsilon_{max}$  value for each of these surface types. The dune pixel was set to 0.97 because of high variance in the NEM spectrum; the Salton Sea and shrubland pixels were set to 0.983, due to a lower spectral contrast.

**Table 7. Output from various stages of the MODTES algorithm for three surface types: sand dunes, Salton Sea, and shrubland transition zone for a MODIS test scene over the Imperial Valley, southeastern California.**

	Algodones Dunes	Salton Sea	Shrubland (transition zone)
$\epsilon_{max}$	0.97	0.983	0.97
<b>MMD</b>	0.166	0.006	0.088
$\epsilon_{min}$	0.817	0.975	0.886
$T_{NEM}$	327.27 K	304.76 K	325.61 K
$T_{TES}$	326.51 K	304.95 K	325.75 K

### 7.2.7 Ratio Module

In the ratio module, the NEM emissivities are ratioed to their average value to calculate a  $\beta_i$  spectrum as follows:

$$\beta_i = \frac{\epsilon_i}{\bar{\epsilon}} \quad (24)$$

Typical ranges for the  $\beta_i$  emissivities are  $0.75 < \beta_i < 1.32$ , given that typical emissivities range from 0.7 to 1.0. Errors in the  $\beta_i$  spectrum due to incorrect NEM temperatures are systematic.

### 7.2.8 MMD Module

In the MMD module, the  $\beta_i$  emissivities are scaled to an actual emissivity spectrum using information from the spectral contrast or MMD of the  $\beta_i$  spectrum. The MMD can then be related to the minimum emissivity,  $\epsilon_{min}$ , in the spectrum using an empirical relationship determined from

lab measurements of a variety of different spectra, including rocks, soils, vegetation, water, and snow/ice. From  $\epsilon_{min}$ , the actual emissivity spectrum can be found by re-scaling the  $\beta_i$  spectrum. First, the MMD of the  $\beta_i$  spectrum is found by:

$$MMD = \max(\beta_i) - \min(\beta_i) \quad (25)$$

Then MMD can be related to  $\epsilon_{min}$  using a power-law relationship:

$$\epsilon_{min} = \alpha_1 - \alpha_2 MMD^{\alpha_3}, \quad (26)$$

where  $\alpha_j$  are coefficients that are obtained by regression using lab measurements. For the three MODIS TIR bands between 8 and 12  $\mu\text{m}$  (shown in Figure 2), the values for the coefficients were calculated as  $\alpha_1 = 0.985$ ,  $\alpha_2 = 0.7503$ , and  $\alpha_3 = 0.8321$ . The TES emissivities are then calculated by re-scaling the  $\beta_i$  emissivities:

$$\epsilon_i^{TES} = \beta_i \left( \frac{\epsilon_{min}}{\min(\beta_i)} \right) \quad (27)$$

An example MODTES emissivity output image for band 29 (8.55  $\mu\text{m}$ ) is shown in Figure 14 for an MODIS cutout on 29 August 2004 over the Imperial Valley, southeastern California. Bare areas, such as the Algodones Dunes running diagonally across the southwest corner, generally have emissivity  $<0.85$ , while graybody surfaces such as the Imperial Valley croplands and Salton Sea in the southwest corner of the image have higher emissivities,  $>0.95$ . Figure 15 shows the differences in emissivity spectra between the NEM and TES output for pixels over three different surface types (sand dunes, Salton Sea water, and mixed shrubland) for the Imperial Valley cutout. Note that, although both NEM and TES have similar spectral shape, the emissivities of NEM are generally higher than TES because of the initial estimate of  $\epsilon_{max}$  in the NEM module. The Algodones Dunes spectrum has high spectral contrast, which is typical for a quartz spectrum that has the characteristic quartz doublet in the 8–10- $\mu\text{m}$  region, while the emissivity of water is usually spectrally flat, and high.

For pixels with low spectral contrast (e.g., graybody surfaces), the accuracy of MMD calculated from TES is compromised and approaches a value that depends on measurement error and residual errors from incomplete atmospheric correction. For ASTER, which has a NEAT of 0.3 K at 300 K, measurement error contributes to the apparent contrast, and a method was explored to correct the apparent MMD using Monte Carlo simulations. For MODIS (NEAT of 0.05 K), we expect measurement errors to be minimal and atmospheric effects to be the largest contribution to MMD errors. A further problem for graybody surfaces is a loss of precision for

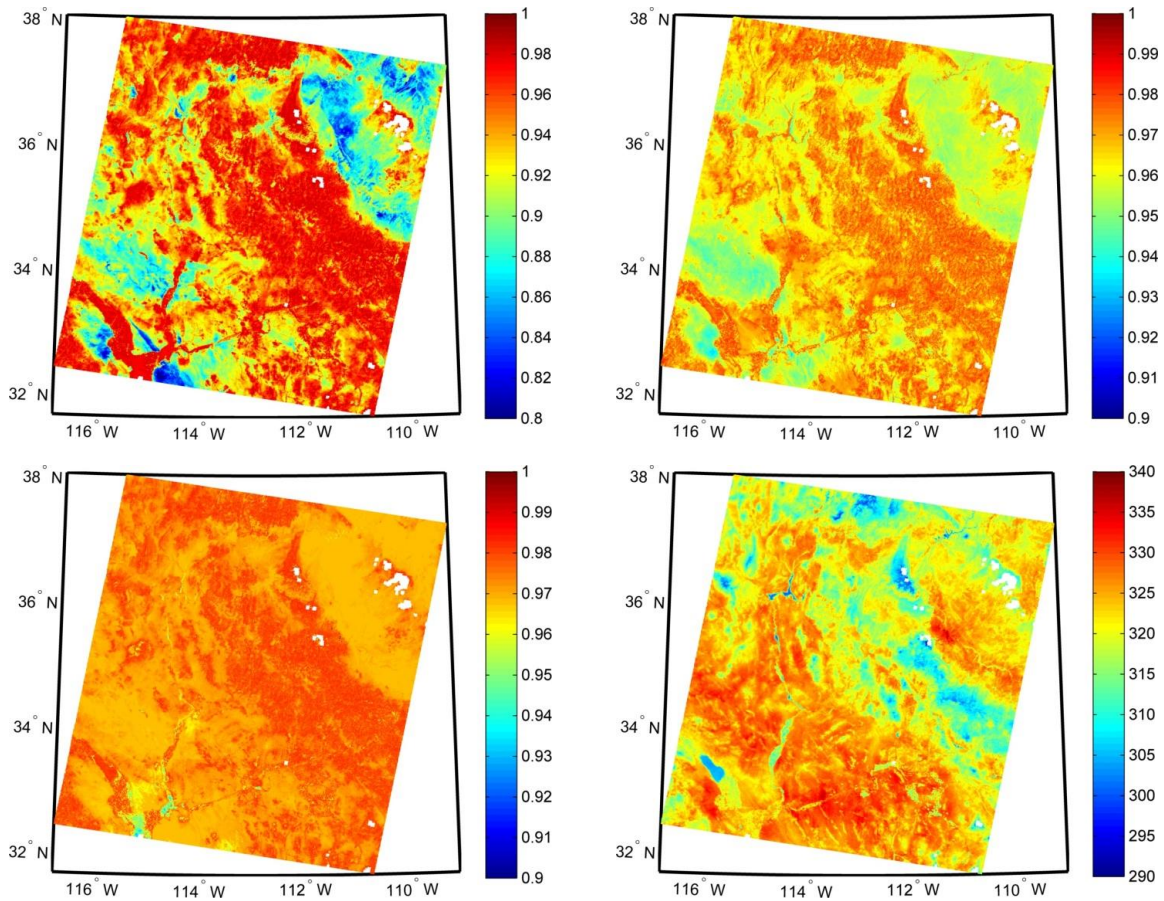


Figure 13. Clockwise from top left: MODIS cutouts of land surface emissivity for band 29 (8.55  $\mu\text{m}$ ); band 31 (11  $\mu\text{m}$ ), band 32 emissivity (12  $\mu\text{m}$ ), and LST output from the TES algorithm over the Imperial Valley, southeastern California on 29 August 2004.

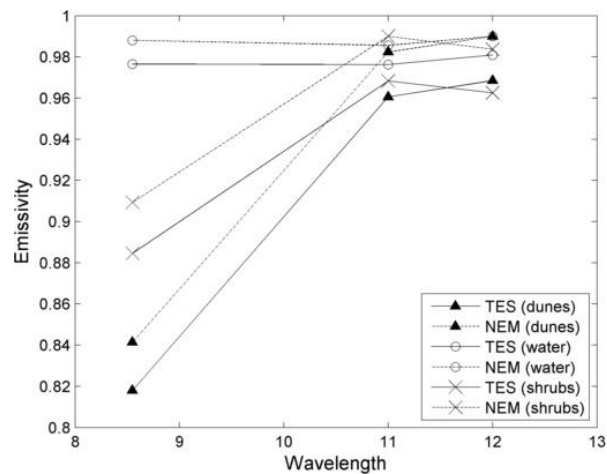


Figure 14. MODIS derived TES and NEM emissivity spectra for three different surface types for the MODIS cutout shown in Figure 11: Algodones Dunes, Salton Sea, and shrublands (mixed soil and vegetation). Details of the TES and NEM outputs from these spectra are shown in Table 7.

low MMD values. This is due to the shape of the power-law curve of  $\epsilon_{min}$  vs. MMD at low MMD values, where small changes in MMD can lead to large changes in  $\epsilon_{min}$ . To address these issues, the ASTER TEWG initially proposed a threshold classifier for graybody surfaces.

If  $MMD < 0.03$ , the value of  $\epsilon_{min}$  in Equation (24) was set to 0.983, a value typical for water and most vegetated surfaces. However, this classification was later abandoned as it introduced large step discontinuities in most images (e.g., from vegetation to mixed-cover types). The consequence of removing the threshold classifier was that, over graybody surfaces, errors in emissivity could range from 0.01 to 0.05 (0.5 K to 3 K) due to measurement error and residuals errors from atmospheric correction (Gustafson et al. 2006; Hulley and Hook 2009b). For MOD21, we use original TES without classification and the WVS method to correct the atmospheric parameters on a pixel-by-pixel basis.

For bare surfaces (rocks, soils, and sand), the error in NEM-calculated T may be as much as 2–3 K, assuming a surface at 340 K due to the fixed assumption of  $\epsilon_{max} = 0.96$ . This error can be corrected by recalculating T using the TES retrieved maximum emissivity,  $\epsilon_{max}^{TES}$ , and the atmospherically corrected radiances,  $R_i$ . The maximum emissivity used as correction for reflected  $L_{\lambda}^{\downarrow}$  will be minimal.

$$T^{TES} = \frac{c_2}{\lambda_{max}} \left( \ln \left( \frac{c_1 \epsilon_{max}^{TES}}{\pi R_i \lambda_{max}^5} + 1 \right) \right)^{-1} \quad (28)$$

An example MODTES surface temperature output image is shown in Figure 14. Bare areas of the Mojave desert generally have the highest temperatures with  $T > 330$  K, while graybody surfaces such as the Imperial Valley croplands and Salton Sea in the southwest corner have the coolest temperatures with  $T < 310$  K.

In the original ASTER TES algorithm, a final correction is made for sky irradiance using the TES temperature and emissivities; however, this was later removed, as correction was minimal and influenced by atmospheric correction errors. This additional correction is not used for the MODTES algorithm.

### 7.2.9 MMD vs. $\epsilon_{min}$ Regression

The relationship between MMD and  $\epsilon_{min}$  is physically reasonable and is determined using a set of laboratory spectra in the ASTER spectral library v2.0 (Baldrige et al. 2009a) and referred to as the calibration curve. The original ASTER regression coefficients were determined from a

set of 86 laboratory reflectance spectra of rocks, soils, water, vegetation, and snow supplied by J.W. Salisbury from Johns Hopkins University. One question that needed to be answered was whether using a smaller or larger subset of this original set of spectra changed the results in any manner. Establishing a reliable MMD vs.  $\epsilon_{min}$  relationship with a subset of spectral representing all types of surfaces is a critical assumption for the calibration curve. This assumption was tested using various combinations and numbers of different spectra (e.g., Australian rocks, airborne data, and a subset of 31 spectra from Salisbury), and all yielded very similar results to the original 86 spectra.

For MODIS, the original 86 spectra were updated to include additional sand spectra used to validate the North American ASTER Land Surface Emissivity Database (NAALSED) (Hulley and Hook 2009b) and additional spectra for vegetation from the MODIS spectral library and ASTER spectral library v2.0, giving a total of 150 spectra. The data were convolved to the three MODIS TIR bands and  $\epsilon_{min}$  and  $\beta_i$  spectra calculated using Equation (21) for each sample. The MMD for each spectrum was then calculated from the  $\beta_i$  spectra and regressed to the  $\epsilon_{min}$  values. The relationship follows a simple power law given by Equation (23), with regression coefficients  $\alpha_1 = 0.997$ ,  $\alpha_2 = 0.7050$ , and  $\alpha_3 = 0.7430$ , and  $R^2 = 0.987$ . Figure 16 shows the power-law relationship between MMD and  $\epsilon_{min}$  using the 150 lab spectra.

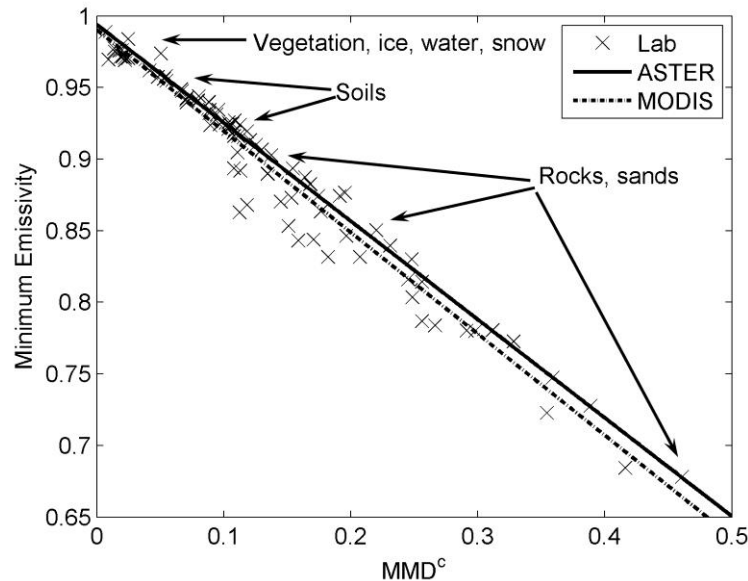


**Figure 15. MODIS and ASTER calibration curves of minimum emissivity vs. MMD. The lab data (crosses) are computed from 150 spectra consisting of a broad range of terrestrial materials (rocks, sand, soil, water, vegetation, and ice).**

### 7.2.10 Atmospheric Effects

The accuracy of the atmospheric correction technique used to estimate the surface radiance relies on the accuracy of the variables input to the radiative transfer model (e.g., air temperature, relative humidity, and ozone). A sensitivity analysis has shown (Table 4) that a change in atmospheric water vapor of 20% leads to a 4.43% change in radiance for MODIS band 12 (12  $\mu\text{m}$ ), which is the most susceptible to atmospheric absorption and emission of the three MODIS TIR bands, while a change in air temperature of 2 K leads to a  $-1.6\%$  change in radiance for a tropical atmosphere. Changes in ozone and aerosol amount had much smaller effects, except for MODIS band 29 (8.55  $\mu\text{m}$ ), which falls closer to the ozone absorption region at 9.6  $\mu\text{m}$ . These atmospheric errors tend to be highly correlated from band to band, since each channel has a characteristic absorbing feature. As a result, the effect on TES output is usually relatively small, but if these errors are uncorrelated from band to band then much larger errors can occur, particularly for graybodies, where small changes in MMD can significantly alter the shape of the emissivity spectrum. For example, over water bodies, errors in emissivity of up to 3% (0.03) have been found due to uncompensated atmospheric effects (Hulley and Hook 2009b; Tonooka and Palluconi 2005).

One method for improving the accuracy of the surface radiance product is to apply the WVS method (Tonooka 2005). Using 183 ASTER scenes over lakes, rivers, and sea surfaces, it was found that using the WVS method instead of the standard atmospheric correction improved estimates of surface temperature from 3 to 8 K in regions of high humidity (Tonooka 2005). These are substantial errors when considering that the required accuracy of the TES algorithm is  $\sim 1$  K (Gillespie et al. 1998).

Figure 17 shows emissivity spectra over the Salton Sea, showing the effects of applying the WVS atmospheric correction method on the shape of the emissivity spectrum when compared to using the standard (STD) correction method without WVS. The emissivity spectrum of water is high ( $\sim 0.98$ ) and flat and the results in Figure 17 show a dramatic improvement in emissivity accuracy in both magnitude (up to 0.06 for ASTER band 11, and 0.09 for MODIS band 29) and spectral shape when using the WVS as opposed to the STD method. Because of the humid day, where MOD07 precipitable water vapor (PWV) values were around 4 cm over the water, the spectral contrast of the STD emissivity results are overestimated for ASTER and MODIS data. However, when applying the WVS method, the ASTER emissivity spectra fall within 0.015 of the

lab-measured spectrum, while MODIS emissivity spectra are within 0.005 at all wavelengths. Differences between the 3- and 5-band TES algorithm applied to ASTER data were small.

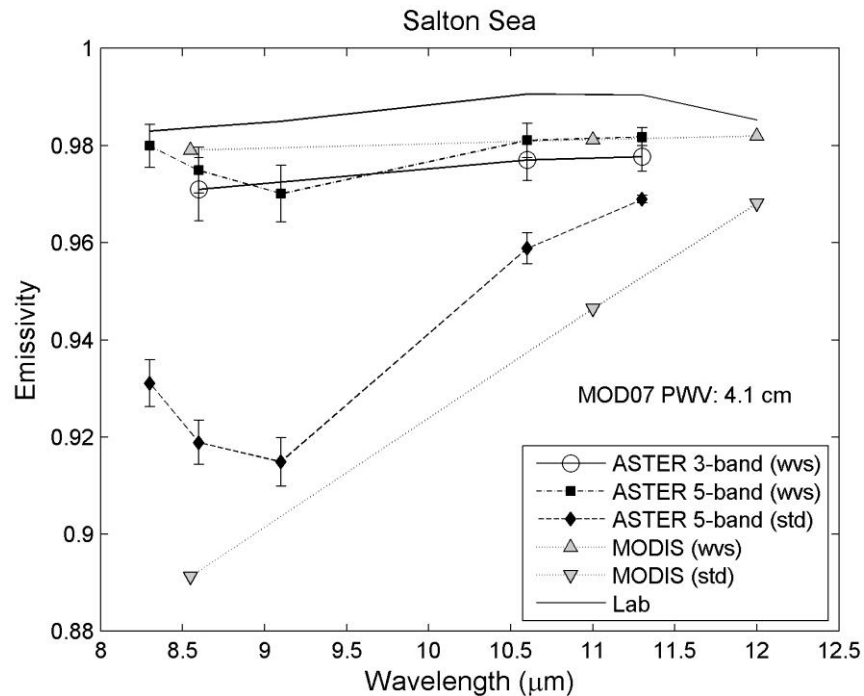


Figure 16. Emissivity spectra comparisons on June 15, 2000 over the Salton Sea between ASTER (3-band), ASTER (5-band), and MODTES, using the TES algorithm along with lab spectra of water from the ASTER spectral library. Results from the WVS method and the STD atmospheric correction are also shown. An estimate of the PWV from the MOD07 atmospheric product indicates very high humidity on this day.

## 8 Advantages of TES over SW approaches

The LST accuracy of SW algorithms is strongly dependent on emissivity variability (Wan and Dozier 1996; Yu et al. 2005). Any errors in the assigned SW classification emissivities can translate into large errors in LST. For example, Galve et al. (2008) showed that, on average, a band emissivity error of 0.005 (0.5%) will result in an LST error of 0.7 K using the SW approach. The sensitivity of the current MODIS GSW algorithm to the view zenith angle is of roughly of the same magnitude as emissivity, but can be compensated for by introducing an atmospheric path-length term, while sensitivity to differences in surface and air temperature are typically much smaller, but can be large over bare areas.

Classification emissivity errors can stem from three main sources: 1) misclassification in the original cover type, 2) errors in emissivity within the cover-type map, or 3) a dynamic change

in the cover-type map. A misclassification in cover type will occur when the land class algorithm does not classify the true cover type correctly. According to a validation study on MODIS land cover product, it was found that the accuracy of individual classes ranged from 60–90% (Strahler et al. 2002). Emissivity errors within a cover-type map occur when a class (e.g., barren) does not represent the range in emissivities within that class. And lastly, dynamic errors occur after sudden natural surface changes, e.g., rainfall, wildfires, or phenological changes, resulting in emissivity changes within the land cover type. Error sources 1) and 3) can be grouped together since they both arise due to misclassification.

### **8.1 Land Cover Misclassification**

The first emissivity error source we investigate arises from land cover misclassification. We looked at the effects of a dynamic land cover change on emissivity and LST retrieved values after the Station fire in Los Angeles, which burned nearly 161,000 acres of land in the Angeles National Forest region from 26 August–19 September 2009. Figure 18 shows emissivity (left panels) and LST images (right panels) for ASTER and MODIS data on 10 October 2009. Top and middle panels show ASTER and MODIS (MODTES) results using the TES algorithm, and bottom panels show the MOD11 band 31 (11  $\mu$ m) emissivity classification (left) and MOD11 LST (right).

The Station fire burn area is clearly seen in the center of the ASTER and MODTES results as an area of lower emissivity in the longwave region, and is roughly 0.04 (4%) lower than a typical value for vegetation of 0.98. This decrease in emissivity is not evident in the MODIS GSW results in which the emissivity has been assigned to a forest land cover type with a value of 0.981. The ASTER and MODIS TES results show corresponding high LSTs (320–325 K) over the burn region, while MOD11 LSTs are 5–12 K lower and range from 312–316 K over the burn scar area as shown in Figure 18. This is a direct consequence of not taking the change in emissivity into account. This error far exceeds the specification for the MODIS product (1 K) (Wan 1999) and the VIIRS product (2.5K) (Yu et al. 2005).

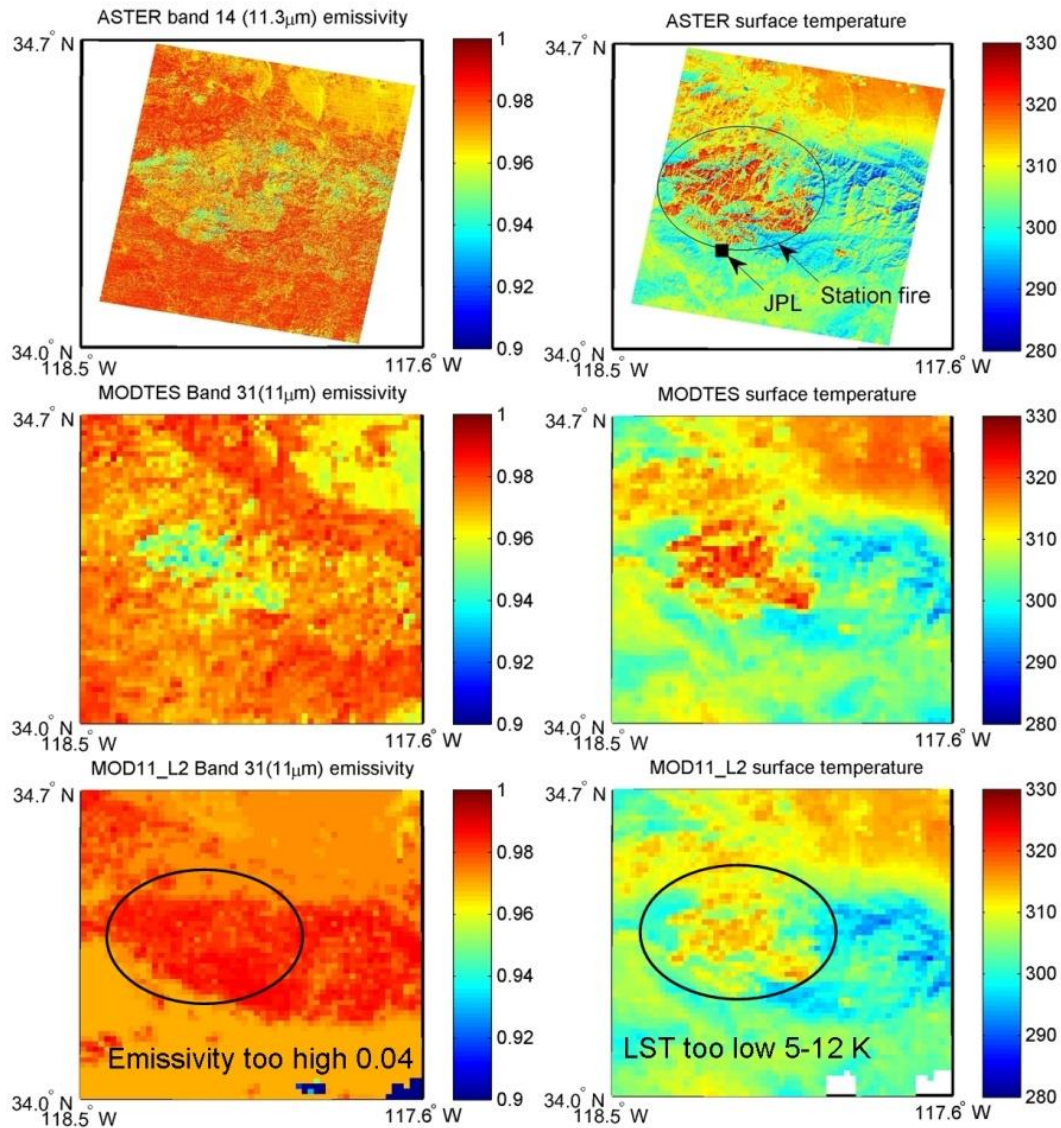
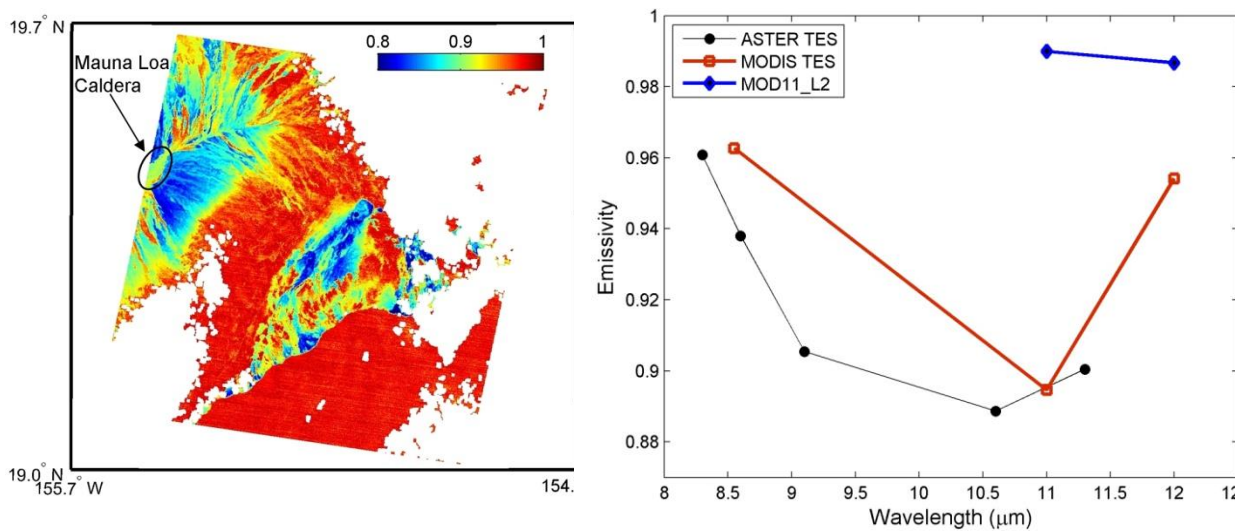


Figure 17. Emissivity images (left) and surface temperature images (right) for ASTER (top), MODIS TES (MODTES) (center) and MODIS SW (MOD11\_L2) (bottom) products over the Station Fire burn scar just north of Pasadena, CA. Location of JPL in Pasadena and burn scar area indicated at top right. MODTES and ASTER results match closely; however, the MOD11\_L2 temperatures are underestimated by as much as 12 K, due to an incorrect emissivity classification.

## 8.2 Emissivity Error within Cover Type

The second major emissivity error in land-cover-type algorithms occurs when the classification is correct, but the emissivities assigned to the class are incorrect. Here we show an example over Mauna Loa caldera in Hawaii (Figure 19). The caldera is approximately 5×3 km in size and consists of flat, smooth pahoehoe basalt with minimal vegetation (Sabol et al. 2009).

Figure 19 shows an ASTER emissivity image (9.1  $\mu\text{m}$ ) of the Mauna Loa region on the 5 June 2000 with the caldera indicated on the map. The accompanying emissivity spectra show ASTER, MODTES and MOD11 classification-based emissivities for bands 31 and 32. It is clear the ASTER and MODTES spectra match closely and show the characteristic basalt emissivity minima in the 10.5–11.5  $\mu\text{m}$  region, while the MOD11 classification emissivities are too high by almost 0.1 in band 31, and 0.04 in band 32. Consequently there is a large discrepancy of up to 12 K between the MODTES and the MOD11 LST product as a result of MOD11 misclassification. This far exceeds the specification for the MOD11 product accuracy (1 K) (Wan 1999) and the VIIRS product (2.5 K) (Yu et al. 2005).



**Figure 18. (left) ASTER band 12 (9.1  $\mu\text{m}$ ) emissivity image over Mauna Loa caldera, Hawaii on 5 June 2000, and (right) emissivity spectra from ASTER, MODTES, and MOD11 emissivity classification. While ASTER and MODTES agree closely, MOD11 emissivities are too high, resulting in large LST discrepancies between MODTES and MOD1 (12 K) due to misclassification in bands 31 (11  $\mu\text{m}$ ) and 32 (12  $\mu\text{m}$ ).**

### 8.3 Soil Moisture Effects

LST errors of this magnitude will occur in a systematic fashion any time that the classification emissivities do not reflect the true spectral shape of the surface being measured. Other factors contributing to emissivity variability include rainfall, which increases the surface soil moisture, and therefore the emissivity due to lower reflectance over bare surfaces.

An example of the effects of rainfall on the emissivity is shown in Figure 20. Hulley et al. (2010) used a case study over the Namib desert to show that the emissivity of bare soils retrieved from physical algorithms such as TES and the MODIS day/night algorithm increased by up to 0.03

due to soil moisture changes in the thermal bands used by SW algorithms (11  $\mu\text{m}$ ), while the SW emissivity values were held constant throughout the rainfall period (19–23 April). The MODIS SW product had cooler mean temperatures of more than 2 K as a result of not taking into account these emissivity changes. Again, a 0.5–1 K LST error can lead to a 10% error in sensible heat flux and evapotranspiration, and a 1–3 K error can lead to surface flux errors of up to 100  $\text{W}/\text{m}^2$  (Yu et al. 2005). Other examples of emissivity misclassification could occur due to intra-annual crop rotation, where fields may go from bare to fully vegetated over short time periods.

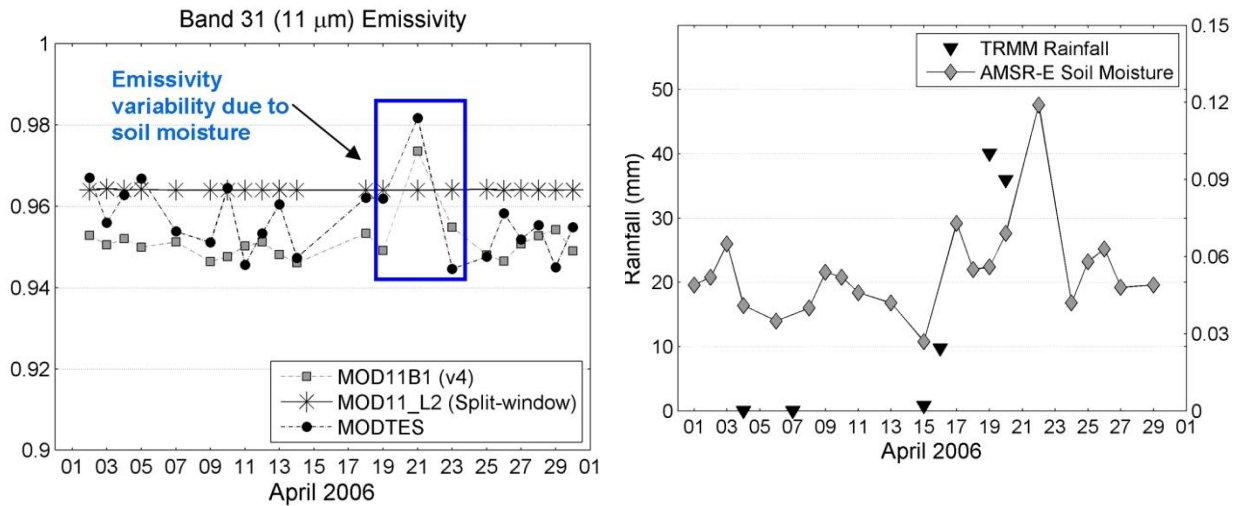


**Figure 19. (top) Emissivity variation for a rainfall event over the Namib desert showing results from MOD11B1 v4 (day/night algorithm), MOD11\_L2 (SW), and MODIS TES (MODTES). (bottom) Corresponding soil moisture variation from AMSRE-E and rainfall estimates from the Tropical Rainfall Measuring Mission (TRMM). It is clear that the physical retrievals, show increases in emissivity due to soil moisture, whereas the SW values are held constant throughout the rainfall period from 15–21 April. From Hulley et al. (2010).**

## **9 Quality Assessment and Diagnostics**

Please see the MOD21 User Guide for a fully detailed description of the Quality Control and Diagnostics available in the product.

## 10 Uncertainty Analysis

NASA has identified a major need to develop long-term, consistent products valid across multiple missions, with well-defined uncertainty statistics addressing specific Earth-science questions. These products are termed Earth System Data Records (ESDRs), and LST&E has been identified as an important ESDR. Currently a lack of understanding of LST&E uncertainties limits their usefulness in land surface and climate models. In this section we present results from an LST&E uncertainty simulator that has been developed to quantify and model uncertainties for a variety of TIR sensors and LST algorithms (Hulley et al. 2012). Using the simulator, uncertainties were estimated for the MOD21 LST&E product, including WVS. These uncertainties are parameterized according to view angle and estimated total column water vapor for application to real MODIS data.

### 10.1 The Temperature and Emissivity Uncertainty Simulator

A Temperature Emissivity Uncertainty Simulator (TEUSim) has been developed for simulating LST&E uncertainties from various sources of error for the TES and SW algorithms in a rigorous manner for any appropriate TIR sensor. These include random errors (noise), systematic errors (calibration), and spatio-temporally correlated errors (atmospheric). The MODTRAN 5.2 radiative transfer model is used for the simulations with a global set of radiosonde profiles and surface emissivity spectra representing a broad range of atmospheric conditions and a wide variety of surface types. This approach allows the retrieval algorithm to be easily evaluated under realistic but challenging combinations of surface/atmospheric conditions. The TEUSim is designed to separately quantify error contributions from the following potential sources:

- Noise
- Model
- Atmospheric correction
- Undetected cloud
- Calibration

The results presented in this study will focus on the first three of these error sources: noise, model, and atmosphere.

## 10.2 Atmospheric Profiles

The TEUSim uses a global set of atmospheric radiosoundings constructed from the University of Wyoming Atmospheric Science Department's CLAR database (Galve et al. 2008). CLAR contains 382 globally distributed radiosoundings for both day and night in 65 layers from the surface to 100 km. The CLAR database includes a wide range of TCW estimates up to 7 cm and surface air temperature ranging from  $-20^{\circ}$  C to  $40^{\circ}$  C. Radiosondes acquired from 2003 to 2006 were distributed over three latitude ranges (40% from  $0^{\circ}$ – $30^{\circ}$ , 40% from  $30^{\circ}$ – $60^{\circ}$ , 20% above  $60^{\circ}$ ) and screened for cloud and fog contamination using a procedure described by Francois et al. (2002).

## 10.3 Radiative Transfer Model

In TEUSim the latest version of MODTRAN (v5.2) was used for the radiative transfer calculations. MODTRAN 5.2 uses an improved molecular band model, termed the Spectrally Enhanced Resolution MODTRAN (SERTRAN), which has a much finer spectroscopy ( $0.1\text{ cm}^{-1}$ ) than previous versions ( $1\text{--}2\text{ cm}^{-1}$ ). This results in higher accuracy in modeling of band absorption features in the longwave TIR window regions, and comparisons with line-by-line models has shown good accuracy (Berk et al. 2005).

## 10.4 Surface End-Member Selection

A selection of emissivity spectra from the ASTER Spectral Library v2.0 (ASTlib) (Baldrige et al. 2009a) were used to define the surface spectral emission term in MODTRAN. A total of 59 spectra were chosen based on certain criteria and grouped into four surface classifications: rocks (20), soils (26), sands (9), and graybodies (4). The doublets between  $8\text{--}9.5\text{ }\mu\text{m}$  and  $12.5\text{--}13\text{ }\mu\text{m}$  are the result of Si-O stretching, and the exact position of the feature at  $11.2\text{ }\mu\text{m}$  is dependent on the size of the cation paired with the carbonate ( $\text{CO}_3$ ) molecule. Spectra were chosen to represent the most realistic effective emissivities observed at the remote sensing scales of ASTER (90 m) and MODIS (1 km) using the following methodology.

For rocks, certain spectra were removed prior to processing based on two considerations. First, samples that rarely exist as kilometer-scale, sub-aerial end-member exposures on the Earth's surface such as pyroxenite or serpentinite were eliminated. Second, and in parallel, spectrally similar samples were eliminated. Spectral similarity was defined by the location, shape, and

magnitude of spectral features between 7 and 13  $\mu\text{m}$ . All eliminated samples are represented in the final selection through spectrally-similar end-member types. The final rock set included 20 spectra.

ASTlib includes 49 soil spectra classified according to their taxonomy, such as Alfisol (9), Aridisol (14), Entisol (10), Inceptisol (7) and Mollisol (9). Filtering in this case was based solely on spectral similarity between each taxonomy type. The final soils set included 26 soil spectra.

A set of nine emissivity spectra collected in separate field campaigns during 2008 over large homogeneous sand dune sites in the southwestern United States in support of validation for the NAALSED v2.0 (Hulley et al. 2009b) were used for sands. The sand samples consist of a wide variety of different minerals including quartz, magnetite, feldspars, gypsum, and basalt mixed in various amounts, and represent a broad range of emissivities in the TIR as detailed in Hulley et al. (2009b).

To represent graybody surfaces, spectra of distilled water, ice, snow, and conifer were chosen from ASTlib. Four spectra were sufficient to represent this class since graybody surfaces exhibit low contrast and high emissivities. It should be noted that certain types of man-made materials were not included, such as aluminum roofs that do not occur at the spatial resolution of these sensors, but should be included for higher-spatial-resolution data sets such as those provided by airborne instruments.

## 10.5 Radiative Transfer Simulations

In the TEUSim, each CLAR radiosonde profile for each set of end-member spectra was used as an input to MODTRAN 5.2. A seasonal rural aerosol was assumed with standard profiles for fixed gases within MODTRAN. For MODIS, five viewing angles were used, representing the Gaussian angles proposed by Wan and Dozier (1996):  $0^\circ$ ,  $11.6^\circ$ ,  $26.1^\circ$ ,  $40.3^\circ$ , and  $53.7^\circ$ . In the WVS simulation model, the downward sky irradiance,  $L_\lambda(\theta)$ , can be modeled using the path radiance, transmittance, and view angle. To simulate the downward sky irradiance in MODTRAN, the sensor target is placed a few meters above the surface, with surface emission set to zero, and view angle set at the prescribed angles above. In this configuration, the reflected downwelling sky irradiance is estimated for a given view angle. The total sky irradiance contribution for band  $i$  is then calculated by summing the contribution of all view angles over the entire hemisphere:

$$L_i^\downarrow = \int_0^{2\pi} \int_0^{\pi/2} L_i^\downarrow(\theta) \cdot \sin\theta \cdot \cos\theta \cdot d\theta \cdot d\delta \quad (29)$$

where  $\theta$  is the view angle and  $\delta$  is the azimuth angle. To minimize computational time, the downward sky irradiance is first modeled as a non-linear function of path radiance at nadir view using (1) (Tonooka 2001):

$$L_i^\downarrow(\gamma) = a_i + b_i \cdot L_i^\uparrow(0, \gamma) + c_i L_i^\uparrow(0, \gamma)^2 \quad (30)$$

where  $a_i$ ,  $b_i$ , and  $c_i$  are regression coefficients, and  $L_i^\uparrow(0, \gamma)$  is computed by:

$$L_i^\uparrow(0, \gamma) = L_i^\uparrow(\theta, \gamma) \cdot \frac{1 - \tau_i(\theta, \gamma)^{\cos\theta}}{1 - \tau_i(\theta, \gamma)} \quad (31)$$

Equations (27) and (28) were used to estimate the downwelling sky irradiance in the TEUSim results using pre-calculated regression coefficients for MODIS bands 29, 31, and 32. The reflected sky irradiance term is generally smaller in magnitude than the surface-emitted radiance, but needs to be taken into account, particularly on humid days when the total atmospheric water vapor content is high. The simulated LST is based on the surface air temperature in the CLAR database as follows:

$$LST_{sim} = T_{air} + \delta T \quad (32)$$

where  $LST_{sim}$  and  $T_{air}$  are the simulated LST and surface air temperature. Galve et al. (2008) found a mean  $\delta T$  of +3 K and standard deviation of 9 K from a global study of surface-air temperature differences over land in the MODIS MOD08 and MOD11 products. We therefore defined  $\delta T$  as a random distribution with a mean of 3 K and a standard deviation of 9 K for each profile input to MODTRAN.

The TES algorithm uses surface radiance as input, which can be derived from the atmospheric transmittance  $\tau_\lambda(\theta)$ , TOA radiance  $L_\lambda(\theta)$ , path radiance  $L_\lambda^\uparrow(\theta)$ , and downward sky irradiance  $L_\lambda^\downarrow(\theta)$ . To calculate the various sources of error in LST&E retrievals from TES, these variables were simulated for the following conditions:

1. Perfect atmosphere (i.e., exact inputs):  $L_\lambda(\theta)$  and atmospheric parameters  $\tau_\lambda(\theta)$ ,  $L_\lambda^\uparrow(\theta)$ , and  $L_\lambda^\downarrow(\theta)$  calculated using a given profile, surface type and viewing angle;
2.  $L_\lambda(\theta)$  and adjusted atmosphere (i.e., imperfect inputs):  $\tau_\lambda'(\theta)$ ,  $L_\lambda'^\uparrow(\theta)$ , and  $L_\lambda'^\downarrow(\theta)$  calculated using perturbed temperature and humidity profiles to simulate real input data;
3. Adjusted atmosphere as in (2) but with humidity scaled by a factor of 0.7 for deriving inputs to the WVS method; and

4.  $L_{\lambda}(\theta)$  calculated using a graybody surface type (conifer was chosen with emissivity close to 0.99), as the scaling factors in the WVS method are initialized over graybody surfaces.

The above conditions were run for ‘perfect’  $L_{\lambda}(\theta)$  and also with adding random noise to the radiances based on the sensor’s noise equivalent delta temperature NE $\Delta$ T (0.05 K for MODIS).

The WVS method is used for improving the accuracy of the atmospheric parameters output from MODTRAN using an EMC/WVD algorithm that models the surface brightness temperature (BT) given the at-sensor brightness temperature along with an estimate of the total water vapor (Tonooka 2001, 2005). The modeled surface BT is then used to determine a WVS correction factor, which for real data is first calculated over all graybody pixels on a given scene and then spatially interpolated using an inverse distance method over the remaining non-graybody pixels within the scene. Simulation Steps (3) and (4) are needed to simulate the input for the WVS method.

## 10.6 Error Propagation

The set of 382 CLAR radiosonde profiles were adjusted to simulate real data by applying estimated uncertainties from the MODIS MOD07 atmospheric product (Seemann et al. 2006; Seemann et al. 2003). Using a dataset of 80 clear sky cases over the SGP ARM site (Tobin et al. 2006), MOD07 air temperature RMS errors showed a linearly decreasing trend from 4 K at the surface to 2 K at 700 mb, and a constant 2 K above 700 mb (Seemann et al. 2006). These reported values were used to perturb the air temperature profiles at each associated level using a random number generator with a mean centered on the RMS error. The uncertainty of the water vapor retrievals were estimated to be between 10–20% (Seemann et al. 2006). Accordingly, the relative humidity profiles were adjusted by scaling factors ranging from 0.8 to 1.2 in MODTRAN using a uniformly distributed random number generator.

The total LST uncertainty for the TES algorithm based on model, atmospheric and measurement noise contributions can be written as:

$$\delta LST_{TES} = [\delta LST_M + \delta LST_A + \delta LST_N]^{1/2} \quad (33)$$

where  $\delta LST_M$  is the model error due to assumptions made in the TES calibration curve,  $\delta LST_A$  is the atmospheric error, and  $\delta LST_N$  is the error associated with measurement noise. These errors are assumed to be independent.

To calculate the separate contributions from each of these errors let us first denote the simulated atmospheric parameters as  $x = [\tau_\lambda(\theta), L_\lambda^\uparrow(\theta), L_\lambda^\downarrow(\theta)]$  and simulated observed radiance parameter as  $y = L_\lambda(\theta)$ . Both  $x$  and  $y$  are required to estimate the surface radiance that is input to the TES algorithm. In reality, however, the input parameters  $x$  are not known explicitly, but are associated with some error,  $\delta x$ , which we write as  $\hat{x} = x + \delta x$ . Similarly, the observed radiances have an associated noise based on the NE $\Delta$ T of the specific sensor, which we will denote by  $\hat{y}$ . To characterize the model error, we express the TES algorithm as a function based on perfect input parameters  $x$  and  $y$  such that  $LST_{TES} = f(x, y)$ . The model error,  $\delta LST_M$ , i.e., due to assumptions in the TES algorithm alone, can then be written as:

$$\delta LST_M = E[(f(x, y) - LST_{sim})^2 | x, y]^{1/2} \quad (34)$$

where  $LST_{sim}$  is the simulated LST used in the MODTRAN simulations, and  $E[\cdot | x, y]$  denotes the mean-square error between the retrieved and simulated LST for inputs  $x$  and  $y$ . The atmospheric error can be written as the difference between TES using perfect atmospheric inputs,  $x$  and imperfect inputs,  $\hat{x}$ :

$$\delta LST_A = E\left[(f(\hat{x}, y) - f(x, y))^2 | x, y\right]^{1/2} \quad (35)$$

And lastly the error due to measurement noise can be written as the difference between TES with perfect simulated TOA radiances,  $y$  and TES with noisy radiances,  $\hat{y}$ :

$$\delta LST_N = E\left[(f(x, \hat{y}) - f(x, y))^2 | x, y\right]^{1/2} \quad (36)$$

Since the TES algorithm simultaneously retrieves the LST and spectral emissivity, the above equations also apply to the corresponding emissivity retrieval for each band.

The effects of sensor view angle on the accuracy of MODIS TES retrievals of LST are shown in Figure 21. LST uncertainties are plotted against TCW for four simulated Gaussian view angles of  $0^\circ$ ,  $26.1^\circ$ ,  $40.3^\circ$ , and  $53.7^\circ$ . It is clear that the uncertainties become larger with both TCW and view angle; however, this is due to TCW in both cases. A TCW amount of 4 cm at a  $53.7^\circ$  view angle has an effective TCW of 6.2 cm, due to an increase in atmospheric path length increases by a factor of  $\cos^{-1}(53.7^\circ)$ . The LSTs are underestimated at higher view angles by as much as 10 K, most likely due to unaccounted-for non-linear effects in the radiative transfer process due to longer atmospheric pathlengths. For real data, angular anisotropy of surface emissivity will also result in higher uncertainties at view angles above  $\sim 40^\circ$  due to non-Lambertian behavior of certain types of soils and sands (Snyder et al. 1997), and also from highly structured (3-D) surfaces such

as shrublands, savannas, woodlands and forests. This variability primarily arises from the changing proportions of scene endmembers visible at different view zenith angles (Yu et al. 2006).

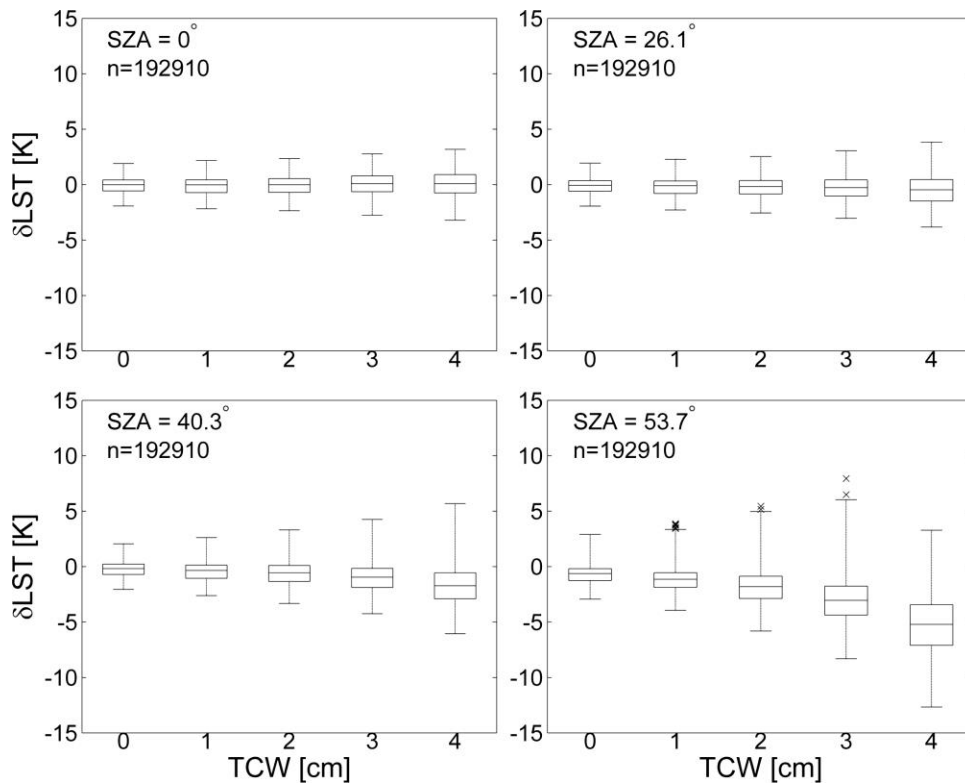


Figure 20. MODIS LST uncertainties using the TES algorithm versus TCW for four viewing Gaussian angles of  $0^\circ$ ,  $26.1^\circ$ ,  $40.3^\circ$ , and  $53.7^\circ$ . The value  $n$  represents the number of data points used for a specific land surface type, in this case bare surfaces (rocks, soils, sands).

## 10.7 Parameterization of Uncertainties

A key requirement for generating LST&E ESDR from either multiple sensors or algorithms is accurate knowledge of uncertainties from the contributing products. Uncertainties for each input product must be rigorously estimated for a variety of different conditions on a pixel-by-pixel basis before they can be merged and incorporated into a time series of measurements of sufficient length, consistency, and continuity to adequately meet the science requirements of an ESDR. Current LST&E datasets are available with quality control information, but do not include a full set of

uncertainty statistics. For example, the standard ASTER and MODIS LST product QC data planes specify qualitative uncertainty information, and MODIS includes a rough estimate of LST&E error, but no uncertainty data-planes exist on a pixel-by-pixel basis dependent upon factors such as land cover type, view angle, and total column water vapor.

The next logical step is to apply the uncertainty statistics produced from the TEUSim to real data from MOD21 retrievals. To achieve this the total uncertainty, taken as the RMSE of the differences between simulated (truth) and retrieved LST&E including atmospheric error, was modeled according to view angle, total water vapor column amount, and land surface type using a least-squares method fit to a quadratic function. Three surface types were classified: graybody, transitional, and bare. The transitional surface represents a mixed cover type, and was calculated by varying the vegetation fraction cover percentage,  $f_v$ , by 25, 50, and 75% for the set of bare surface spectra (rocks, soils, sand) as follows:

$$\varepsilon_{trans} = \varepsilon_{gray} \cdot f_v + \varepsilon_{bare} \cdot (1 - f_v) \quad (37)$$

where  $\varepsilon_{trans}$  is the transition emissivity,  $\varepsilon_{gray}$  is a graybody emissivity spectrum (e.g., conifer), and  $\varepsilon_{bare}$  are the lab emissivities for bare surfaces.

For MODIS, the total uncertainty includes both a sensor view angle (SVA) and TCW dependence. The total uncertainty for MODIS LST can be expressed as:

$$\begin{aligned} \delta LST_{MODIS} = & a_o + a_1 TCW + a_2 SVA + a_3 TCW \cdot SVA + a_4 TCW^2 \\ & + a_5 SVA^2 \end{aligned} \quad (38)$$

Similarly, the band-dependent emissivity uncertainties can be expressed as:

$$\delta \varepsilon_{i,MODIS} = a_{i,o} + a_{i,1} TCW + a_{i,2} SVA + a_{i,3} TCW \cdot SVA + a_{i,4} TCW^2 + a_{i,5} SVA^2 \quad (39)$$

where  $\delta LST$  is the LST uncertainty (K) calculated as the difference between the simulated and retrieved LST,  $\delta \varepsilon_i$  is the band-dependent emissivity uncertainty for band  $i$ , calculated as the difference between the input lab emissivity and retrieved emissivity, and  $a_i$  and  $a_{i,j}$  are the LST and emissivity regression coefficients and depend on surface type (graybody, transition, bare).

A sensitivity study showed that the parameterizations given by equations 10–13 provided the best fit to the simulation results in terms of RMSE, with fits of ~0.1 K. Once the coefficients are established they can be applied on a pixel-by-pixel basis across any scene given estimates of TCW from either a retrieval (e.g., MODIS MOD07 or AIRS) or a numerical weather model (e.g., ECMWF, NCEP), and the SVA from the product metadata. A simple emissivity threshold using a

band with large spectral variation can be used to discriminate between graybody, transition, and bare types in any given scene for application of the relevant coefficients.

Figure 22(a) shows the retrieved LST using the TES algorithm with WVS correction and corresponding uncertainty in Figure 22(c), while Figure 22(b) shows the retrieved emissivity for band 29 and corresponding uncertainty in Figure 22(d). The highest LST uncertainties range from 2–3 K in the monsoonal region to over 5 K on the edges of cloudy regions, where uncertainties are highest as expected. Over most of the scene where TCW values are  $<2$  cm, the LST uncertainties are generally  $<1.5$  K. Similar to the LST results, the uncertainties in band 29 emissivity are highest over the monsoonal region, ranging from 0.03–0.05, and along the edges of clouds. Over drier regions of California and Nevada, there is a stronger uncertainty correlation with cover type, with lowest uncertainties over the denser forests of the Sierra Nevadas ( $\sim 0.015$ ) and slightly higher over bare and mixed regions ( $\sim 0.02$ ). For this scene, retrievals were restricted to view angles  $<40^\circ$ , so uncertainty dependencies related to view angle are not evident; however, at angles  $>40^\circ$  the uncertainties for both LST and emissivity increase noticeably due to reasons discussed earlier.

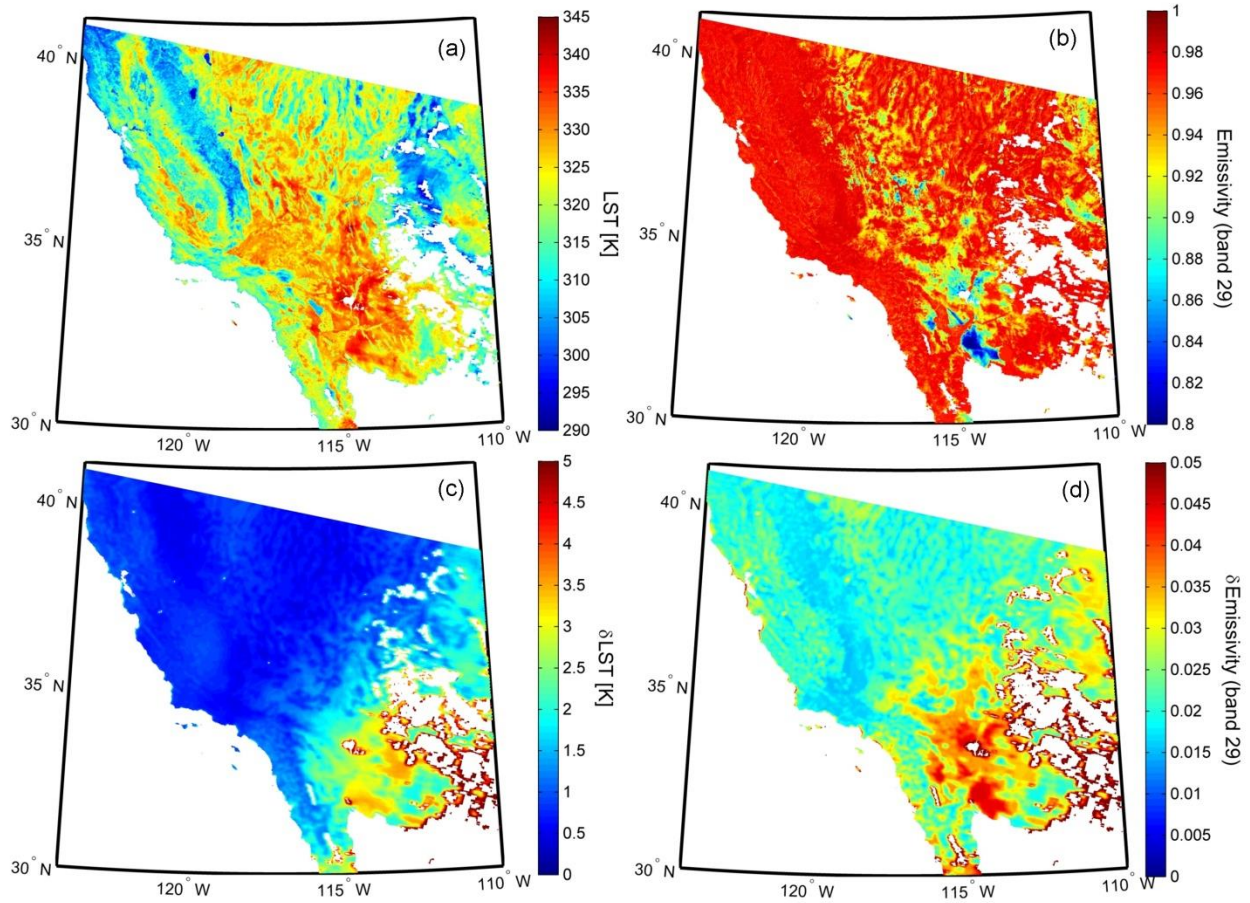


Figure 21. MODIS TES retrievals including WVS correction over the southwestern United States on 7 August 2004: (a) (top left) LST, (b) (top right) emissivity for band 29 (8.55  $\mu\text{m}$ ), (c) (bottom left) LST uncertainty, and (d) (bottom right) emissivity uncertainty for band 29 (8.55  $\mu\text{m}$ ). White areas over land indicate areas of cloud that have been masked out using the MOD35 cloud mask product.

## 11 Validation

Two methods have been established for validating MODIS LST data: a conventional T-based method and an R-based method (Wan and Li 2008). The T-based method requires ground measurements over thermally homogenous sites concurrent with the satellite overpass, while the R-based method relies on a radiative closure simulation in a clear atmospheric window region to estimate the LST from top of atmosphere (TOA) observed brightness temperatures, assuming the emissivity is known from ground measurements. The T-based method is the preferred method, but it requires accurate in-situ measurements that are only available from a small number of thermally homogeneous sites concurrently with the satellite overpass. The R-based method is not a true validation in the classical sense, but it does not require simultaneous in-situ measurements and is therefore easier to implement both day and night over a larger number of global sites; however, it is susceptible to errors in the atmospheric correction and emissivity uncertainties. The MOD11\_L2 LST product has been validated with a combination of T-based and R-based methods over more than 19 types of thermally homogenous surfaces including lakes (Hook et al. 2007), dedicated field campaign sites over agricultural fields and forests (Coll et al. 2005), playas and grasslands (Wan et al. 2004; Wan 2008), and for a range of different seasons and years. LST errors are generally within  $\pm 1$  K for all sites under stable atmospheric conditions except semi-arid and arid areas, which had errors of up to 5 K (Wan and Li 2008).

Initial testing and validation of the MOD21 emissivity product has shown good agreement with the North American ASTER Land Surface Database (NAALSED) v2.0 emissivity product (Hulley et al. 2009b) and in-situ data over nine pseudo-invariant sand dune sites in the southwestern United States to  $<0.02$  (2%) (Hulley and Hook 2011). NAALSED was validated over arid/semi-arid regions using nine pseudo-invariant sand dune sites in the western/southwestern United States. The emissivity of samples collected at each of the nine sites was determined in the laboratory using a Nicolet 520 FT-IR spectrometer and convolved with the appropriate ASTER system response functions. Validation of emissivity data from space ideally requires a site that is homogeneous in emissivity at the scale of the imagery, allowing several image pixels to be validated over the target site. The nine sand dune validation sites chosen for the ASTER study and planned for use with the MOD21 product are: Great Sands National Park, Colorado; White Sands National Monument, New Mexico; Kelso Dunes, California; Algodones Dunes, California;

Stovepipe Wells Dunes, California; Coral Pink Sand Dunes, Utah; Little Sahara Dunes, Utah; Killpecker Dunes, Wyoming; and Moses Lake Basalt Dunes, Washington.

A validation study at the Land Surface Analysis–Satellite Application Facility (LSA-SAF) Gobabeb validation site in Namibia showed that MOD21 LSEs matched closely with in-situ emissivity data (~1%), while emissivities based on land cover classification products (e.g., SEVIRI, MOD11) overestimated emissivities over the sand dunes by as much as 3.5% (Gottsche and Hulley 2012). R-based validation of the MOD21 product is currently underway over nine pseudo-invariant sites in southwestern United States, and the Lake Tahoe and Salton Sea sites.

For the MOD21 product we plan to use in-situ data from a variety of ground sites covering the majority of different land-cover types defined in the International Geosphere-Biosphere Programme (IGBP). The sites will consist of water, vegetation (forest, grassland, and crops), and barren areas (Table 8).

**Table 8. The core set of global validation sites according to IGBP class to be used for validation and calibration of the MODIS MOD21 land surface temperature and emissivity product.**

IGBP Class	Sites
0 Water	Tahoe, Salton Sea, CA
1,2 Needle-leaf forest	Krasnoyarsk, Russia; Tharandt, Germany; Fairhope, Alaska
3,4,5 Broad-leaf/mixed forest	Chang Baisan, China; Hainich, Germany; Hilo, Hawaii
6,7 Open/closed shrublands	Desert Rock, NV; Stovepipe Wells, CA
8,9,10 Savannas/Grasslands	Boulder, CO; Fort Peck, MT
12 Croplands	Bondville, IL; Penn State, PA; Sioux Falls, SD; Goodwin Creek, MS
16 Barren	Algodones Dunes, CA; Great Sands, CO; White Sands, NM; Kelso Dunes, CA; Namib Desert, Namibia; Kalahari Desert, Botswana

### 11.1 Water Sites

For water surfaces, we will use the Lake Tahoe, California/Nevada, automated validation site where measurements of skin temperature have been made every two minutes since 1999 and are used to validate the mid and thermal infrared data and products from ASTER and MODIS (Hook et al. 2007). Water targets are ideal for cal/val activities because they are thermally homogeneous and the emissivity is generally well known. A further advantage of Tahoe is that the lake is located at high altitude, which minimizes atmospheric correction errors, and is large enough to validate sensors from pixel ranges of tens of meters to several kilometers. More recently in

2008, an additional cal/val site at the Salton Sea was established. Salton Sea is a low-altitude site with significantly warmer temperatures than Lake Tahoe (up to 35°C), and together they provide a wide range of different conditions. The typical range of temperatures at Tahoe is from 5°C to 25°C.

Figure 23 shows initial validation of the MOD21 emissivity at Lake Tahoe and the Salton Sea. Although the emissivity matches well with the shape of the lab water spectra (black), which were extracted from the ASTER spectral library in this case, there is ~1% difference across all bands which is due to a limitation of the TES calibration. The emissivities in MOD11 are derived from land classification, which is why the emissivity matches exactly the lab spectra at both water sites. Figure 24 shows scatterplot and histogram differences between MODIS Aqua MYD21/MYD11 LST retrieval and in-situ measurements at Lake Tahoe and Salton Sea for three years of MODIS Aqua overpasses. MYD21 performs consistently at both sites with RMSE of ~1 K, while MYD11 performs better at Tahoe (0.5 K) than at Salton Sea (1.5 K).

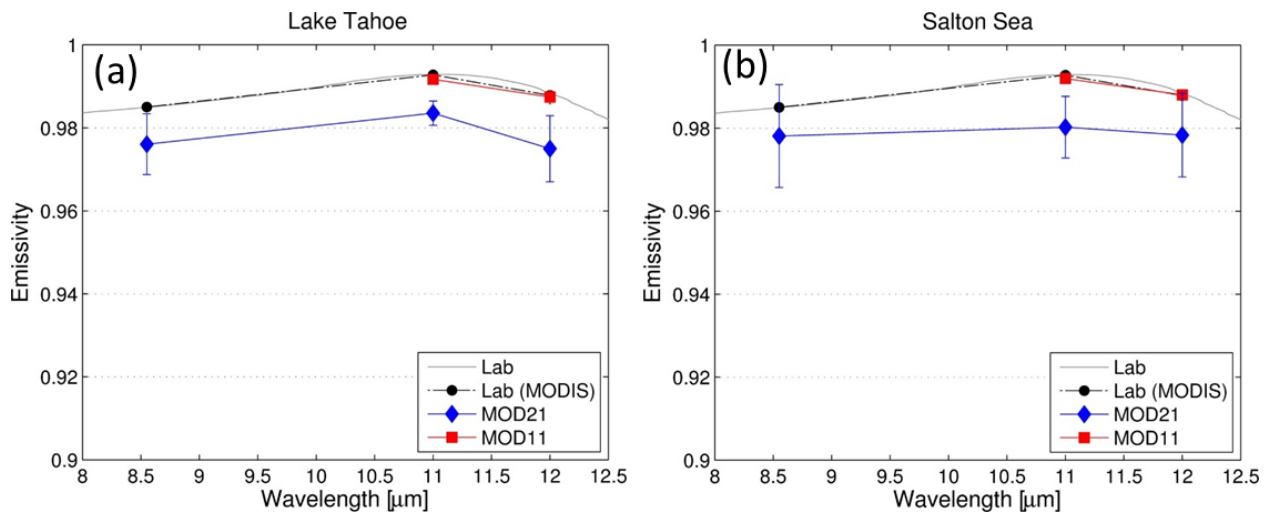
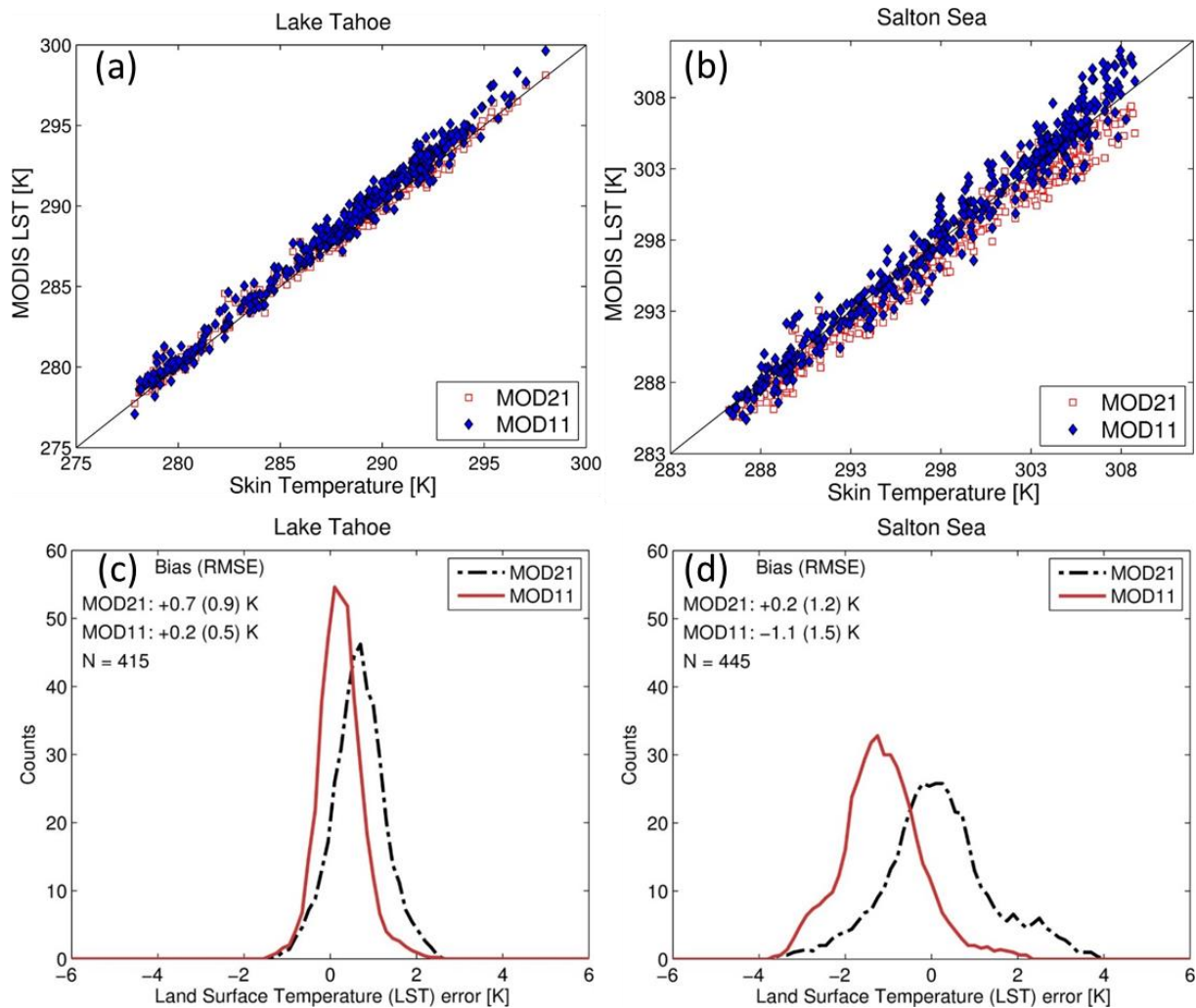


Figure 22. Figures showing the Emissivity retrievals for the MODIS Aqua MYD21 products over two water sites using data collected for three years of data for Lake Tahoe (2003-2005) and Salton Sea (2008-2010). Lab data, Lab data convolved with MODIS bands and the MOD11 bands 31 and 32 are also shown for comparison.



**Figure 23.** An example of the LST validation applied to the MODIS Aqua MYD11 and MYD21 LST products over two water sites using three years of data collected Lake Tahoe (2003-2005) and Salton Sea (2008-2010). While MYD11 performs better than MYD21 at Lake Tahoe (0.5 vs 0.9 K), MYD21 performs better at Salton Sea (1.2 vs 1.5 K).

### 11.2 Pseudo-invariant Sand Dune Sites

For LST validation over arid regions, we will use a set of six pseudo-invariant, homogeneous sand dune sites in the southwestern United States (Hulley et al. 2009b) that were used for validating ASTER and MODIS products, and two sites over large sand dune seas in the Namib and Kalahari deserts in Southern Africa (Hulley et al. 2009c) for validating AIRS. The emissivity and mineralogy of samples collected at these sites have been well characterized and are described by Hulley et al. (2009b).

Pseudo-invariant ground sites such as playas, salt flats, and claypans have been increasingly recognized as optimal targets for the long-term validation and calibration of visible, shortwave, and thermal infrared data (Bannari et al. 2005; Cosnefroy et al. 1996; de Vries et al. 2007; Teillet et al. 1998). We have found that large sand dune fields are particularly useful for the validation of TIR emissivity data (Hulley and Hook 2009a). Sand dunes have consistent and homogeneous mineralogy and physical properties over long time periods. They do not collect water for long periods as playas and pans might, and drying of the surface does not lead to cracks and fissures, typical in any site with a large clay component, which could raise the emissivity due to cavity radiation effects (Mushkin and Gillespie 2005). Furthermore, the mineralogy and composition of sand samples collected in the field can be accurately determined in the laboratory using reflectance and x-ray diffraction (XRD) measurements. In general, the dune sites should be spatially uniform and any temporal variability due to changes in soil moisture and vegetation cover should be minimal. Ideally, the surface should always be dry, since any water on the surface can increase the emissivity by up to 0.16 (16%) in the 8.2–9.2- $\mu\text{m}$  range depending on the type of soil (Mira et al. 2007).

### *11.2.1 Emissivity Validation*

Seasonal changes in vegetation cover, aeolian processes such as wind erosion, deposition and transport, and daily variations in surface soil moisture from precipitation, dew, and snowmelt are the primary factors that could potentially affect the temporal stability and spatial uniformity of the dune sites. Field observations during the spring and early summer of 2008 revealed that the major portion of the dune sites was bare, with the exception of Kelso and Little Sahara, which contained sparse desert grasses and reeds on the outer perimeter of the dune field and in some interdunal areas. Nonetheless, this does not mean the other seven dune sites did not have vegetation in the past, since 2000. The presence of soil moisture would result in a significant increase in TIR emissivity at the dune sites, caused by the water film on the sand particles decreasing its reflectivity (Mira et al. 2007; Ogawa et al. 2006), particularly for MODIS band 29 in the quartz Reststrahlen band. However, given that the majority of dune validation sites are aeolian (high winds), at high altitude (low humidity), and in semi-arid regions (high skin temperatures), the lifetime of soil moisture in the first few micrometers of the surface skin layer as measured in the TIR is most likely small due to large sensible heat fluxes and, therefore, high evaporation rates, in addition to rapid infiltration. Consequently, we hypothesize that it would most likely take a very recent

precipitation event to have any noticeable effect on remote-sensing observations of TIR emissivity over these types of areas.

Figure 25 shows emissivity spectra from sand dune samples collected at ten sand dune sites in the southwestern United States. The spectra cover a wide range of emissivities in the TIR region. These sites will be the core sites used to validate the emissivity and LST products from MODIS.

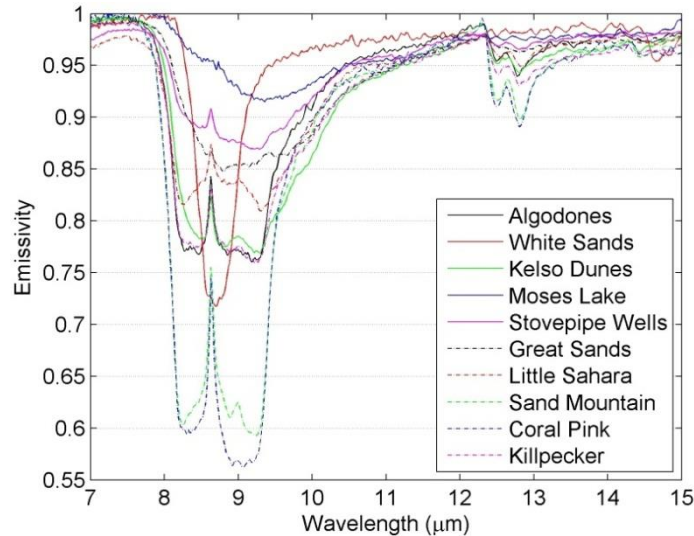


**Figure 24. Laboratory-measured emissivity spectra of sand samples collected at ten pseudo-invariant sand dune sites in the southwestern United States. The sites cover a wide range of emissivities in the TIR region.**

Figure 26 show the emissivity retrievals for the MODIS Aqua MOD21 products over six pseudo-invariant validation sites for MODIS Aqua MOD21 product. All the validation studies were performed with 3 years of MODIS data collected for 2003-2005. As seen in Figure 26, lower values of band 29 emissivities (8-9  $\mu\text{m}$ ) are typical in the bare sites because of the exposed mineralogy. Also included are the lab measurement data, the lab data convolved with MODIS bands 29, 31, and 32, and the emissivities for MOD11 bands 31 and 32 are also shown for comparison. MOD21 retrieves emissivities at all 3-bands, and are compared with the lab-measured emissivity values. Tables 9 show comparison of band 31 emissivity between the laboratory-derived emissivities at each site, along with the mean MOD11 and MOD21 emissivities for band 31 (11  $\mu\text{m}$ ). The emissivity retrievals for MOD21 is closer to the lab values than the MOD11 emissivities for band 31 because MOD11 assigns emissivities based upon land-classification scheme, and are generally higher for bare sites by about 2%. This results into cold bias over bare regions for MOD11 LST product, as we will show next.

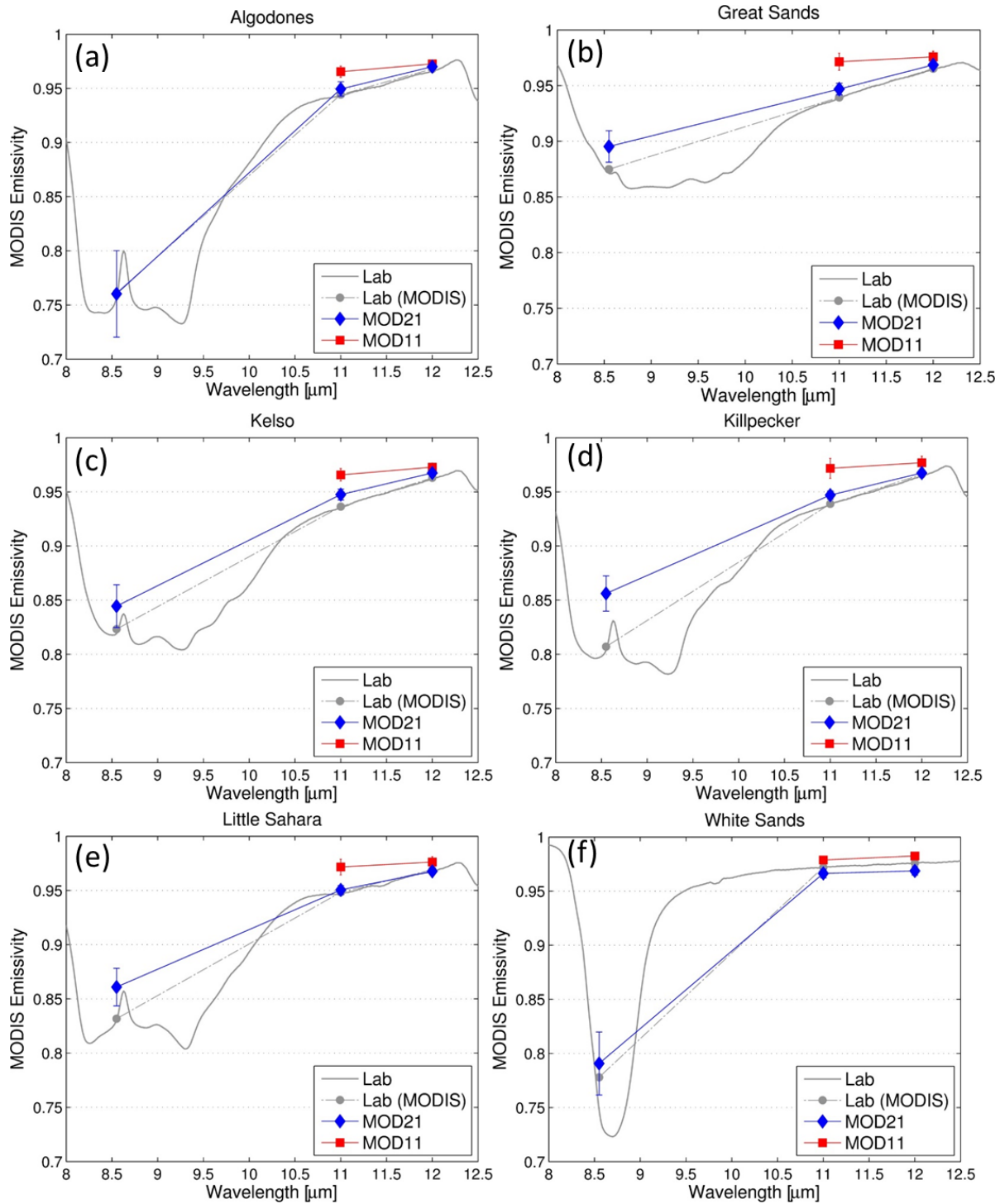


Figure 25. Figures showing the Emissivity retrievals for the MODIS Aqua MYD21 products over six pseudo-invariant sand dune sites using data collected for three years of data (2003-2005); Lab data, Lab data convolved with MODIS bands, and the MOD11 bands 31 and 32 emissivity are also shown for comparison.

### 11.2.2 LST Validation

For LST validation, we use the R-based validation method (Coll et al. 2009a; Wan and Li 2008). The advantage of this method is that it does not require in-situ measurements, but instead relies on atmospheric profiles of temperature and water vapor over the site and an accurate estimation of the emissivity. The R-based method is based on a ‘radiative closure simulation’ with input surface emissivity spectra from either lab or field measurements, atmospheric profiles from an external source (e.g., model or radiosonde), and the retrieved LST product as input. A radiative transfer model is used to forward model these parameters to simulate at-sensor BTs in a clear window region of the atmosphere (11–12  $\mu\text{m}$ ). The input LST product is then adjusted in 2-K steps until two calculated at-sensor BTs bracket the observed BT value. An estimate of the ‘true’ temperature ( $LST_{R-based}$ ) is then found by interpolation between the two calculated BTs, the observed BT, and the initial retrieved LST used in the simulation. The LST error, or uncertainty in the LST retrieval is simply found by taking the difference between the retrieved LST product and the estimate of  $LST_{R-based}$ . This method has been successfully applied to MODIS LST products in previous studies (Coll et al. 2009b; Wan and Li 2008; Wan 2008). For MODIS data, band 31 (10.78–11.28  $\mu\text{m}$ ) is typically used for the simulation since it is the least sensitive to atmospheric absorption in the longwave region. The advantage of the R-based method is that it can be applied to a large number of global sites where the emissivity is known (e.g., from field measurements) and during night- and daytime observations to define the diurnal temperature range.

The archive of all North American MODIS data, as defined by the bounding box 22° to 71° N and 55° to 169° W, was used in this process for each pseudo-invariant site. Each scene was tested to see if it contained the location of interest. Scenes that did not contain the point of interest were eliminated, as were scenes in which the point was located either along scene margins (the first or last row or column of pixels) or whose viewing angle exceeded 40°. Finally, scenes in which the pixel of interest was cloudy, or had greater than three neighboring pixels that were cloudy, were eliminated. Cloudiness was defined as less than a 66% certainty that a pixel was clear in the M\*D35 data. Any scene remaining at this point was used for determination of LST. LST data were derived either directly from the M\*D11\_L2 product or calculated locally using the algorithm for the M\*D21 product. In the latter case, these calculations were performed using the M\*D021KM, M\*D03, M\*D07\_L2, M\*D10A2, M\*D13A2, and M\*D35\_L2 data as input, as

described in Hulley and Hook (2011). In addition to LST, the uncertainty of the value was read from the M\*D11\_L2 data or calculated for the M\*D21 data using the values given in Hulley et al. (2012). Following LST retrieval, atmospheric profiles over the pseudo-invariant site were obtained from either the measurements of the AIRS instrument or from the NCEP GDAS model. Both methods were used for MODIS-Aqua data, while only NCEP GDAS data were used for MODIS-Terra data. Data retrieved for atmospheric profiles were the geopotential heights, temperatures, relative humidities, ozone, and pressure for each geopotential height level of the profile, and the PWV for the column as a whole. Together with the original land surface temperature from M\*D11, these values were then used as input to MODTRAN 5.2 to calculate the Top Of Atmosphere Radiance.

Wan and Li (2008) proposed a quality check to assess the suitability of the atmospheric profiles by looking at differences between observed and calculated BTs in two nearby window regions with different absorption features. For example, the quality check for MODIS bands 31 and 32 at 11 and 12  $\mu\text{m}$  is:

$$\delta(T_{11} - T_{12}) = (T_{11}^{obs} - T_{12}^{obs}) - (T_{11}^{calc} - T_{12}^{calc}) \quad (40)$$

where:  $T_{11}^{obs}$  and  $T_{12}^{obs}$  are the observed brightness temperatures at 11 and 12  $\mu\text{m}$  respectively, and  $T_{11}^{calc}$  and  $T_{12}^{calc}$  are the calculated brightness temperatures from the R-based simulation at 11 and 12  $\mu\text{m}$  respectively. If  $\delta(T_{11} - T_{12})$  is close to zero, then the assumption is that the atmospheric temperature and water vapor profiles are accurately representing the true atmospheric conditions at the time of the observation, granted the emissivity is already well known. Because water vapor absorption is higher in the 12- $\mu\text{m}$  region, negative residual values of  $\delta(T_{11} - T_{12})$  imply the R-based profiles are overestimating the atmospheric effect, while positives values imply an underestimation of atmospheric effects. A simple threshold can be applied to filter out any unsuitable candidate profiles for validation. Although Wan and Li (2008) proposed a threshold of  $\pm 0.3$  K for MODIS data, we performed a sensitivity analysis and found that a threshold of  $\pm 0.5$  K resulted in a good balance between the numbers of profiles accepted and accuracy of the final R-based LST.

Figure 27 show scatterplots of MODIS retrieved LST (MOD11 in red squares and MOD21 in blue-diamonds) versus the R-based LST for six pseudo-invariant sites using all MODIS Aqua data from 2003-2005. The results on the bare sites show that the MOD11 SW LST algorithm

underestimates the LST by about 3–4 K at all sites except White Sands, while the MOD21 algorithm has biases around 1 K.

Figure 28 show the histogram plots of MOD11 and MOD21 LST retrievals. As we observed in Figure 26, MOD11 assigns fixed emissivity for the bare surfaces which is the primary reason for LST bias in MOD11 while MOD21 simultaneously retrieves the LST&E using physics-based TES method. The distribution shows a constant “cold” biased LST retrievals for MOD11 over the bare pseudo-invariant sand dune sites, while MOD21 retrievals are consistently distributed around the mean biases close to zero and RMSE's of ~1 K.

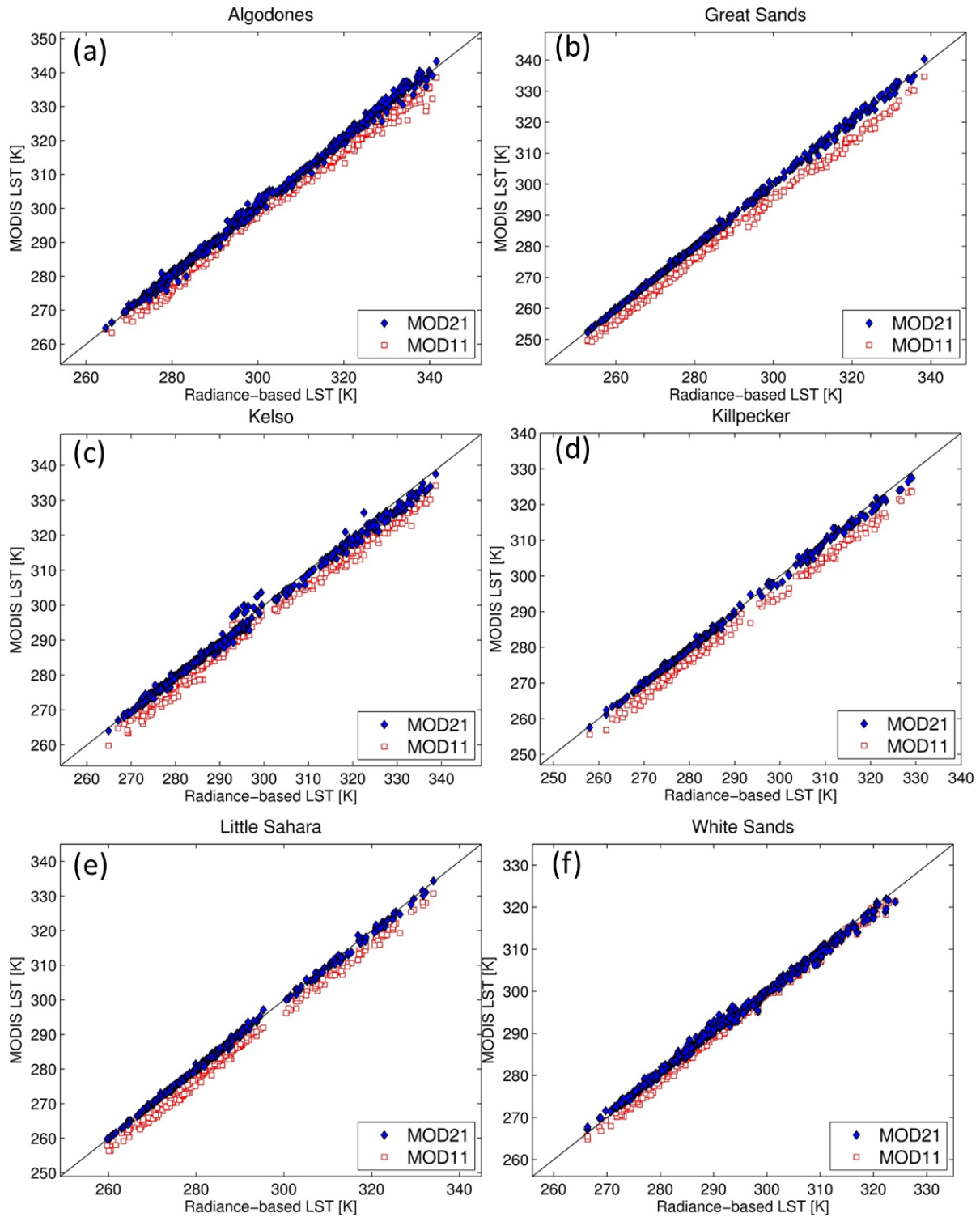


Figure 26. An example of the R-based validation method applied to the MODIS Aqua MYD11 and MYD21 LST products over six pseudo-invariant sand dune sites using all data during 2003-2005. AIRS profiles and lab-measured emissivities from samples collected at the sites were used for the R-based simulations.

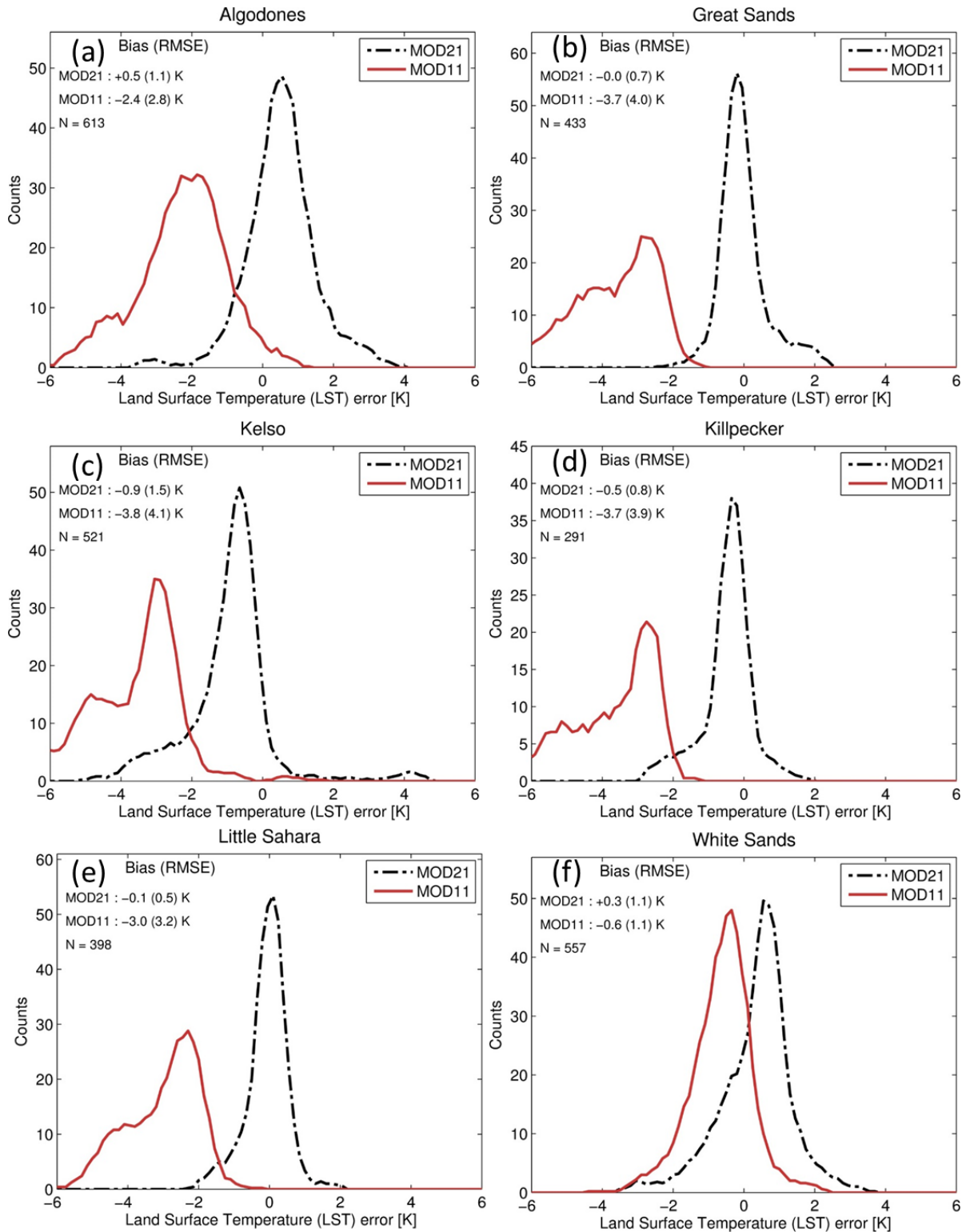


Figure 27. Histogram error plots showing validation of the R-based method applied to the MODIS Aqua MYD11 and MYD21 LST products over six pseudo-invariant sand dune sites using all data during 2003-2005.

### 11.3 Vegetated Sites

For initial testing of the MOD21 product, we used R-based validation over Redwood and Texas Grassland sites. While pseudo-invariant sand dune sites are ideal for R-based validation studies as their emissivity features stay relatively consistent over time in the absence of soil moisture (Hulley and Hook 2009b), special care should be taken over grassland sites that may undergo seasonal or inter-annual changes in vegetation phenology. Also any land surface disturbance such as loss of vegetation by fire or soil exposure from land degradation could cause an error in the validation results that assume a constant emissivity of the surface over time. In order to demonstrate the emissivity stability at the Texas Grassland site, we use MODIS band 31 emissivity over the 3-year period, and compare the band 31 emissivity retrieval with Algodones Dunes site. (Figure. 29). The two-sample running mean time series show relatively small fluctuations with standard deviation (stdev) of  $\sim 0.007$  is observed at Algodones and Texas Grassland sites over the 3-year validation period. This is equivalent to  $\sim 0.2$  K error in the R-based validation method (Hulley and Hook 2012). The histograms on the margins show consistent high density of the data around the mean for each of the sites. Also small standard deviation of 0.007, and 0.006 at Texas Grassland and Algodones Dunes indicate adequate stability of the retrievals over the sites, and therefore using constant in situ emissivity inputs into the R-based validation simulations for both sites are justified (Malakar and Hulley 2016).

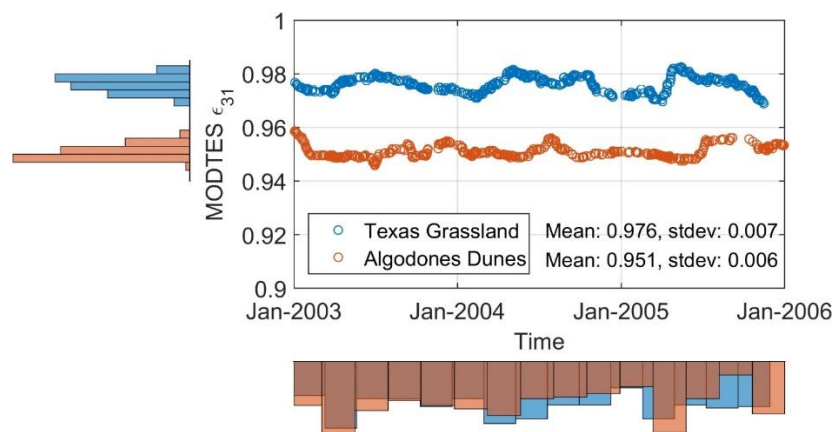


Figure 28. MYD21 Emissivity retrievals for band 31 at the two sites show small fluctuations within the error range of 1% from the mean values. The histograms on the margins show a consistently high density of the data around the mean for each of the sites.

Figure 30 (a & b) show scatterplots of MODIS retrieved LST (MOD11 in red squares and MOD21 in blue-diamonds) versus the R-based LST for Redwood and Texas Grassland sites using all MODIS data from 2003-2005. Figure 30 (c & d) show the histogram plots of MOD11 and MOD21 LST retrievals. The distributions show both the MOD11 and the MOD21 algorithm have RMSE's of around 1 K, with MOD11 having a slight cold bias and MOD21 slight warm bias.

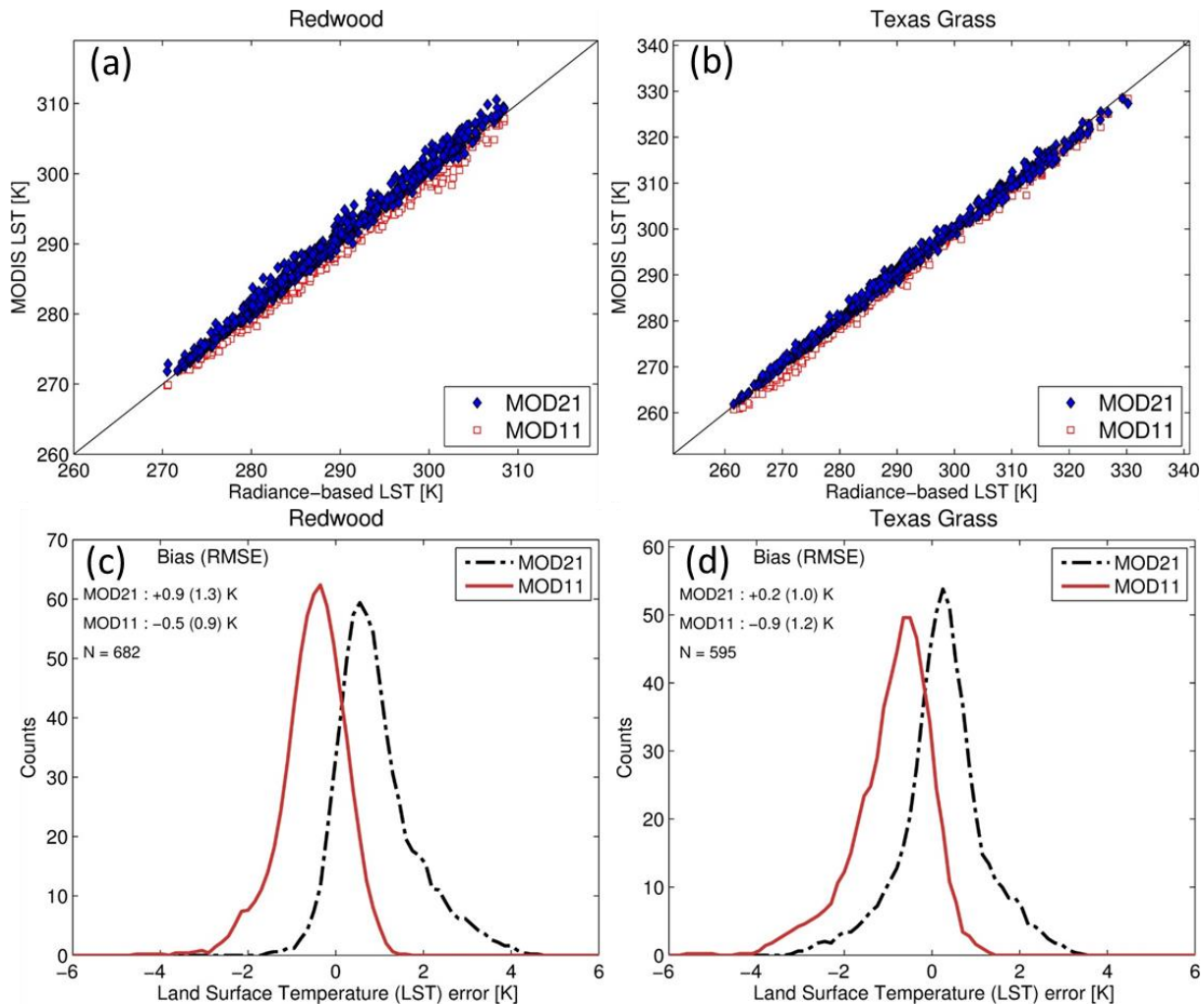


Figure 29. R-based validation for MODIS Aqua MYD11 and MYD21 LST products over Redwood and Texas Grassland sites (a, b) using three years of data collected (2003-2005). The bottom panels (c,d) show the histogram of the distribution of the LST error for both products showing comparable performances at the 1 K level in RMSE, although MYD21 is biased warm while MYD11 is biased cold.

### 11.4 Validation Summary

Table 9 shows comparison of the band 31 emissivity retrievals between MOD21, MOD11 and lab values. The MOD11 emissivity tend to assign about 2% higher in the bare sites. MOD21

retrieves LST&E simultaneously, and performs consistently better than MOD11 over the bare sites when compared to lab spectra. Since MOD11 assigns fixed emissivities based upon the land class information, the water and vegetation sites are relatively more accurate (Table 9).

Figure 32 shows a summary histograms of the MODIS LST retrievals using RMSE at the ten validation sites comprising various kinds of land surface types and wide range of atmospheric characteristics are shown. The corresponding bias and RMSE for MYD21 and MYD11 LST products are also summarized in Table 10. The RMSEs in the bare sites are generally higher, reaching up to 4.1 K for some of the bare sites such as Great Sands, Kelso, and Killpecker. The MYD21 and MYD11 have comparable accuracies for the vegetation and water sites, ~1 K. The reason for the MYD11 cold bias is due to the assignment of emissivity for barren surfaces (~0.96 at 11  $\mu$ m). This causes large LST errors over bare sites where variations in surface composition over bare regions results in emissivities lower than that fixed value. The MxD21 algorithm, on the other hand, physically retrieves the spectral emissivity in MODIS bands 29, 31, and 32, along with the LST, and this results in more accurate LST results, particularly over bare regions where emissivity variations can be large, both spatially and spectrally.

**Table 9. Emissivity comparisons between lab, MYD11, and MYD21 at six sand sites for band 31.**

Sites	Emissivity			% error	
	Lab	MOD11	MOD21	MOD11-Lab	MOD21-Lab
Algodones	0.94	0.97	0.95	2.3	0.6
Great Sands	0.94	0.97	0.95	3.4	0.8
Kelso	0.94	0.97	0.95	3.2	1.2
Killpecker	0.94	0.97	0.95	3.2	0.9
Little Sahara	0.95	0.97	0.95	2.5	0.2
White Sands	0.97	0.98	0.97	0.7	0.6
Redwood	0.99	0.99	0.97	0.2	2.1
Texas Grassland	0.98	0.98	0.97	0.5	0.8
Lake Tahoe	0.99	0.99	0.98	0.1	0.9
Salton Sea	0.99	0.99	0.98	0.1	1.3

**Table 10. R-based LST validation statistics from six pseudo-invariant sand dune sites using all MOD11 and MOD21 LST retrievals during 2005.**

	N	MOD11 Bias	MOD11 RMSE	MOD21 Bias	MOD21 RMSE
<b>Algodones</b>	613	-2.4	2.8	0.5	1.1
<b>Great Sands</b>	433	-3.7	4.0	0.0	0.7
<b>Kelso</b>	521	-3.8	4.1	-0.9	1.5
<b>Killpecker</b>	291	-3.7	3.9	-0.5	0.8
<b>Little Sahara</b>	398	-3.0	3.2	-0.1	0.5
<b>White Sands</b>	557	-0.6	1.1	0.3	1.1
<b>Redwood</b>	682	-0.5	0.9	0.9	1.3
<b>Texas Grassland</b>	595	-0.9	1.2	0.2	1.0
<b>Lake Tahoe</b>	415	0.2	0.5	0.7	0.9
<b>Salton Sea</b>	445	-1.1	1.5	0.2	1.2

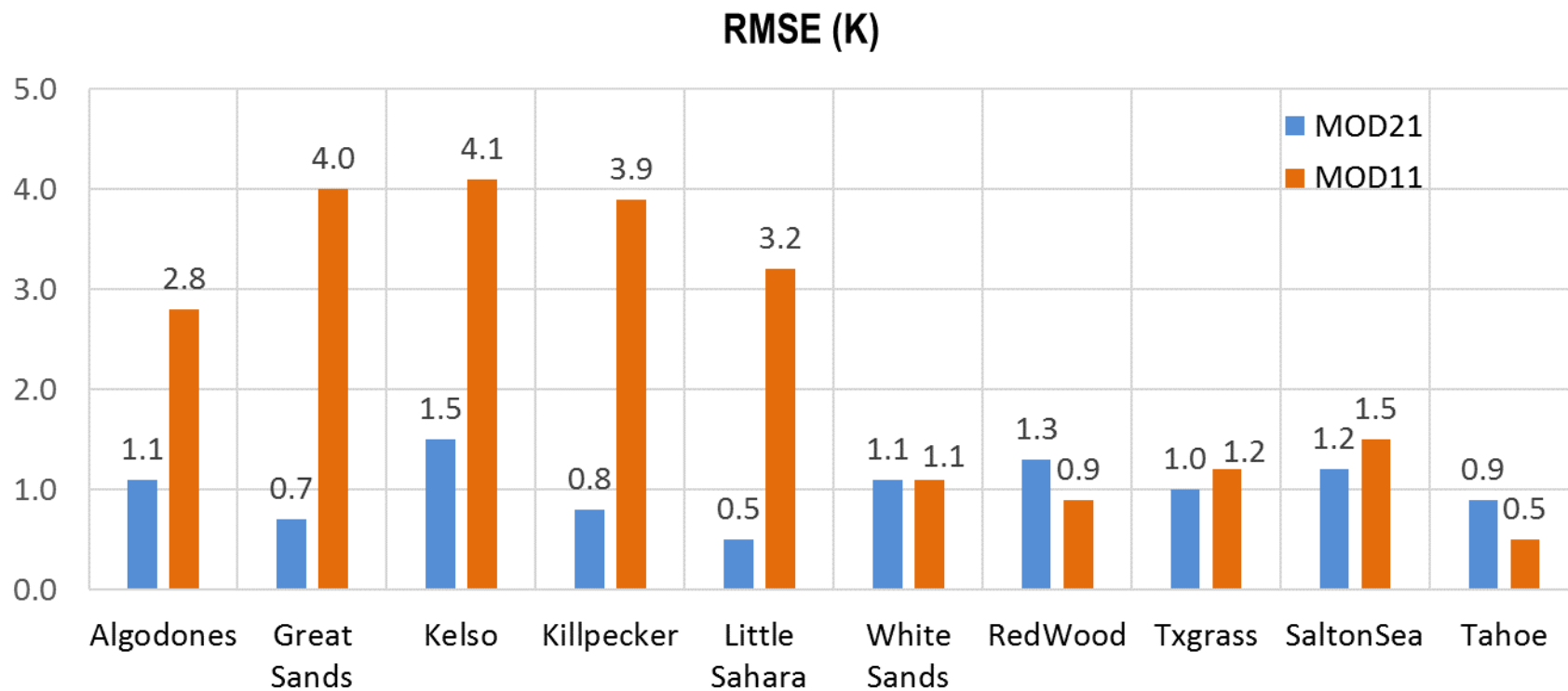


Figure 30. Figures showing the validation summary for LST retrievals for the MODIS Aqua MYD21 and MYD11 products over various IGBP sites using data collected for year 2003-2005, except for Salton Sea (2008-2010).

## 12 References

- Abdalati, W., & Steffen, K. (2001). Greenland ice sheet melt extent: 1979-1999. *Journal of Geophysical Research-Atmospheres*, *106*, 33983-33988
- Anderson, M.C., Hain, C.R., Wardlow, B., Mecikalski, J.R., & Kustas, W.P. (2011a). Evaluation of a drought index based on thermal remote sensing of evapotranspiration over the continental U.S. *Journal of Climate*, *24*, 2025-2044
- Anderson, M.C., Kustas, W.P., Norman, J.M., Hain, C.R., Mecikalski, J.R., Schultz, L., Gonzalez-Dugo, M.P., Cammalleri, C., d'Urso, G., Pimstein, A., & Gao, F. (2011b). Mapping daily evapotranspiration at field to continental scales using geostationary and polar orbiting satellite imagery. *Hydrology and Earth System Sciences*, *15*, 223-239
- Augustine, J.A., DeLuise, J.J., & Long, C.N. (2000). SURFRAD - A national surface radiation budget network for atmospheric research. *Bulletin of the American Meteorological Society*, *81*, 2341-2357
- Baldrige, A.M., Hook, S.J., Grove, C.I., & Rivera, G. (2009a). The ASTER Spectral Library Version 2.0. *Remote Sensing of Environment*, *114*, 711-715
- Baldrige, A.M., Hook, S.J., Grove, C.I., & Rivera, G. (2009b). The ASTER spectral library version 2.0. *Remote Sensing of Environment*, *113*, 711-715
- Bannari, A., Omari, K., Teillet, R.A., & Fedosejevs, G. (2005). Potential of getis statistics to characterize the radiometric uniformity and stability of test sites used for the calibration of earth observation sensors. *Ieee Transactions on Geoscience and Remote Sensing*, *43*, 2918-2926
- Barducci, A., & Pippi, I. (1996). Temperature and emissivity retrieval from remotely sensed images using the "grey body emissivity" method. *Ieee Transactions on Geoscience and Remote Sensing*, *34*, 681-695
- Barnes, W.L., Pagano, T.S., & Salomonson, V.V. (1998). Prelaunch characteristics of the Moderate Resolution Imaging Spectroradiometer (MODIS) on EOS-AM1. *Ieee Transactions on Geoscience and Remote Sensing*, *36*, 1088-1100
- Barton, I.J., Zavody, A.M., Obrien, D.M., Cutten, D.R., Saunders, R.W., & Llewellyn-Jones, D.T. (1989). Theoretical Algorithms for Satellite-Derived Sea-Surface Temperatures. *Journal of Geophysical Research-Atmospheres*, *94*, 3365-3375
- Becker, F., & Li, Z.L. (1990). Temperature-Independent Spectral Indexes in Thermal Infrared Bands. *Remote Sensing of Environment*, *32*, 17-33
- Benson, C.S. (1996). Stratigraphic studies in the snow and firn of the Greenland ice sheet, Snow, Ice and Permafrost Research Establishment (now U.S. Army Cold Regions Research and Engineering Laboratory). In
- Berk, A., Anderson, G.P., Acharya, P.K., Bernstein, L.S., Muratov, L., Lee, J., Fox, M., Adler-Golden, S.M., Chetwynd, J.H., Hoke, M.L., Lockwood, R.B., Gardner, J.A., Cooley, T.W., Borel, C.C., & Lewis, P.E. (2005). MODTRAN<sup>TM</sup> 5, A Reformulated Atmospheric Band Model with Auxiliary Species and Practical Multiple Scattering Options: Update. In S.S. Sylvania & P.E. Lewis (Eds.), *in Proc SPIE, Algorithms and Technologies for Multispectral, Hyperspectral, and Ultraspectral Imagery XI* (pp. 662-667). Bellingham, WA: Proceedings of SPIE

- Bonan, G.B., Oleson, K.W., Vertenstein, M., Levis, S., Zeng, X.B., Dai, Y.J., Dickinson, R.E., & Yang, Z.L. (2002). The land surface climatology of the community land model coupled to the NCAR community climate model. *Journal of Climate*, *15*, 3123-3149
- Borbas, E., Knuteson, R., Seemann, S.W., Weisz, E., Moy, L., & Huang, H. (2007). A high spectral resolution global land surface infrared emissivity database. In, *Joint 2007 EUMETSAT Meteorological Satellite & 15th AMS Satellite Meteorology and Oceanography Conference*. Amsterdam, The Netherlands
- Bosilovich, M.G., Chen, J.Y., Robertson, F.R., & Adler, R.F. (2008). Evaluation of global precipitation in reanalyses. *Journal of Applied Meteorology and Climatology*, *47*, 2279-2299
- Brown, O., & Minnett, P. (1999). MODIS infrared sea surface temperature algorithm. *Algorithm Theoretical Basis Document Version 2*, Univ. of Miami, Miami, Fla.
- Coll, C., & Caselles, V. (1997). A split-window algorithm for land surface temperature from advanced very high resolution radiometer data: Validation and algorithm comparison. *Journal of Geophysical Research-Atmospheres*, *102*, 16697-16713
- Coll, C., Caselles, V., Galve, J.M., Valor, E., Niclos, R., Sanchez, J.M., & Rivas, R. (2005). Ground measurements for the validation of land surface temperatures derived from AATSR and MODIS data. *Remote Sensing of Environment*, *97*, 288-300
- Coll, C., Caselles, V., Valor, E., Niclos, R., Sanchez, J.M., Galve, J.M., & Mira, M. (2007). Temperature and emissivity separation from ASTER data for low spectral contrast surfaces. *Remote Sensing of Environment*, *110*, 162-175
- Coll, C., Wan, Z.M., & Galve, J.M. (2009a). Temperature-based and radiance-based validations of the V5 MODIS land surface temperature product. *Journal of Geophysical Research-Atmospheres*, *114*, -
- Coll, C., Wan, Z.M., & Galve, J.M. (2009b). Temperature-based and radiance-based validations of the V5 MODIS land surface temperature product. *Journal of Geophysical Research-Atmospheres*, *114*, D20102, doi:20110.21029/22009JD012038
- Comiso, J.C. (2006). Arctic warming signals from satellite observations. *Weather*, *61*, 70-76
- Cosnefroy, H.N., Leroy, M., & Briottet, X. (1996). Selection and characterization of Saharan and Arabian desert sites for the calibration of optical satellite sensors. *Remote Sensing of Environment*, *58*, 101-114
- de Vries, C., Danaher, T., Denham, R., Scarth, P., & Phinn, S. (2007). An operational radiometric calibration procedure for the Landsat sensors based on pseudo-invariant target sites. *Remote Sensing of Environment*, *107*, 414-429
- Deschamps, P.Y., & Phulpin, T. (1980). Atmospheric Correction of Infrared Measurements of Sea-Surface Temperature Using Channels at 3.7, 11 and 12  $\mu$ -M. *Boundary-Layer Meteorology*, *18*, 131-143
- Eyre, J.R., & Woolf, H.M. (1988). Transmittance of Atmospheric Gases in the Microwave Region - a Fast Model. *Applied Optics*, *27*, 3244-3249
- Francois, C., Brisson, A., Le Borgne, P., & Marsouin, A. (2002). Definition of a radiosounding database for sea surface brightness temperature simulations - Application to sea surface temperature retrieval algorithm determination. *Remote Sensing of Environment*, *81*, 309-326

- Francois, C., & Otle, C. (1996). Atmospheric corrections in the thermal infrared: Global and water vapor dependent Split-Window algorithms - Applications to ATSR and AVHRR data. *Ieee Transactions on Geoscience and Remote Sensing*, 34, 457-470
- French, A.N., Schmugge, T.J., Ritchie, J.C., Hsu, A., Jacob, F., & Ogawa, K. (2008). Detecting land cover change at the Jornada Experimental Range, New Mexico with ASTER emissivities. *Remote Sensing of Environment*, 112, 1730-1748
- Galve, J.A., Coll, C., Caselles, V., & Valor, E. (2008). An atmospheric radiosounding database for generating land surface temperature algorithms. *Ieee Transactions on Geoscience and Remote Sensing*, 46, 1547-1557
- Gillespie, A., Rokugawa, S., Hook, S., Matsunaga, T., & Kahle, A.B. (1999). Temperature/Emissivity Separation Algorithm Theoretical Basis Document, Version 2.4, ASTER TES ATBD, NASA Contract NAS5-31372, 31322 March, 31999
- Gillespie, A., Rokugawa, S., Matsunaga, T., Cothorn, J.S., Hook, S., & Kahle, A.B. (1998). A temperature and emissivity separation algorithm for Advanced Spaceborne Thermal Emission and Reflection Radiometer (ASTER) images. *Ieee Transactions on Geoscience and Remote Sensing*, 36, 1113-1126
- Gottsche, F.M., & Hulley, G.C. (2012). Validation of six satellite-retrieved land surface emissivity products over two land cover types in a hyper-arid region. *Remote Sensing of Environment*, 124, 149-158
- Gustafson, W.T., Gillespie, A.R., & Yamada, G.J. (2006). Revisions to the ASTER temperature/emissivity separation algorithm. In *2nd International Symposium on Recent Advances in Quantitative Remote Sensing*. Torrent (Valencia), Spain
- Hall, D.K., Williams Jr., R.S., Casey, K.A., Digirolamo, N.E., & Wan, Z. (2006). Satellite-derived, melt-season surface temperature of the Greenland Ice Sheet (2000-2005) and its relationship to mass balance. *Geophysical Research Letters*, 33:L11501, doi:10.1029/2006GL026444
- Hall, D.K., Williams, R.S., Luthcke, S.B., & Digirolamo, N.E. (2008). Greenland ice sheet surface temperature, melt and mass loss: 2000-06. *Journal of Glaciology*, 54, 81-93
- Hook, S., Johnson, W., & Abrams, M. (2013). NASA's Hyperspectral Thermal Emission Spectrometer (HyTES). In C. Kuenzer & S. Dech (Eds.), *Thermal Infrared Remote Sensing - Sensors, Methods, Applications*: Springer
- Hook, S.J., Dmochowski, J.E., Howard, K.A., Rowan, L.C., Karlstrom, K.E., & Stock, J.M. (2005). Mapping variations in weight percent silica measured from multispectral thermal infrared imagery - Examples from the Hiller Mountains, Nevada, USA and Tres Virgenes-La Reforma, Baja California Sur, Mexico. *Remote Sensing of Environment*, 95, 273-289
- Hook, S.J., Gabell, A.R., Green, A.A., & Kealy, P.S. (1992). A Comparison of Techniques for Extracting Emissivity Information from Thermal Infrared Data for Geologic Studies. *Remote Sensing of Environment*, 42, 123-135
- Hook, S.J., Vaughan, R.G., Tonooka, H., & Schladow, S.G. (2007). Absolute radiometric in-flight validation of mid infrared and thermal infrared data from ASTER and MODIS on the terra spacecraft using the Lake Tahoe, CA/NV, USA, automated validation site. *Ieee Transactions on Geoscience and Remote Sensing*, 45, 1798-1807

- Hulley, G.C., & Hook, S.J. (2009a). Intercomparison of Versions 4, 4.1 and 5 of the MODIS Land Surface Temperature and Emissivity Products and Validation with Laboratory Measurements of Sand Samples from the Namib Desert, Namibia. *Remote Sensing of Environment*, 113, 1313-1318
- Hulley, G.C., & Hook, S.J. (2009b). The North American ASTER Land Surface Emissivity Database (NAALSED) Version 2.0. *Remote Sensing of Environment*, 113, 1967-1975
- Hulley, G.C., & Hook, S.J. (2009c). The North American ASTER Land Surface Emissivity Database (NAALSED) Version 2.0. *Remote Sensing of Environment*, 113, 1967-1975
- Hulley, G.C., & Hook, S.J. (2011). Generating Consistent Land Surface Temperature and Emissivity Products Between ASTER and MODIS Data for Earth Science Research. *Ieee Transactions on Geoscience and Remote Sensing*, 49, 1304-1315
- Hulley, G.C., & Hook, S.J. (2012). A radiance-based method for estimating uncertainties in the Atmospheric Infrared Sounder (AIRS) land surface temperature product. *Journal of Geophysical Research-Atmospheres*, 117
- Hulley, G.C., Hook, S.J., Abbott, E., Malakar, N., Islam, T., & Abrams, M. (2015a). The ASTER Global Emissivity Database (ASTER GED): Mapping Earth's emissivity at 100 meter spatial scale. *Geophysical Research Letters*, 42, doi:10.1002/2015GL065564
- Hulley, G.C., Hook, S.J., Abbott, E., Malakar, N., Islam, T., & Abrams, M. (2015b). The ASTER Global Emissivity Dataset (ASTER GED): Mapping Earth's emissivity at 100 meter spatial scale. *Geophysical Research Letters*, 42, 7966-7976
- Hulley, G.C., Hook, S.J., & Baldrige, A.M. (2008). ASTER land surface emissivity database of California and Nevada. *Geophysical Research Letters*, 35, L13401, doi: 10.1029/2008gl034507
- Hulley, G.C., Hook, S.J., & Baldrige, A.M. (2009a). Validation of the North American ASTER Land Surface Emissivity Database (NAALSED) version 2.0 using pseudo-invariant sand dune sites. *Remote Sensing of Environment*, 113, 2224-2233
- Hulley, G.C., Hook, S.J., & Baldrige, A.M. (2009b). Validation of the North American ASTER Land Surface Emissivity Database (NAALSED) Version 2.0 using Pseudo-Invariant Sand Dune Sites. *Remote Sensing of Environment*, 113, 2224-2233
- Hulley, G.C., Hook, S.J., & Baldrige, A.M. (2010). Investigating the Effects of Soil Moisture on Thermal Infrared Land Surface Temperature and Emissivity Using Satellite Retrievals and Laboratory Measurements. *Remote Sensing of Environment*, 114, 1480-1493
- Hulley, G.C., Hook, S.J., Manning, E., Lee, S.Y., & Fetzer, E.J. (2009c). Validation of the Atmospheric Infrared Sounder (AIRS) Version 5 (v5) Land Surface Emissivity Product over the Namib and Kalahari Deserts. *Journal of Geophysical Research Atmospheres*, 114, D19104
- Hulley, G.C., Hughes, T., & Hook, S.J. (2012). Quantifying Uncertainties in Land Surface Temperature (LST) and Emissivity Retrievals from ASTER and MODIS Thermal Infrared Data. *Journal of Geophysical Research Atmospheres*, in press.
- Jimenez-Munoz, J.C., & Sobrino, J.A. (2010). A Single-Channel Algorithm for Land-Surface Temperature Retrieval From ASTER Data. *Ieee Geoscience and Remote Sensing Letters*, 7, 176-179

- Jin, M.L., & Liang, S.L. (2006). An improved land surface emissivity parameter for land surface models using global remote sensing observations. *Journal of Climate*, 19, 2867-2881
- Justice, C., & Townshend, J. (2002). Special issue on the moderate resolution imaging spectroradiometer (MODIS): a new generation of land surface monitoring. *Remote Sensing of Environment*, 83, 1-2
- Justice, C.O., Vermote, E., Townshend, J.R.G., Defries, R., Roy, D.P., Hall, D.K., Salomonson, V.V., Privette, J.L., Riggs, G., Strahler, A., Lucht, W., Myneni, R.B., Knyazikhin, Y., Running, S.W., Nemani, R.R., Wan, Z.M., Huete, A.R., van Leeuwen, W., Wolfe, R.E., Giglio, L., Muller, J.P., Lewis, P., & Barnsley, M.J. (1998). The Moderate Resolution Imaging Spectroradiometer (MODIS): Land remote sensing for global change research. *Ieee Transactions on Geoscience and Remote Sensing*, 36, 1228-1249
- Kalnay, E., Kanamitsu, M., & Baker, W.E. (1990). Global Numerical Weather Prediction at the National-Meteorological-Center. *Bulletin of the American Meteorological Society*, 71, 1410-1428
- Kealy, M.J., Montgomery, M., & Dovidio, J.F. (1990). Reliability and Predictive-Validity of Contingent Values - Does the Nature of the Good Matter. *Journal of Environmental Economics and Management*, 19, 244-263
- Kealy, P.S., & Hook, S. (1993). Separating temperature & emissivity in thermal infrared multispectral scanner data: Implication for recovering land surface temperatures. *Ieee Transactions on Geoscience and Remote Sensing*, 31, 1155-1164
- Key, J.R., Mahoney, R., Liu, Y.H., Romanov, P., Tschudi, M., Appel, I., Maslanik, J., Baldwin, D., Wang, X.J., & Meade, P. (2013). Snow and ice products from Suomi NPP VIIRS. *Journal of Geophysical Research-Atmospheres*, 118, 12816-12830
- Kinter, J.L., Shukla, J., Marx, L., & Schneider, E.K. (1988). A simulation of the winter and summer circulations with the NMC global spectral model. *Journal of Atmospheric Science*, 45, 2486-2522
- Kneizys, F.X., Abreu, L.W., Anderson, G.P., Chetwynd, J.H., Shettle, E.P., Berk, A., Bernstein, L.S., Robertson, D.C., Acharya, P.K., Rothman, L.A., Selby, J.E.A., Gallery, W.O., & Clough, S.A. (1996). The MODTRAN 2/3 Report & LOWTRAN 7 Model, F19628-91-C-0132. In, *Phillips Lab. Hanscom AFB, MA*
- Li, F.Q., Jackson, T.J., Kustas, W.P., Schmugge, T.J., French, A.N., Cosh, M.H., & Bindlish, R. (2004). Deriving land surface temperature from Landsat 5 and 7 during SMEX02/SMACEX. *Remote Sensing of Environment*, 92, 521-534
- Li, Z.L., Becker, F., Stoll, M.P., & Wan, Z.M. (1999). Evaluation of six methods for extracting relative emissivity spectra from thermal infrared images. *Remote Sensing of Environment*, 69, 197-214
- Lyon, R. (1965). Analysis of ROcks by Spectral INfrared Emission (8 to 25 microns). *Economic Geology and the Bulletin of the Society of Economic Geologists*, 60, 715-736
- Malakar, N.K., & Hulley, G.C. (2016). A Water Vapor Scaling Model for Improved Land Surface Temperature and Emissivity Separation of MODIS Thermal Infrared Data. *Remote Sensing of Environment*

- Masuda, K., Takashima, T., & Takayama, Y. (1988). Emissivity of Pure and Sea Waters for the Model Sea-Surface in the Infrared Window Regions. *Remote Sensing of Environment*, 24, 313-329
- Matricardi, M. (2009). Technical Note: An assessment of the accuracy of the RTTOV fast radiative transfer model using IASI data. *Atmospheric Chemistry and Physics*, 9, 6899-6913
- Matricardi, M., Chevallier, F., & Tjemkes, S.A. (2001). An improved general fast radiative transfer model for the assimilation of radiance observations. In: European Centre for Medium-Range Weather Forecasts
- Matsunaga, T. (1994). A temperature-emissivity separation method using an empirical relationship between the mean, the maximum, & the minimum of the thermal infrared emissivity spectrum, in Japanese with English abstract. *Journal Remote Sensing Society Japan*, 14, 230-241
- Mira, M., Valor, E., Boluda, R., Caselles, V., & Coll, C. (2007). Influence of soil water content on the thermal infrared emissivity of bare soils: Implication for land surface temperature determination. *Journal of Geophysical Research-Earth Surface*, 112, F04003
- Mushkin, A., & Gillespie, A.R. (2005). Estimating sub-pixel surface roughness using remotely sensed stereoscopic data. *Remote Sensing of Environment*, 99, 75-83
- Norman, J.M., & Becker, F. (1995). Terminology in Thermal Infrared Remote-Sensing of Natural Surfaces. *Agricultural and Forest Meteorology*, 77, 153-166
- Ogawa, K. (2004). Mapping Surface Broadband Emissivity of the Sahara Desert Using ASTER and MODIS Data. *Earth Interactions*, 8, -
- Ogawa, K., Schmugge, T., Jacob, F., & French, A. (2003). Estimation of land surface window (8-12  $\mu$  m) emissivity from multispectral thermal infrared remote sensing - A case study in a part of Sahara Desert. *Geophysical Research Letters*, 30, -
- Ogawa, K., Schmugge, T., & Rokugawa, S. (2006). Observations of the dependence of the thermal infrared emissivity on soil moisture. *Geophysical Research Abstracts*, 8, 04996
- Oleson, K.W., Bonan, G.B., Levis, S., & Vertenstein, M. (2004). Effects of land use change on North American climate: impact of surface datasets and model biogeophysics. *Climate Dynamics*, 23, 117-132
- Palluconi, F., Hoover, G., Alley, R.E., Nilsen, M.J., & Thompson, T. (1999). An atmospheric correction method for ASTER thermal radiometry over land, ASTER algorithm theoretical basis document (ATBD), Revision 3, Jet Propulsion Laboratory, Pasadena, CA, 1999
- Parkinson, C.L., Cavalieri, D.J., Gloersen, P., Zwally, H.J., & Comiso, J.C. (1999). Arctic sea ice extents, areas, and trends, 1978-1996. *Journal of Geophysical Research-Oceans*, 104, 20837-20856
- Prata, A.J. (1994). Land-Surface Temperatures Derived from the Advanced Very High-Resolution Radiometer and the Along-Track Scanning Radiometer .2. Experimental Results and Validation of Avhrr Algorithms. *Journal of Geophysical Research-Atmospheres*, 99, 13025-13058
- Price, J.C. (1984). Land surface temperature measurements from the split window channels of the NOAA 7 Advanced Very High Resolution Radiometer. *Journal of Geophysical Research*, 89, 7231-7237

- Rhee, J., Im, J., & Carbone, G.J. (2010). Monitoring agricultural drought for arid and humid regions using multi-sensor remote sensing data. *Remote Sensing of Environment*, 114, 2875-2887
- Sabol, D.E., Gillespie, A.R., Abbott, E., & Yamada, G. (2009). Field validation of the ASTER Temperature-Emissivity Separation algorithm. *Remote Sensing of Environment*, 113, 2328-2344
- Salomonson, V.V., Barnes, W.L., Maymon, P.W., Montgomery, H.E., & Ostrow, H. (1989). Modis - Advanced Facility Instrument for Studies of the Earth as a System. *Ieee Transactions on Geoscience and Remote Sensing*, 27, 145-153
- Saunders, R., Matricardi, M., & Brunel, P. (1999). An improved fast radiative transfer model for assimilation of satellite radiance observations. *Quarterly Journal of the Royal Meteorological Society*, 125, 1407-1425
- Seemann, S.W., Borbas, E., Li, J., Menzel, P., & Gumley, L.E. (2006). MODIS Atmospheric Profile Retrieval Algorithm Theoretical Basis Document, Cooperative Institute for Meteorological Satellite Studies, University of Wisconsin-Madison, Madison, WI, Version 6, October 25, 2006
- Seemann, S.W., Borbas, E.E., Knuteson, R.O., Stephenson, G.R., & Huang, H.L. (2008). Development of a global infrared land surface emissivity database for application to clear sky sounding retrievals from multispectral satellite radiance measurements. *Journal of Applied Meteorology and Climatology*, 47, 108-123
- Seemann, S.W., Li, J., Menzel, W.P., & Gumley, L.E. (2003). Operational retrieval of atmospheric temperature, moisture, and ozone from MODIS infrared radiances. *Journal of Applied Meteorology*, 42, 1072-1091
- Snyder, W.C., Wan, Z., Zhang, Y., & Feng, Y.Z. (1998). Classification-based emissivity for land surface temperature measurement from space. *International Journal of Remote Sensing*, 19, 2753-2774
- Snyder, W.C., Wan, Z.M., Zhang, Y.L., & Feng, Y.Z. (1997). Thermal infrared (3-14  $\mu$  m) bidirectional reflectance measurements of sands and soils. *Remote Sensing of Environment*, 60, 101-109
- Strahler, A.H., Zhang, X., Cooper, A., Schaaf, C., Friedl, M., Hodges, J., Baccini, A., & Gao, F. (2002). Validation of the consistent-year v003 MODIS land cover product. <http://www-modis.bu.edu/landcover/userguide/c/consistent.htm>
- Susskind, J., Barnett, C.D., & Blaisdell, J.M. (2003). Retrieval of atmospheric and surface parameters from AIRS/AMSU/HSB data in the presence of clouds. *Ieee Transactions on Geoscience and Remote Sensing*, 41, 390-409
- Teillet, P.M., Fedosejevs, G., Gautier, R.P., & Schowengerdt, R.A. (1998). Uniformity characterization of land test sites used for radiometric calibration of earth observation sensors. In, *Proc. 20th Can. Symp. Remote Sensing* (pp. 1-4). Calgary, AB, Canada
- Tobin, D.C., Revercomb, H.E., Knuteson, R.O., Lesht, B.M., Strow, L.L., Hannon, S.E., Feltz, W.F., Moy, L.A., Fetzer, E.J., & Cress, T.S. (2006). Atmospheric Radiation Measurement site atmospheric state best estimates for Atmospheric Infrared Sounder temperature and water vapor retrieval validation. *Journal of Geophysical Research-Atmospheres*, 111, -
- Tonooka, H. (2001). An atmospheric correction algorithm for thermal infrared multispectral data over land - A water-vapor scaling method. *Ieee Transactions on Geoscience and Remote Sensing*, 39, 682-692
-

- Tonooka, H. (2005). Accurate atmospheric correction of ASTER thermal infrared imagery using the WVS method. *Ieee Transactions on Geoscience and Remote Sensing*, 43, 2778-2792
- Tonooka, H., & Palluconi, F.D. (2005). Validation of ASTER/TIR standard atmospheric correction using water surfaces. *Ieee Transactions on Geoscience and Remote Sensing*, 43, 2769-2777
- Tonooka, H., Palluconi, F.D., Hook, S.J., & Matsunaga, T. (2005). Vicarious calibration of ASTER thermal infrared bands. *Ieee Transactions on Geoscience and Remote Sensing*, 43, 2733-2746
- Valor, E., & Caselles, V. (1996). Mapping land surface emissivity from NDVI: Application to European, African, and South American areas. *Remote Sensing of Environment*, 57, 167-184
- Vargas, M., Miura, T., Shabanov, N., & Kato, A. (2013). An initial assessment of Suomi NPP VIIRS vegetation index EDR. *Journal of Geophysical Research-Atmospheres*, 118, 12301-12316
- Vaughan, R.G., Hook, S.J., Calvin, W.M., & Taranik, J.V. (2005). Surface mineral mapping at Steamboat Springs, Nevada, USA, with multi-wavelength thermal infrared images. *Remote Sensing of Environment*, 99, 140-158
- Wan, Z. (1999). MODIS Land-Surface Temperature Algorithm Theoretical Basis Document (LST ATBD), Version 3.3, University of California, Santa Barbara, April 1999
- Wan, Z., & Li, Z.L. (2008). Radiance-based validation of the V5 MODIS land-surface temperature product. *International Journal of Remote Sensing*, 29, 5373-5395
- Wan, Z., Zhang, Y., Zhang, Q., & Li, Z.L. (2004). Quality assessment and validation of the MODIS global land surface temperature. *International Journal of Remote Sensing*, 25, 261-274
- Wan, Z.M. (2008). New refinements and validation of the MODIS Land-Surface Temperature/Emissivity products. *Remote Sensing of Environment*, 112, 59-74
- Wan, Z.M., & Dozier, J. (1996). A generalized split-window algorithm for retrieving land-surface temperature from space. *Ieee Transactions on Geoscience and Remote Sensing*, 34, 892-905
- Wan, Z.M., & Li, Z.L. (1997). A physics-based algorithm for retrieving land-surface emissivity and temperature from EOS/MODIS data. *Ieee Transactions on Geoscience and Remote Sensing*, 35, 980-996
- Wang, K.C., & Liang, S.L. (2009). Evaluation of ASTER and MODIS land surface temperature and emissivity products using long-term surface longwave radiation observations at SURFRAD sites. *Remote Sensing of Environment*, 113, 1556-1565
- Watson, K. (1992). Spectral Ratio Method for Measuring Emissivity. *Remote Sensing of Environment*, 42, 113-116
- Watson, K., Kruse, F.A., & Hummermiller, S. (1990). Thermal Infrared Exploration in the Carlin Trend, Northern Nevada. *Geophysics*, 55, 70-79
- Yao, Z.G., Li, J., Li, J.L., & Zhang, H. (2011). Surface Emissivity Impact on Temperature and Moisture Soundings from Hyperspectral Infrared Radiance Measurements. *Journal of Applied Meteorology and Climatology*, 50, 1225-1235
- Yu, Y., Pinheiro, J.L., & Privette, J.L. (2006). Correcting Land Surface Temperature Measurements for Directional Emissivity Over 3-D Structured Vegetation. *Proc. SPIE*, 6298, 629817, DOI:629810.621117/629812.682951

- Yu, Y., Privette, J.L., & Pinheiro, A.C. (2008). Evaluation of split-window land surface temperature algorithms for generating climate data records. *Ieee Transactions on Geoscience and Remote Sensing*, 46, 179-192
- Yu, Y.Y., Privette, J.L., & Pinheiro, A.C. (2005). Analysis of the NPOESS VIIRS land surface temperature algorithm using MODIS data. *Ieee Transactions on Geoscience and Remote Sensing*, 43, 2340-2350
- Zeng, Q.C., Zhang, X.H., Liang, X.Z., Yuan, C.G., & Chen, S.F. (1989). Documentation of IAP two-level atmospheric general circulation model. In U.S.D.o. Energy (Ed.) (p. 383 pp.). Washington, D.C.
- Zhou, L., Dickinson, R.E., Ogawa, K., Tian, Y., Jin, M., Schmugge, T., & Tsvetsinskaya, E. (2003a). Relations between albedos and emissivities from MODIS and ASTER data over North African desert. *Geophysical Research Letters*, 30, -
- Zhou, L., Dickinson, R.E., Tian, Y., Jin, M., Ogawa, K., Yu, H., & Schmugge, T. (2003b). A sensitivity study of climate and energy balance simulations with use of satellite-derived emissivity data over Northern Africa and the Arabian Peninsula. *Journal of Geophysical Research-Atmospheres*, 108, 4795



---